2010

Effect of catalysts on hydrogen storage properties of MgH2

Abbas Ranjbar
University of Wollongong

Effect of catalysts on hydrogen storage properties of MgH_2

A thesis submitted in fulfilment of the requirements for
the award of the degree

Doctor of Philosophy

from

University of Wollongong

by

Abbas Ranjbar

(B.S. Physics, M.S. Physics)

Institute for Superconducting and Electronic Materials

February 2010

Dedicated to

My love

Masi

تقدیم به همسر و همسفر عزیزم

CERTIFICATION

I, Abbas Ranjbar, declare that this thesis, submitted in partial fulfilment of the requirements for the award of Doctor of Philosophy, in the Institute for Superconducting and Electronic Materials, University of Wollongong, is wholly my own work unless otherwise referenced or acknowledged. The document has not been submitted for qualifications at any other academic institution.

Abbas Ranjbar

28 Feb. 2010

Acknowledgements

It is my great pleasure to express my gratitude to my supervisors, Professor Huakun Liu and Dr. Zaiping Guo, for their inspiration, guidance, encouragement, and financial and spiritual support. I feel fortunate to have been associated with them, and I believe that I still can learn much from them. I wish to express my special thanks to Professor Shixue Dou for being a model of dignity and remarkable managerial skill. I owe my deep gratitude to Professor X. B. Yu, Dr. A. Calka, and Dr. D Wexler for their invaluable assistance and suggestions.

I would like to express my gratitude to my colleagues Dr. G. Peleckis, Dr. S. Aminorroaya, Dr. Z. G. Huang, J. Mao, C. K. Poh, and M. Ismail for all their support and encouragements.

I also would like to thank all non-teaching staff members, particularly Darren Attard, Joanne George, Ron Kinnel, and Virginie Schmelitschek for their invaluable assistance in many regards. Special thanks go to Dr. Tania Silver for her critical help thorough error checking of my papers and this thesis.

I wish to express my heartfelt thanks to my lovely mother, brother, and sisters for their care, spiritual support, and fondness towards me.

Finally, and the most importantly, I am indebted to my wife, Masi, who cheered me up whenever I needed it. This thesis would not have been possible without her trustworthy love, patience, and encouragement. I owe her my deepest appreciation.

Abstract

Hydrogen is the best energy carrier for all kinds of environmentally friendly energy sources such as wind and solar energy. Among the various types of material for hydrogen storage, magnesium is one of the most promising candidates. The objective of this thesis is enhancement of the hydrogen storage properties of MgH_2 using different kinds of catalysts and ball-milling methods.

To increase defects and decrease both grain size and agglomeration, and therefore hydrogen diffusion paths, a hard nanopowder, SiC, was added to MgH_2. Less than 10wt% of SiC improved the sorption kinetics, while more than 10wt% SiC blocked Mg particles and had negative effects.

In addition to increasing defects and extra improvement of the surface area, the effects of doping Ni into the MgH_2-SiC system were investigated. Additional improvement in sorption kinetics and hydrogen capacity was achieved by this combination. The rate-limiting step changed from ‘‘surface controlled’’ for the pure sample to ‘‘nucleation and three-dimensional growth of the existing nuclei’’ for the MgH_2-SiC-Ni sample.

As Ti-based body-centred cubic (BCC) alloys have shown superior catalytic effects on the hydrogen storage properties of magnesium, a new type of BCC, $Ti_{0.4}Mn_{0.22}Cr_{0.1}V_{0.28}$, was ball milled with MgH_2 with different ball-to-powder weight (BPWR) ratios. The conversion of magnesium to magnesium hydride was much faster in presence of this

catalyst. Both desorption temperature and hydrogen absorption/desorption kinetics were improved by adding the catalyst and increasing the BPWR.

With the aim of improving the different steps of hydrogen sorption in Mg, a combination of ball milling $Ti_{0.4}Mn_{0.22}Cr_{0.1}V_{0.28}$ and multi-walled carbon nanotubes with MgH_2 was investigated. $Ti_{0.4}Mn_{0.22}Cr_{0.1}V_{0.28}$ improved two steps of hydrogen absorption: dissociation of hydrogen molecules and transformation of hydrogen atoms into the Mg/BCC interface to form MgH_2 particles. The effects of CNTs could include promotion of Mg aggregation along the grain boundaries and facilitated penetration of hydrogen atoms into interior layers of Mg grains. These effects were in reverse order during hydrogen desorption.

With the aim of finding optimised fabrication conditions for the Mg-Ni system, various fabrication methods such as casting, ball-milling, and the combination of casting and ball milling, and their influence on the hydrogen sorption properties of Mg-6 wt% Ni alloys were studied. Preparation of *Mg + Ni* by ball milling led to remarkable hydrogen sorption properties in comparison with casting as a consequence of introducing defects and active sites during the ball milling.

Key words: hydrogen storage, magnesium hydride, ball milling, catalyst, silicon carbide, nickel, Ti-based body centred cubic, carbon nanotube

Table of Contents

List of Tables

List of Figures

Chapter 1

Introduction

Nowadays, crude oil, natural gas, and coal are the main sources of energy supply in our daily lives, particularly in transportation, while the world's energy demand is increasing significantly. On the other hand, utilizing these carbon-based energy sources has two unavoidable disadvantages. Firstly, they will be depleted in the near future. Secondly, their main by-product, carbon dioxide, is the most important greenhouse gas, which is causing perhaps our most serious common predicament: global warming. Therefore, sustainable, clean, and environmental friendly energy sources, such as solar and wind energy, are essential. However, for using the energy produced by these sources in final applications, an energy carrier is necessary. This energy carrier should be safe, capable of easy conversion, and convenient for use in applications. Consequently, the best candidate for this purpose is *hydrogen*. Hydrogen can be transported and distributed to a wide range of applications, such as transportation, electric power generation, and so on. This is what is meant by the term *hydrogen economy*.

On the other hand, there are some serious technical drawbacks in hydrogen production, storage, and usage. There are different processes that can be used for hydrogen production, such as steam reforming and water electrolysis. Furthermore, the best method for hydrogen utilization in the transportation sector is the fuel cell. However, the main drawback in proceeding with the hydrogen economy is hydrogen storage, particularly for mobile applications. After a long investigation, the US Department of Energy (DOE) has set requirements for on-board applications, which are the targets for

researchers in this area. All aspects of the requirements have been specified in the DOE's targets, such as storage capacity, volumetric and gravimetric capacity, hydrogenation and dehydrogenation, reversibility, and safety.

In Chapter 2, methods of hydrogen production and utilization are briefly explained, while its storage is discussed in detail, particularly storage in the solid state. In addition, the efforts of other researchers to improve hydrogen storage properties in different materials have been summarized. As the central focus of this thesis is on magnesium hydride, at the end of this chapter, a brief history of this compound, its crystal structure, the methods of preparation, and the thermodynamics and hydrogen storage properties of this material have been described in more detail, and published works on improvement of its hydrogen sorption properties are reviewed.

Materials used in the experiments and the equipment which is used for sample preparation and different kinds of measurements, such as ball-milling, X-ray diffraction, etc., have been explained in Chapter 3.

Based on the reports described in Chapter 2, the diffusion of hydrogen atoms into the magnesium lattice is one of the critical aspects of formation of MgH_2 with good sorption kinetics. Shorter and easier hydrogen diffusion paths are available for particles which are produced by ball milling, because they have more fresh surface area and activation sites. In Chapter 4, a new method for decreasing grain size and agglomeration, and thus increasing fresh surface area is studied. The principle consists of adding particles of a hard nanopowder, SiC, to act as nanoballs during ball milling. The results show that a small amount (up to 5wt%) of SiC has noticeable effects on

MgH_2 and improves the sorption kinetics significantly, while increasing the proportion of SiC to more than 10wt% gives rise to negative effects.

As SiC is not a catalyst, and its effects relate to improvement of the surface area, it was expected that a combination of SiC with a good catalyst, such as Ni, could result in extra enhancement of the hydrogen storage properties of Mg. This was the motivation for fabricating and analysing results on MgH_2-SiC-Ni, which is described in Chapter 5. The results have indicated that there is additional improvement in comparison with the sample without Ni. In this chapter also, the kinetic behaviour of the sample of Mg-5wt%SiC-10wt%Ni is studied, and the results show that the rate-limiting step has changed from ‘‘surface controlled’’ to ‘‘nucleation and three-dimensional growth of the existing nuclei’’.

Ti-based body-centred cubic alloys have shown superior catalytic effects on the hydrogen storage properties of magnesium by acting as a catalyst for hydrogen molecule dissociation and then as a diffusion path for hydrogen atoms. Therefore, in Chapter 6, a new kind of body-centred cubic alloy, $Ti_{0.4}Mn_{0.22}Cr_{0.1}V_{0.28}$ was ball milled with MgH_2 with different ball-to-powder weight ratios (BPWR), and the hydrogen storage properties and the structural changes of the composites have been studied.

Carbon nanotubes (CNTs) have shown remarkable effects on the hydrogen storage properties of Mg-based alloys. These effects were additionally improved when CNTs were combined with transition metals. Based on the results in Chapter 6, the catalytic effects of $Ti_{0.4}Mn_{0.22}Cr_{0.1}V_{0.28}$ were better than those of transition metals, and therefore, it was possible that a combination of CNTs and $Ti_{0.4}Mn_{0.22}Cr_{0.1}V_{0.28}$ could lead to a

great enhancement of hydrogen dissociation and diffusion into Mg nanoparticles. Based on this expectation, in Chapter 7, to complete the results achieved in the previous chapter, two samples of Mg+10wt% $Ti_{0.4}Mn_{0.22}Cr_{0.1}V_{0.28}$ were fabricated, and 5wt% CNTs were added to one of them. The hydrogen storage properties of the prepared samples were investigated and compared with the performance of pure MgH_2. The results confirmed our expectations.

The investigation in Chapter 8 is a comparison between 2 methods of fabrication of MgH_2+Ni: casting and ball milling. The possibility of placement of the catalyst particles in deeper layers of Mg particles by ball milling after casting was also investigated. For this purpose, in this chapter, Mg-6wt% Ni was first prepared by melt processing and casting, the obtained materials were then ball-milled by both planetary and reactive ball milling, and finally, the results are compared with those of as-milled Mg+6wt% Ni nanopowder.

In Chapter 9, the main results and achievements are summarized, followed by the list of references and acronyms. This thesis is closed with a list of my papers that were published during my PhD work.

Chapter 2

Literature review

2.1 Background

Since 1769, when James Watt invented the steam engine and then by developing the internal engine, coal gradually became the most important source of energy in the western world. With increasing popularity of automobiles and other self-propelled vehicles at the beginning of the 20th century, crude oil took over and became the source of main energy supply in the industrial nations. Natural gas, after World War II, and nuclear power in 1960 were added to the group of conventional energy sources. These two sources could not break the market leadership of coal and crude oil and, nowadays, more than 85 percent of world primary energy demands are provided by these the traditional sources. Figure 2.1 shows the amount of oil production and illustrates that the production rate increased exponentially after World War II. Undoubtedly, this increase will continue in the future.

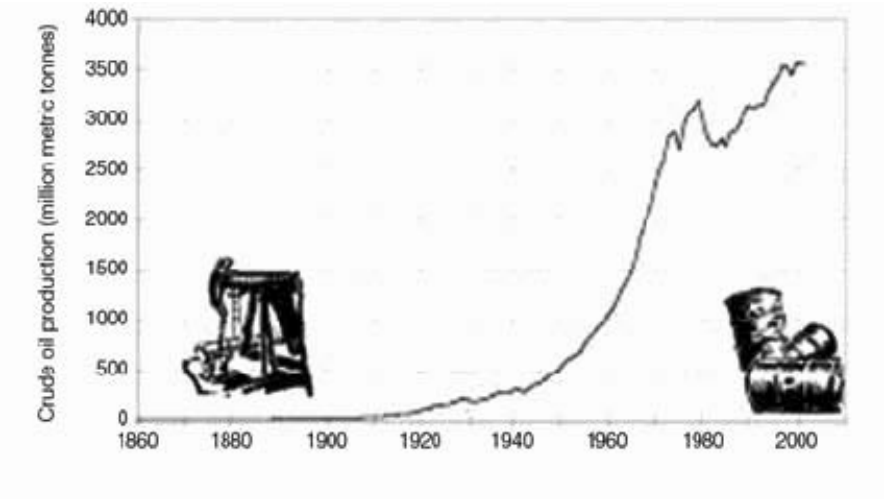

Figure 2.1. Evolution of Annual Crude Oil Production [1].

It is expected that the world population will reach 8 billion by 2030 [2], and, at the same time, the world's energy requirements will increase by a factor of 2.3-4 compared to 1990 [3]. This will exacerbate the problems of today's high energy expenditure and its consequences, such as the greenhouse effect and the rapid depletion of fossil energy resources. On the other hand, fossil fuel based energy carriers, such as natural gas, petroleum, and coal, needed many years of development. Due to increasingly difficult manipulation of the fossil fuel reservoirs, future extraction will be more and more complicated, technically challenging, and risky, and therefore, much more expensive than today. By unimpeded use of fossil fuel, all available economically viable sources of petroleum and natural gas will be exhousted within the next few decades, and, as shown in Table 2.1, only coal reserves will be obtainable for a longer period of time.

Table 2.1 Fossil fuel reserves [4].

	Crude Oil	**Natural Gas**	**Coal**
Proven reserves	142.7 billion t	155.8 billion m^3	948 billion t
Production in 2002	3.56 billion t	2.53 billion m^3	4.82 billion t
Reserves/production rate	41 years	61 years	204 years
Unproven additional reserves	84 billion t	217 billion m^3	6668 billion t
Accumulated production	128.2 billion t	69.6 billion m^3	

The result of burning fossil fuels and biomass is anthropogenic carbon dioxide (CO_2), which is the most significant greenhouse gas and contributes 61 percent of the greenhouse effect. Fifteen percent of this amount is the share of biomass and 46 percent is the share of fossil fuels. The concentration of CO_2 in the outer atmosphere has already risen from 280 parts per million by volume (ppmv) in 1850 to 372 ppmv in 2002 [5]. In addition both production and utilization of fossil fuels causes the majority of methane (CH_4) emissions. In comparison, the concentration of methane in the atmosphere is less than 1 percent of that for CO_2; however, the global warming potential of methane is much higher than that of CO_2 [5].

Carbon dioxide emissions from fuel combustion are not equal per capita. Figure 2.2 shows this amount for different regions.

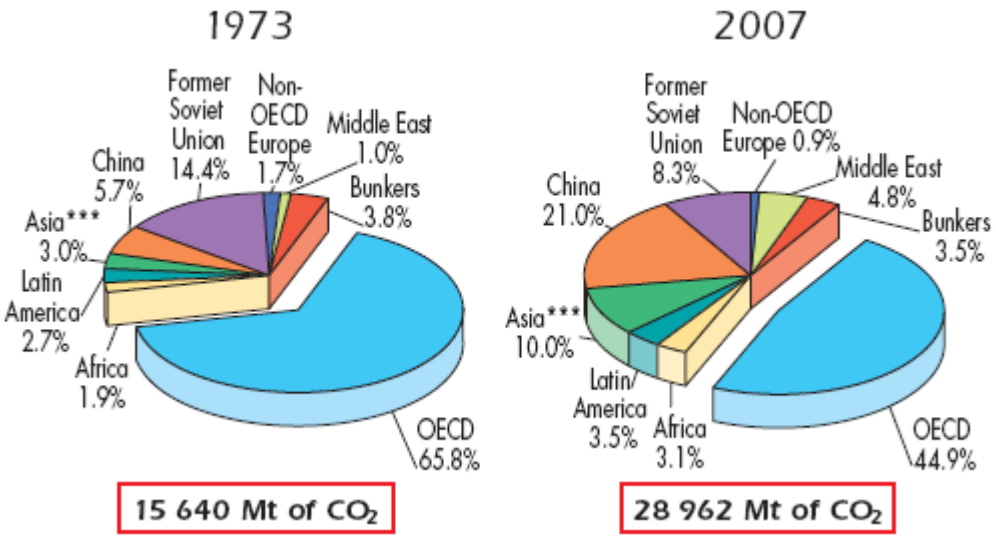

Figure 2.2 1973 and 2007 regional shares of CO_2 emissions per capita [6].

Therefore, both the depletion of fossil energy resources and global warming, as a result of increasing greenhouse gases, necessitate renewable and environmentally friendly energy sources.

Since the focus of this thesis is on materials for hydrogen storage, and the greatest impact of hydrogen is in the *transportation* sector, it is necessary to discuss transportation as one of the most important energy consumers and its share of global warming.

2.1.1 Transportation

Transport plays an important role in global energy-related CO_2 emissions. Although it is not the main CO_2 supplier, it is a noteworthy factor. Transport's shares of CO_2 emissions are growing persistently because people require more and improved mobility, and so the number of vehicles is going up. It is expected that the rate of increase of per capita CO_2 emissions will also rise from other sectors. From 1990 to 2003, the emissions of the transport sector increased 31% (1412 mt) worldwide and 26% (820 mt) in the Organisation for Economic Co-operation and Development (OECD) countries, where it is slowly, but surely, increasing. This share is highest in the more developed countries of the OECD [7]. Figure 2.4 shows transport's share of CO_2 emissions.

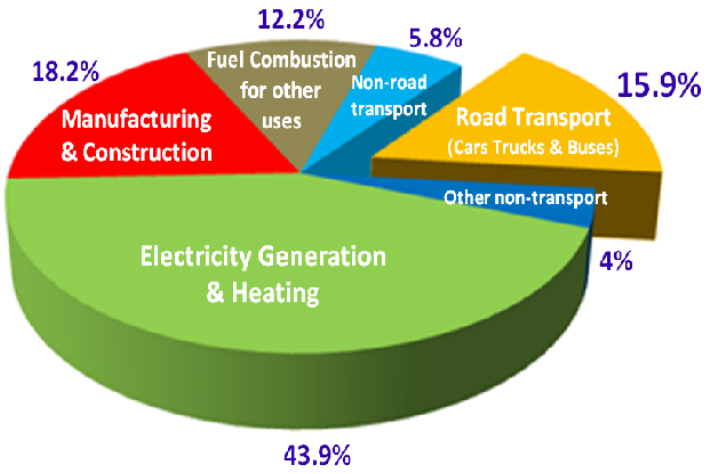

Fig. 2.3 Transport percentage shares of CO_2 emissions in 2005 [8].

To accomplish the necessary deep cuts in greenhouse gas emissions is impossible without the participation of transport. As a result, legislators concerned about both transport and climate change are paying ever more attention to the transport sector.

An integrated approach for emission abatement includes:

1- Delivering a majority of innovative vehicles with higher efficiency engines.
2- Improving driving behaviour.
3- Reducing congestion by decreased travel and development of public transportation.
4- Increasing CO_2-related taxation.
5- Development of renewable alternative fuels.

Among these methods, developing a renewable and clean fuel is the most important one.

2.2 Energy sources and carriers

There are some primary energy sources with the characteristics of renewable and clean energy, such as solar, wind, geothermal energy, hydropower, and wave energy. The uses of all of these energy sources have some advantages and disadvantages. For example, hydropower is reliable and cheap, and, of course, very clean. However, it has a negative effect on ecosystems everywhere that the generators are based. To reduce this impact, the generators should be installed in proper locations, and improvements in design and operation are necessary.

Solar and wind energy, and also waves are carbon free and limitless in nature, and their use can noticeably decrease greenhouse gas emissions. Their major problem is that they are not accessible all the time. For all types of new energy sources, there is one common

requirement: they all need a high capacity, low-cost, and long cycle life energy carrier. On the other hand, about the three-quarters of the mentioned primary energy from these renewable sources is going to be ultimately used as fuel, however, none of them, in contrast with the fossil fuels, can be directly used as a fuel, as they require an energy carrier.

Therefore what we need is a production of the best *"fuel"* for the future. Although there are many candidates, such as gasoline, methane, ethanol, and hydrogen, we can not choose one of them without considering the following conditions [9]:

1- Convenient for transportation: All kinds of vehicles (cars, airplanes etc.) must carry their fuel for a short or long distance. Therefore it is essential that the transportation fuel be very light with as low a volume as possible.
2- Capability for easy conversion: All fuels, finally, must be converted to other forms of energy such as mechanical and electrical energy. Any new proposed fuel must be suitable for these conversions at the user end.
3- High efficiency: The new transportation fuel should be converted to the desired energy form with higher efficiency than other fuels.
4- Safe: Both aspects of safety - toxicity and fire hazard properties - must be minimized for the future fuel.

2.3 Hydrogen: the best candidate

As mentioned above, there are several candidate energy carriers, such as synthetic gasoline, methane, and hydrogen. The following reasons prove that hydrogen is the best energy carrier for all purposes, particularly for future fuel use.

1- The motivity factor, $\Phi_{m,}$ is a factor based on the requirements for a fuel to be convenient for transportation [10]. Carrying a fuel is easer if its motivity factor is higher. Table 2.2 shows that between the different kinds of fuels, hydrogen, in both liquid and gas phases, has the best Φ_m. This is one reason why hydrogen is used as a fuel in space programs. Definitely, however, this transportation will be much easier if we can store hydrogen in a solid phase such as a metal hydride.

Table 2.2. Motivity factors for different fuels [11].

Fuel	Gasoline	Ethanol	Methanol	Natural gas	LH_2	GH_2
Motivity factor	0.76	0.23	0.37	0.75	1	1

2- All kind of fossil fuels can only be converted through combustion, whereas hydrogen can be converted through flame and catalytic combustion, chemical reaction, and electrochemical processes [12].

3- The utilization efficiency factor, Φ_u, the ratio of the fossil fuel utilization efficiency η_f to the hydrogen utilization efficiency η_H, is presented in Table 2.3 for different applications. As is shown, hydrogen is capable of being converted to the required energy form with more efficiency than fossil fuels [13].

4- Water and water vapour, which are the main combustion products of hydrogen, are not toxic. On the other hand, in the case of fire hazards, lower density and higher specific heat cause a fuel to be safer. Consequently, by considering these factors, hydrogen becomes the safest fuel in comparison with other suggested fuels such as methane and gasoline [11].

Table 2.3 Comparison between Φ_us of fossil fuels and hydrogen [13].

Application	Utilization efficiency factor $\phi_u = \eta_F / \eta_H$
Thermal energy	
Flame combustion	1.00
Catalytic combustion	0.80
Steam generation	0.80
Electric power, fuel cells	0.54
Surface transportation	
Internal combustion engines	0.82
Fuel cells/electric motor	0.40
Subsonic jet transportation	0.84
Supersonic jet transportation	0.72
Weighted average	0.72
Hydrogen utilization efficiency factor	1.00
Fossil fuel utilization efficiency factor	0.72

In addition to the above-mentioned important factors, hydrogen is the simplest, lightest, and third most abundant element in the world. All these conditions make hydrogen the best candidate for fuel in future vehicles. However, there are some serious technical drawbacks in its *production*, *utilization,* and the important steps between them: *hydrogen storage* or *transportation.*

Hydrogen can be produced from fossil fuel resources, such as natural gas and coal, or from renewable resources, such as sunlight, wind, or hydropower. Moreover, there are a variety of process technologies that can be used for this purpose, including steam reforming [14], gasification of coal [15], water electrolysis [16], thermochemical [14], and photobiological and photobiochemical [17] processes. Besides the two first methods mentioned, which, unfortunately, are not environmentally friendly, the other processes currently can not be used for hydrogen generation in large quantities. Accessibility of feedstocks, the development of technology, policy issues, and the production costs will

influence the production of significant amounts of hydrogen. However, these drawbacks will be solved over time.

Hydrogen can be used in both combustion engines and fuel cells. Although hydrogen combustion engines present obvious advantages over present engines in term of performance and cost, one of its by-products, NO_x, displays toxic effects, the same as for the combustion of fossil fuels. Fuel cells are pollution free with non-toxic by-products. A fuel cell [18] is an electrochemical device that converts chemical energy into electricity. Fuel cells can be categorized as portable, stationary, or transportable depending on their sizes and functions, and the focus of this section is on the latter.

A fuel cell, as is shown in Figure 2.4, consists of an electrolyte layer in contact with two electrodes, an anode and a cathode, on each side [19]. The process of energy conversion in the most promising fuel cell for transportation, called the Proton Electrolyte Membrane (PEM) fuel cell, consist of the following steps:

1- Hydrogen gas flows through the channels to the anode.
2- Hydrogen molecules are separated into protons and electrons by the effect of a catalyst.
3- The membrane acts as a filter and allows only the protons to pass it.
4- The external circuit is the path of the separated electrons, and this is the electricity which can be used to power a motor.
5- The returned electrons from the circuit react with the protons and oxygen gas, drawn from the exterior air, at the cathode and form water while producing heat as well.

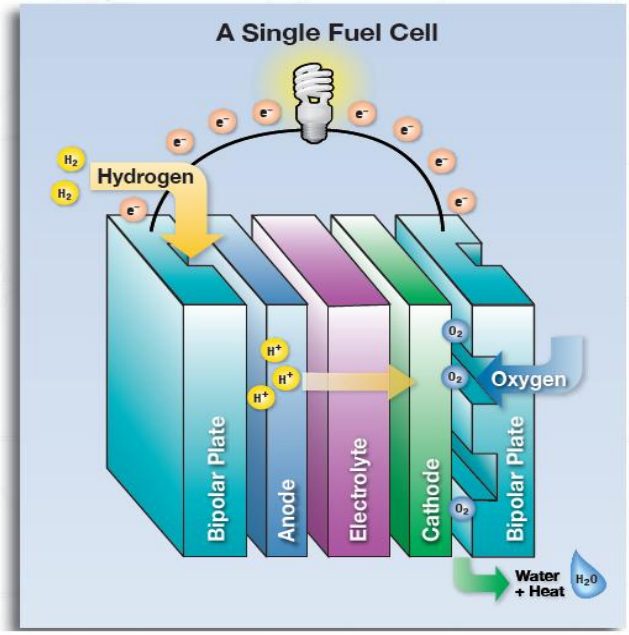

Fig 2.4 Schematic diagram of a PEM fuel cell [19].

2.4 Hydrogen storage

Hydrogen storage is the main bottleneck to the realization of the hydrogen economy. There are various technologies (which are explained in the next section of this chapter) for this purpose, and, for mobile application, the selected technology should be dense, safe, inexpensive and lightweight. The Department of Energy of the United States (the US DOE) has set the operating requirements for this discussion by preparing targets for the years 2010 and 2015 (Table 2.4).

Table 2.4 US DOE hydrogen storage targets for mobile application [20].

Storage Parameter	Units	2010	2015	Ultimate
System Gravimetric Capacity: Usable, specific-energy from H_2 (net useful energy/max system mass)	kWh/kg (kg H_2/kg system)	1.5 (0.045)	1.8 (0.055)	2.5 (0.075)
System Volumetric Capacity: Usable energy density from H_2 (net useful energy/max system volume)	kWh/L (kg H_2/L system)	0.9 (0.028)	1.3 (0.040)	2.3 (0.070)
Storage system cost (& fuel cost)	$/kWh net ($/kg H_2) $/gge at pump	TBD (TBD) 3-7	TBD (TBD) 2-6	TBD (TBD) 2-3
Durability/Operability				
• Operating ambient temperature	ºC	-30/50 (sun)	-40/60 (sun)	-40/60 (sun) -40/85
• Min/max delivery temperature	ºC	-40/85	-40/85	
• Operational cycle life (1/4 tank to full)	Cycles	1000	1500	1500
• Min delivery pressure from storage system; FC=Fuel Cell, ICE= internal combustion engine	bar (abs)	5FC/35 ICE	5FC/35 ICE	3FC/35 ICE
• Max delivery pressure from storage system	bar (abs)	12	12	12
• Onboard Efficiency	%	90%	90%	90%
• "Well" to Powerplant Efficiency	%	60%	60%	60%
Charging/discharging Rates				
• System fill time (for 5-kg H_2)	min	4.2 min	3.3 min	2.5 min
• Minimum full flow rate	(Kg H_2/min)	(1.2 kg/min)	(1.5 kg/min)	(2.0 kg/min)
• Start time to full flow (20ºC)	(g/s)/kW	0.02	0.02	0.02
• Start time to full flow (-20ºC)	s	5	5	5
• Transient response 1 0%-90%	s	15	15	15
and 90% -0%	s	0.75	0.75	0.75
Fuel Purity (H_2 from storage)	% H_2	SAE J2719 and ISO/PDTS 14687-2 (99.97% dry basis)		
Environmental Health & Safety				
• Permeation & leakage	Scc/h	Meets or exceeds applicable standards		
Toxicity	-			
Safety	-			
Loss of useable H_2	(g/h)/kg H_2 stored	0.1	0.05	0.05

There are basically five known main storage methods at present which *might* satisfy the requirements of on-board systems after improvement:

1- High pressure gas storage

2- Liquid hydrogen

3- Physisorbed hydrogen

4- Chemically bound hydrogen

5- Hydrolytic evolution of hydrogen

Every method has its advantages and disadvantages and currently, none of them meets the US DOE target requirements. Table 2.5 shows a comparison of the hydrogen storage characteristics of different methods.

Table 2.5 Comparison of main characteristics of various hydrogen storage methods [21].

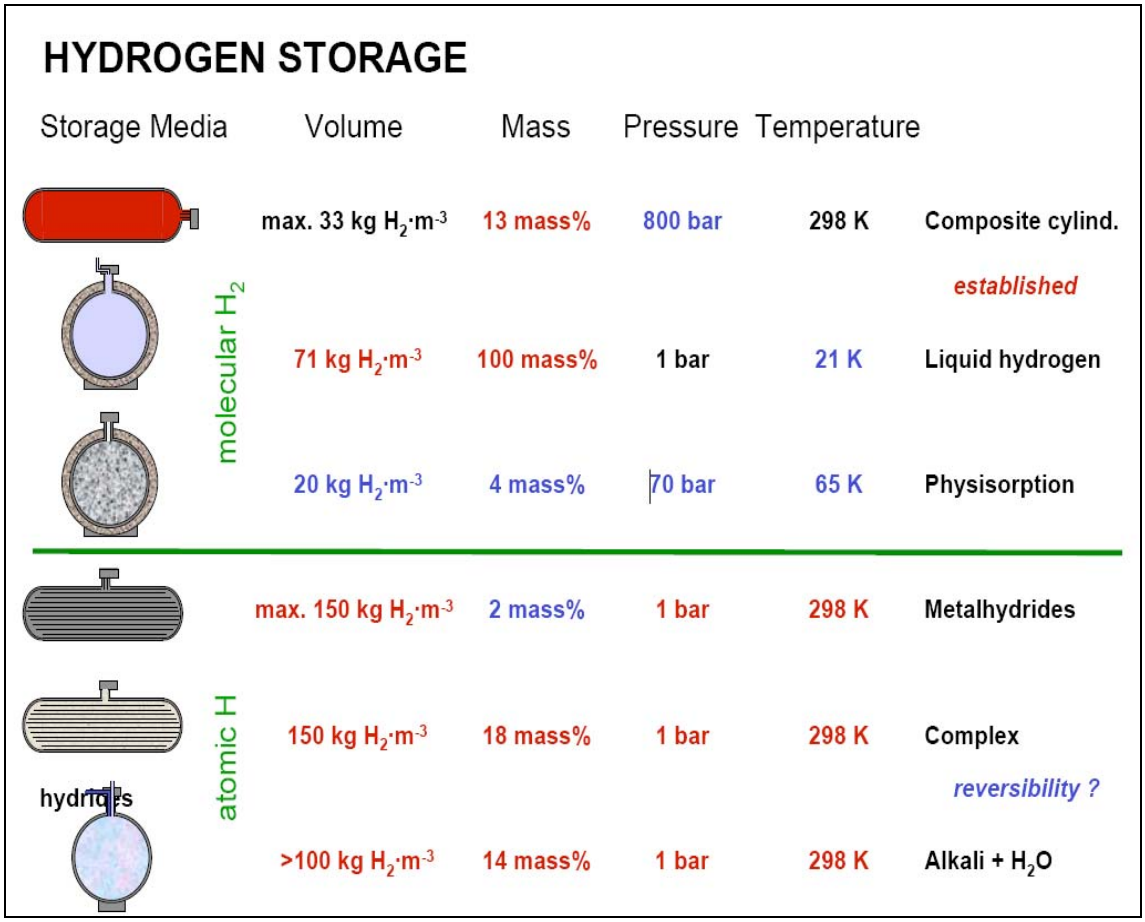

In the following section the most important aspects of each of the above-mentioned methods, and its strong and weak points are explained.

2.4.1 High pressure gas storage

The most common hydrogen storage method, for both stationary and on-board applications, currently is via pressurised cylinders to store hydrogen. As this technique merely requires a compressor and a pressure vessel, it is the simplest and, at present, the cheapest method. However there are some obstacles too. The main drawback is its low volumetric capacity. Working pressure for a typical composite cylinder, shown in Figure 2.5, can be either 350 or 700 bar. The gravimetric density for a 700 bar tank is 4.5 wt% which is not far from DOE 2010 target, however, its volume density is 25 $kgHm^{-3}$ which is close to half of the target [22]. Increasing the pressure seems a possible approach to solve this problem, however, on considering practical and safety issues it is less likely that higher pressure can be used for vehicle applications.

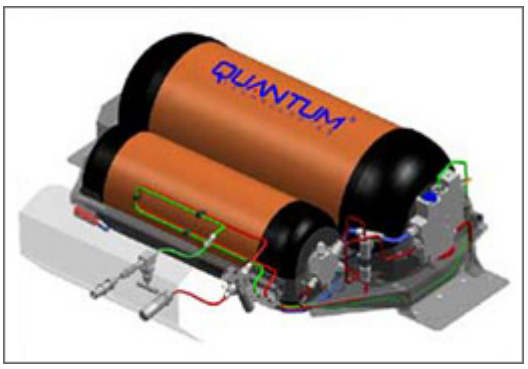

Fig 2.5 Typical compressed hydrogen storage tank [23].

Another issue in using high pressure gas storage is the limited space available in a vehicle, particularly a family car. Such gas storage not only will constrict the passenger and luggage space and, as a consequence, introduce extra weight and costs, but also is very difficult to manufacture because of the extra complexity in the filament winding process.

Although there have been many investigations to improve the design of both vehicles and storage tanks to use the high pressure hydrogen storage method, it seems unlikely to be able to meet the US DOE target.

2.4.2 Liquid hydrogen

Liquid phase of hydrogen can be stored in a cryogenic tank (Figure 2.6) at 20 K and 1 atm pressure. Under these conditions the volumetric density is 70.8 kgm^{-3} which gives an acceptable volumetric capacity; 70.5 $kgHm^{-3}$ [24]. This capacity is much higher than for pressurised hydrogen gas (25 $kgHm^{-3}$) and, therefore, the driving range using liquid hydrogen is longer than for the gas storage one [25].

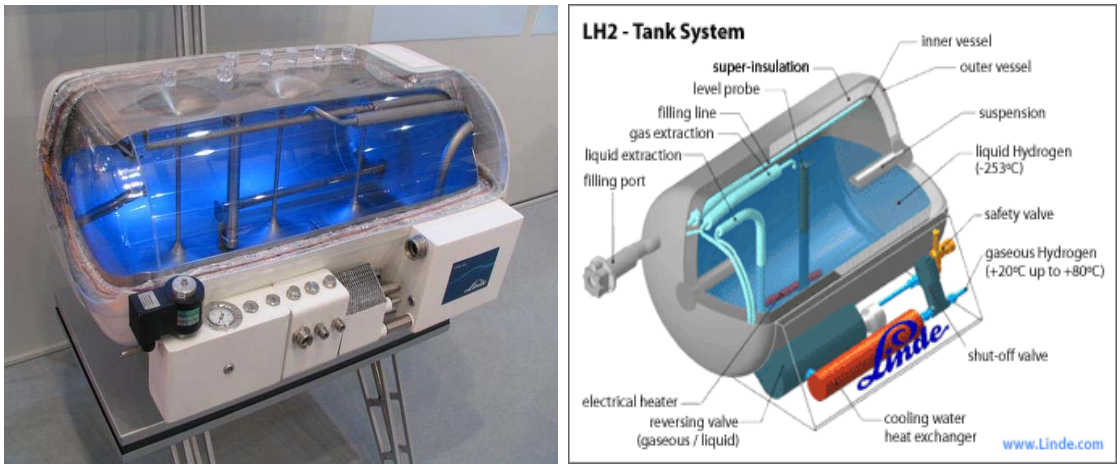

Fig. 2.6 A 120 litre liquid hydrogen tank (left) and its schematic structure (right) [26].

However, there are two major problems with this method. The first one is the low efficiency of the liquidizing process. There is unavoidable energy loss during this process, even inside a tank with a perfect insulation [25]. The second drawback is the boil-off of hydrogen, which is a result of thermal radiation from the environment and thermal conduction through cables and fixtures. This is undesirable for mobile

application, because the tanks could have serious safety issues and may allow an explosive combination to form in an enclosed space [27].

The low efficiency of the process, the boil-off of hydrogen and the super-insulation nneded are critical issues for the storage of hydrogen by liquidizing and make it unsuitable for portable applications.

2.4.3 Solid state hydrogen storage

The storage hydrogen in solid state materials could be the safest and the most advantageous method for hydrogen storage, in terms of the lowest cost and highest efficiency. This method includes physisorption of hydrogen molecules on materials with high surface area, such as carbon nanotubes, and chemisorption in compounds such as MgH_2 and complex hydrides.

2.5 Hydrogen storage by physisorption

In this method, hydrogen molecules are held on the surface by a van der Waals interaction and without dissociation (Fig 2.7). The strength of this interaction is very weak and so, the enthalpy of formation for this process is less than 10 kJ/mol. Therefore, physisorption (adsorption) of hydrogen gas on a surface by this technique means that very low temperature, in the range of the temperature of liquid nitrogen, is necessary.

Porous materials, such as carbon nanotubes (CNTs), zeolites, metal organic frameworks (MOFs), and graphite nanofibers (GNFs), have received substantial interest for this purpose because of their high surface areas.

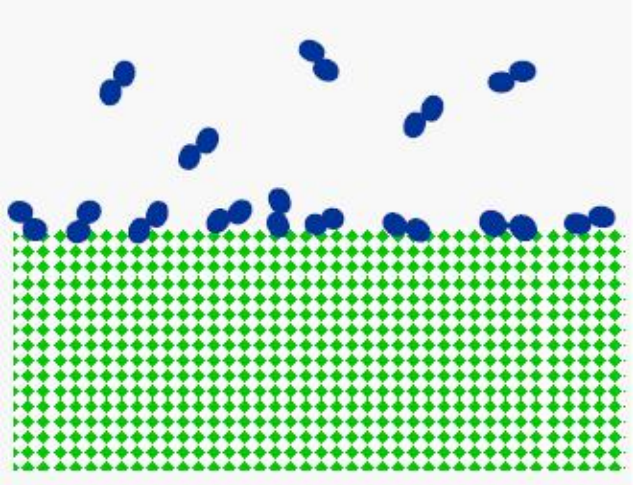

Fig. 2.7 Schematic physisorption on surface [21].

2.5.1 Carbon nanotubes

A carbon atom can bind with three, five, or seven of its neighbours with covalent bonds, leading to the creation of diamond, graphite, activated carbon, carbon nanofibers, fullerenes, single wall carbon nanotube (SWCNT), and multiwall carbon nanotube (MWCNT).

A (SWCNT) consists of a single graphite sheet rolled up in a seamless cylinder with a radius of a few nanometers [28]. As is shown in Figure 2.8, both ends of a typical SWCNT are usually closed with fullerene-like hemisphere caps when synthesized. The outer radius of a CNT ranges from 20 to 200 Å, and the inner oneis between 10 and 30 Å [29].

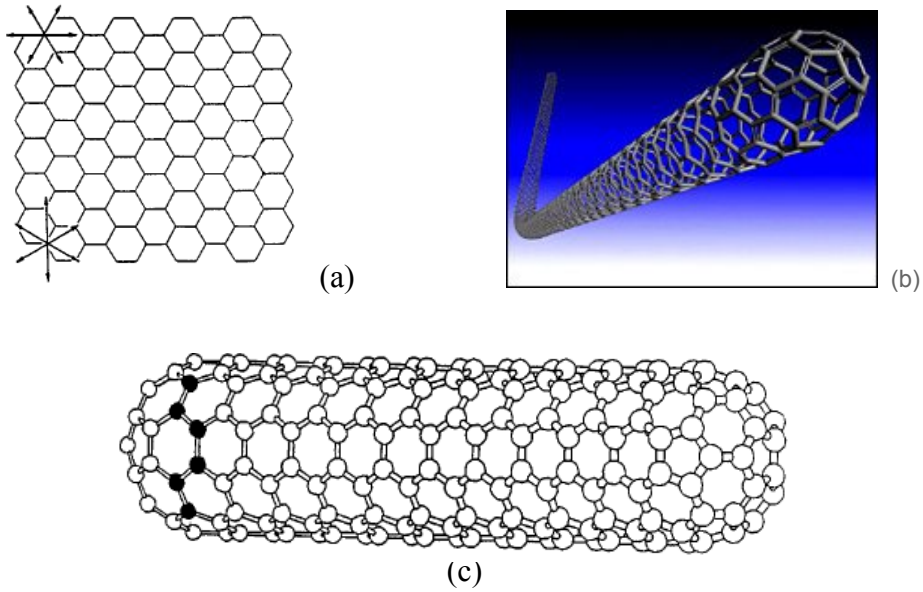

Fig 2.8 (a) Piece of a graphene sheet, (b) and (c) models of a carbon nanotube [28].

There are four adsorption sites on a SWCNT: internal or tube sites, interstitial sites, which are between nanotubes within the bundle, peripheral sites between pairs of SWCNTs at their surfaces, and the external surface sites (Fig. 2.9) [30]. In physisorption, at a given temperature, the amount of adsorbed hydrogen is a function of the pressure applied on the system, so hydrogen can penetrate into the internal sites only at high pressure. In this case, the tube diameter must be 0.7 nm [29].

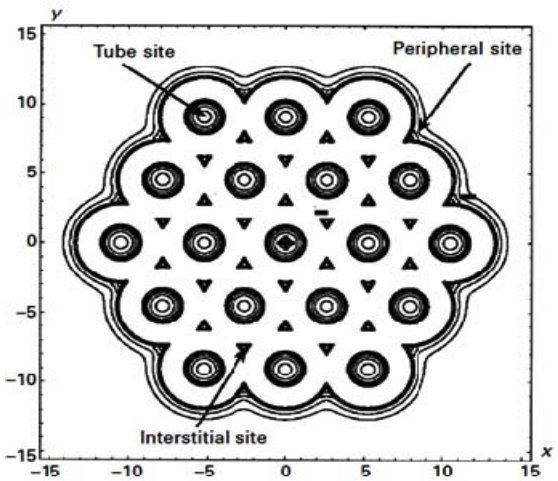

Fig 2.9 Adsorption sites in bundles of single wall nanotubes [30].

A multiwall carbon nanotube (MWCNT) consists of several concentric rolls of graphite sheets and a distance between two layers of about 0.35 nm [29]. It can be prepared by different methods, such as laser ablation from a graphite target, chemical vapor deposition, and arc discharge.

The mechanism and the improvement of hydrogen storage properties by CNTs are major interests of researchers. Dillon et al. published the first experimental results on the hydrogen storage properties of SWCNT by the temperature programmed desorption (TPD) method [31]. Their procedure consists in measuring by a mass spectrometer the hydrogen desorbed by a carbon sample during a heating run. Since then, very many groups have researched both SWCNT and MWCNT systems by altering the methods of preparation and doping a variety of elements into them. As expected, there are large discrepancies in their claimed hydrogen storage capacities. Fan et al. observed a hydrogen uptake of 10-13 wt% in MWCNTs at room temperature and a pressure of 110 atm by the volumetric method [32]. This group also obtained a capacity of 4.2 wt% for SWCNTs [33]. However, none of these results were confirmed under the same conditions by any other groups. In contrast, Poirier et al. [34] found only 0.2 wt% capacity under ambient conditions for SWCNTs. Hou et al. [35] showed that the maximum hydrogen storage capacity of MWCNTs was 4.6 wt% at 293 K and 135 atm, while Li et al. [36]reported a range from 1.29 to 3.98 wt% at room temperature (RT).

Different reports exist at cryogenic temperature too. Ye et al. [37] found a hydrogen adsorption of more than 8 wt% in SWCNTs at 77K and a pressure of 120 atm, while this quantity was 4 wt% at 1 bar for Poirier et al. [34].

Briefly, most of the current research has demonstrated that the hydrogen storage capacity of CNTs is less than 1 wt% under ambient conditions [38] and up to 2.5 wt% under cryogenic conditions, depending on the sample preparation [39-42].

2.5.2 Zeolites

Zeolites are crystalline aluminosilicate defined by a network of pores and channels of molecular dimensions (Fig 2.10). The general formula of a zeolite is: $M_{x/n}[(AlO_2)_x(SiO_2)_y]\cdot mH_2O$, where cation M of valance n balance the negative charge on the framework [43, 44] .

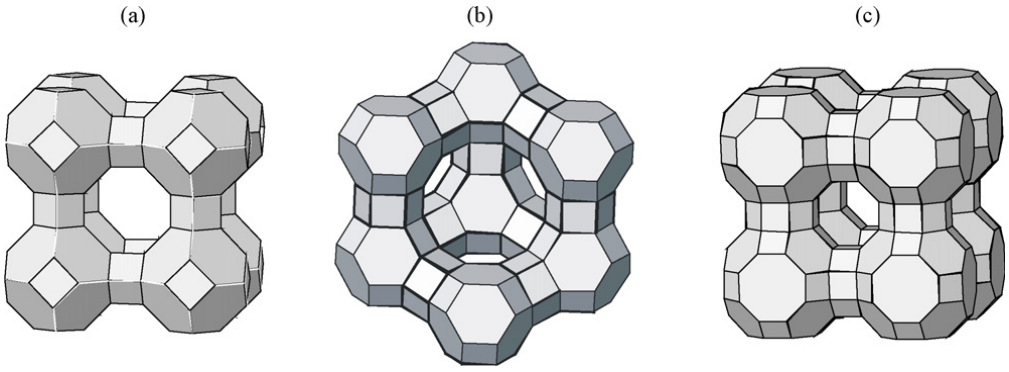

Fig. 2.10 Framework structures of zeolites: (a) zeolite A, (b) zeolites X and Y, and (c) zeolite Rho [44].

As zeolites are cheap, available, easy to synthesize, and safe to use, they are of interest as hydrogen storage materials. Hydrogen can be stored in zeolites by encapsulation (at elevated temperatures and pressures) or physisorption [45-47]. In 1998, Kazansky et al. [48] studied the hydrogen adsorption at cryogenic temperature of zeolites with different isostructures, such as NaY and NaX with different Si/Al ratios. The maximum hydrogen storage capacity was 1.2 wt% for NaX, with a Si/Al ratio of 1.05 at 0.6 atm. Darkrim et

al. [49] reported a capacity of 1.2 wt% at room temperature and a pressure of 700 atm in NaA. The hydrogen adsorbed by ZSM5 zeolites reported by Nijkamp et al. [50] at 77 K was 0.72 wt%. Forster et al. [51] investigated hydrogen adsorption on the zeolite nickel phosphates VSB1 and VSB5 at 77 K. They believed that the adsorption in the latter one (~1 wt% at 1 atm) was related to the presence of a coordinatively unsaturated framework of Ni^{2+} cations. The highest hydrogen storage capacity in zeolites was reported by Du and Wu [52] in NaX, which was 2.55 wt% at 77 K and 40 atm.

2.5.3 Metal Organic Frameworks (MOFs)

MOFs consist of metal ions linked by organic donor molecules called ligands. As there is a vast diversity of both ligands and metal ions, different kinds of MOFs with different properties exist. MOF-5, MOF-74, MOF-177, HKUST-1, MIL-100, and MIL-101, as shown in Fig. 2.11, have demonstrated outstanding performance in hydrogen storage and even adsorption of other gases [53].

Rosi et al. [54] reported an initial hydrogen storage capacity of 4.5 wt% at 77 K and 1 atm on MOF-5, however, this result was an overestimation, which was corrected by Rowsell et al. [55] to 1.32 wt%. Wong et al. [56] fabricated a series of MOFs at 77 K, across a 25- 80 atm range of pressure, and found 5 wt% adsorbed hydrogen at 50 atm by MOF-5. Hydrogen storage on HKUST-1 was investigated by Xiao et al. [57], on unsaturated copper sites after dehydration. Their results showed capacities of 2.27 wt% and 3.6 wt% at 77 K, and 1 atm and 10 atm, respectively. The best hydrogen storage capacity was reproducibly obtained from MOF-177, ~7.5 wt% at 70 bar [53]. Storage capacity at room temperature, either based on experimental [58] or theoretical [59]

results, is less than 1 wt% at a pressure of 100 atm, which will limit the MOFs' applications.

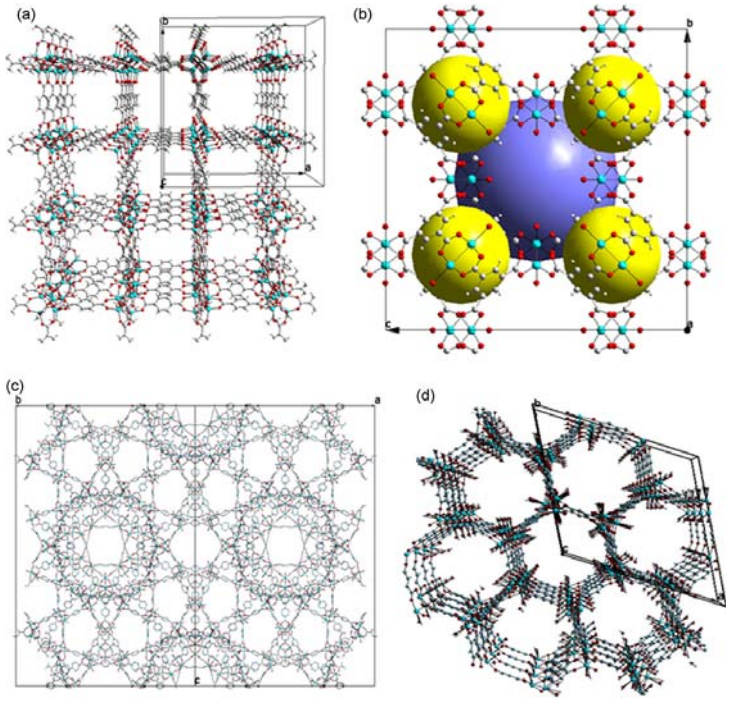

Fig. 2.11. Crystal structure of metal organic frameworks: (a) MOF-5; (b) HKUST-1 (cavities, yellow and blue balls); (c) MIL-101, and (d) MOF-74 or CPO-27-Co(Ni) (metals, cyan; oxygen, red; carbon, grey) [53].

2.5.4 Graphite Nanofibers (GNFs)

GNFs consist of graphite platelets arranged in different directions. This structure presents a large number of edges, which consecutively constitute available sites for chemical or physical interaction, mainly for physisorption. Carbon nanofibers run from 5 to 100 microns in length and 5 to 100 nm in diameter. A schematic diagram of a catalytically grown carbon nanofiber is shown in Figure 2.12 .

There is a huge difference between the results for hydrogen storage capacities of pure GNFs from 67 wt% [60], which nobody has confirmed yet, to 0.04 wt% [61]. Gupta et

al. [62] synthesized GNFs through thermal decomposition of acetylene which was carried out utilizing Pd sheets as the catalyst. The reversible hydrogen storage capacity of their samples was ~17 wt% at RT and 80 atm.

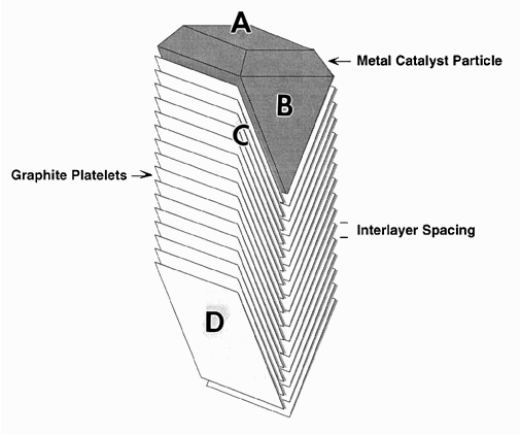

Fig. 2.12. Schematic diagram of a catalytically grown carbon nanofibers [60].

Recently, Kim et al. [63] investigated Pt-doped GNFs with a platinum content range of 1.3-7.5 wt%. They reported that hydrogen stored in the samples increased by raising the amount of Pt to reach to a maximum of 3.4 wt% at 298 K and 10 MPa.

In summary, the combined drawbacks of materials which adsorb hydrogen make them less attractive for vehicular applications, but they are acceptable alternatives to liquid hydrogen storage for stationary supplies.

2.6. Hydrogen storage by chemisorption

Chemically bound hydrides are classified into two main groups: 1) complex hydrides, such as alanates and borohydides, which are usually non-reversible, and 2) metal hydrides, such as intermetallic compounds and magnesium hydride. Figure 2.13 shows

the general hydrogen absorption process in metals. The dehydrogenation of all of these groups can be obtained by either increasing the temperature or reducing the pressure.

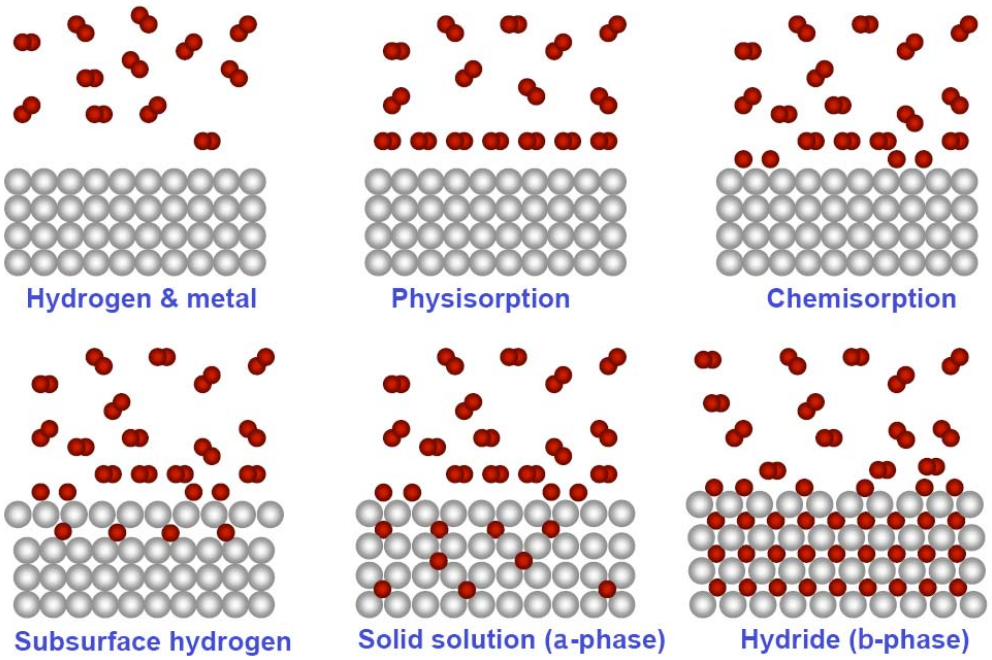

Fig 2.13 Hydrogen absorption process in metals [21].

2.6.1 Complex hydrides

The general formula for complex hydrides is $A_xM_yH_z$, in which A is an alkali, an alkaline earth, or a transition metal. If M is aluminium, they are called “alanates”, and if it is boron they are called “borohydrides”. Their structure is a mix of ionic and covalent hydrides. As shown in Table 2.7 [64, 65], the gravimetric hydrogen capacity of these materials is very high, and it seems they could be viable candidates for on-board hydrogen storage; however, their poor kinetics and irreversible hydriding reactions restrict their practical applications. In the last few years, many investigations have been conducted on complex hydrides to improve their hydrogen storage properties.

Table 2.7. Hydrogen storage capacity of some complex hydrides [64, 65].

Chemical formula	Hydrogen (wt %)
$NaAlH_4$	7.4
$LiAlH_4$	10.5
$Mg(AlH_4)_2$	9.3
$Ca(AlH_4)_2$	7.7
$LiBH_4$	18.4
$NaBH_4$	10.6
$Mg(BH_4)_2$	14.8
$Ca(BH_4)_2$	11.4

2.6.1.1 Sodium Aluminium Hydride

Sodium aluminium hydride ($NaAlH_4$) is a low cost material with 7.4 wt% hydrogen storage capacity, but poor absorption/desorption kinetics and irreversibility.

$NaAlH_4$ releases hydrogen through three steps [66]:

$$3NaAlH_4 \rightarrow Na_3AlH_6 + 2Al + 3H_2 \quad (2.1)$$

$$Na_3AlH_6 \rightarrow 3NaH + Al + 3/2H_2$$

$$NaH \rightarrow Na + 1/2H_2$$

that hydrogen released in the first two reactions which occur at 210 °C and 250 °C, respectively, which are compatible with the temperature for on-board applications, amounts to 5.6 wt%, and this is the storage capacity considered for this material because the third step occur at very high temperature.

In 1997, Bogdanovic and Schwickardi [67] reported that doping with Ti can significantly improve the reversibility and desorption kinetics. Since then, many studies have been developed on doped $NaAlH_4$, with such dopants as TiN [68], TiF_3, and $ZrCl_3$ [69]. An understanding of soak and release reactions by sodium aluminium hydride and of the effects of catalysts on the reactions could lead the way to vehicle applications. Recently, anelastic spectroscopy has given essential information on the different decomposition steps and effects of catalysts [70-73], however, despite all efforts, the mechanisms are unknown so far.

2.6.1.2 Lithium Aluminium Hydride

Despite the high storage capacity of lithium aluminium hydride, its thermodynamic stability and non-reversible hydrogenation limit its on-board applications. Differential scanning calorimetry (DSC) studies by Block and Grey [74] indicated that there is a phase transition at ~180 °C before the first dehydrogenation reaction ($LiAlH_4 \rightarrow Li_3AlH_6$), which occurs at 190-220 °C. The second hydrogen release step happens at 230-280 °C. Total gravimetric capacity by this temperature is 5.6 wt %, and the final desorption occurs at ~700 °C, which is too high for practical applications. Balema et al. found that the first dehydrogenation reaction could happen at RT after mechanical milling of $LiAlH_4$ with $TiCl_4$ [75], and Chen et al. [76]claimed that doping the hydride with 2 mol% of $TiCl_3$ can reduce the temperature of the second step by almost 150 °C. Wang et al. [77]studied a five-step physiochemical pathway for the cyclic dehydrogenation and rehydrogenation of $LiAlH_4$. The $LiAlH_4$ produced by this physiochemical method exhibited excellent dehydrogenation kinetics and released ~4 wt % hydrogen in the range of 80-100 °C. In spite of all these significant achievements, the hydrogen storage properties of this hydride are still far from the target.

2.6.1.3 Magnesium Aluminium Hydride

Fossdal et al. [78] studied the structure of magnesium aluminium hydride $Mg(AlH_4)_2$ by both X-ray and neutron diffraction. They found that the structure is a sheetlike arrangement consisting of $[AlH_4]$- tetrahedra surrounded by six Mg atoms in a distorted MgH_6 octahedral geometry (Figure 2.14).

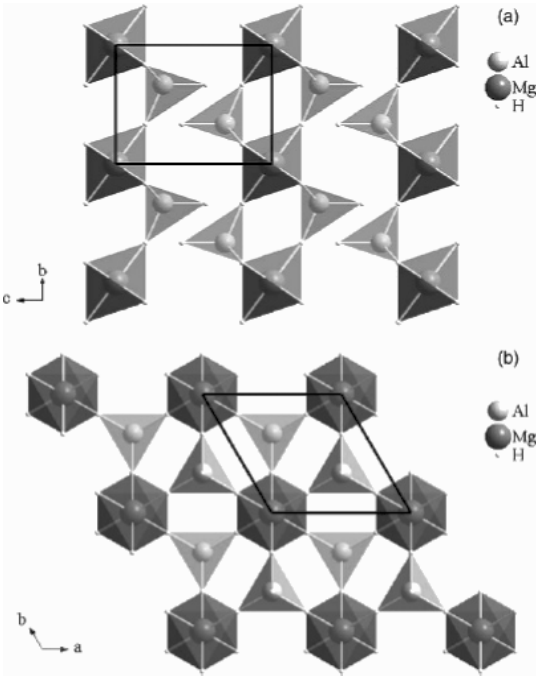

Fig 2.14. Crystal structure of $Mg(AlH_4)_2$ along the *a*-axis (a) and the *c*-axis (b) [78].

The dehydrogenation process of this hydride occurs at 163 °C according to the following equation and without the involvement of $(AlH_6)_3$:

$$Mg(AlH_4)_2 \rightarrow MgH_2 + 2Al + 3H_2 \qquad 2.2$$

the resultant MgH_2 releases hydrogen at ~280 °C, and the remaining Mg reacts with Al to produce Al_3Mg at 400 °C. This process is prohibited thermodynamically [79]. Komiya et al. [80] studied the effects of $TiCl_3$ on the hydride. They found that 1-5 mol% $TiCl_3$ reduces the desorption temperature of the first reaction. A large amount of

hydrogen was released during ball milling of a sample of $Mg(AlH_4)_2$ + 5 mol% $TiCl_3$ at RT. However, a maximum of 0.3 wt% hydrogen was absorbed by a sample of $Mg(AlH_4)_2$ + 1mol% $TiCl_3$ at 330 °C and under 30 atm hydrogen pressure.

2.6.1.4 Calcium Aluminium Hydride

$Ca(AlH_4)_2$ is very similar to $Mg(AlH_4)_2$ but with a theoretical maximum hydrogen capacity of 7.9 wt% and a theoretical reversibility of 5.9 wt%. Mamatha et al. [81] and Komiya et al. [80] synthesized $Ca(AlH_4)_2$ by the following reaction:

$$2NaAlH_4 + CaCl_2 \rightarrow Ca(AlH_4)_2 + 2NaCl \quad (2.3)$$

and the decomposition processes take place in two steps:

$$Ca(AlH_4)_2 \rightarrow CaH_2 + 2Al + 3H_2 \quad (110\text{-}200\ ^\circ C) \quad (2.4a)$$

$$CaH_2 \rightarrow Ca + H \quad (280\ ^\circ C) \quad (2.4b)$$

Showarz et al. [82]presented different methods of synthesis for the tetrahydrofuran (THF) adduct of $Ca(AlH_4)_2THF_x$. Decomposition of the sample, because of the release of coordinated THF and hydrogen, produces CaH_2 and Al.

Neither $Mg(AlH_4)_2$ nor $Ca(AlH_4)_2$ have a potential for further expansion as a solid state material for hydrogen storage because of their poor hydrogen storage properties in comparison with $LiAlH_4$.

2.6.1.5 Sodium Borohydride

Sodium borohydride ($NaBH_4$), which is not a new compound, but was discovered in the 1940s, can be used in many different purposes, for example, as a reducing agent in various organic and inorganic processes [83]. Starting from 2000, it has been considered

as a candidate hydrogen carrier and supplier for fuel cells and hydrogen production systems [84]. $NaBH_4$ can be produced from trimethyl borate and sodium hydride reactants from the so-called Rohme-Hass process:

$$4NaH + B(OCH_3)_3 \rightarrow NaBH_4 + 3NaOCH_3 \quad 2.5$$

in which this reaction is generally performed in an autoclave [85]. Hydrogen can be released via thermal and catalytic dehydrogenation of $NaBH_4$:

$$NaBH_4 + (2+x)H_2O \rightarrow 4H_2 + NaBO_2.xH_2O \quad 2.5$$

to suppress the self-hydrolysis of $NaBH_4$, NaOH should be added to the process. It can be added in different amounts from 5 to15 wt%, however, 3-5 wt% is considered to be sufficient to control hydrogen release [86].

Despite the acceptable hydrogen storage capacity and desorption kinetics of $NaBH_4$, its production and regeneration is too difficult for practical on-board applications. However, Demirici et al. [87]showed that $NaBH_4$ has a potential for portable and/or niche applications.

2.6.1.6 Lithium Borohydride

In 1940, Shlesinger and Brown [88] synthesized lithium borohydride ($LiBH_4$) by reaction of ethyl lithium with diborate (B_6H_6):

$$2LiH + B_2H_6 \rightarrow 2LiBH_4 \quad 2.6$$

The thermal desorption spectrum of the hydride shows four endothermic peaks attributed to i) a polymorphic transformation around 110 °C, ii) melting at 267- 280 °C ,iii) the first dehydrogenation at 490 °C, and iv) the release of three of the four hydrogen atoms at 680 °C [89]. Additives to $LiBH_4$ may reduce the desorption temperature, T_{des}.

For example, T_{des} is reduced by almost 100 °C in the presence of SiO_2 [90]. Vajo et al. [91] showed that addition of $1/2MgH_2$ to $LiBH_4$ yielded a destabilized, reversible hydrogen storage system with a hydrogen capacity of 8-10 wt%. Fan et al. [92] have shown that adding 16 wt% Nb_2O_5 to a composite of MgH_2 + $LiBH_4$ produced a material system with a gravimetric hydrogen capacity of 6-8 wt% below 400 °C, which could be rehydrogenated to 5-6 wt% in 4 h at 400 °C and 1.9 MPa. Recently, Mao et al. [93] prepared a TiF_3-doped $LiAlH_4$-$LiBH_4$ system by ball milling. Their results demonstrated that the onset desorption temperature of the sample with 5 mol% TiF_3 decreased by ~64 °C and the decomposition enthalpy decreased by 14 kJ/ (mol)H_2. This system could absorb 3.76 and 4.78 wt% hydrogen at 600 °C and 4 MPa in 1 h and 14 h, respectively.

Although $LiBH_4$ is a promising candidate for hydrogen storage for on-board applications, its drawbacks, such as irreversibility and high thermodynamic desorption enthalpy, have remained challenges and need more research to improve.

2.6.1.7 Magnesium Borohydride

Magnesium Borohydride, $Mg(BH_4)_2$, has been accepted as a potential candidate hydrogen storage material because of its large hydrogen capacity (14.9 wt%) and smaller enthalpy (22.7 $kJmol^{-1}H_2$) in comparison with $LiBH_4$ [94, 95]. It has been synthesized according to reaction 2.7 [96] and also several other new reactions [97].

$$MgCl_2 + 2NaBH_4 \rightarrow Mg(BH_4)_2 + 2\ NaCl \qquad 2.7$$

while dehydrogenation starts around 300-400 °C and continues in several steps to a maximum of 13 wt% up to 500 °C [96].

Li et al. [96] found that ball milling the hydride with $TiCl_3$ reduced the initial T_{des} significantly. Fichter et al. infiltrated $Mg(BH_4)_2$ into the voids of activated carbon with a pore diameter of < 2 nm and found that the decomposition temperature of $Mg(BH_4)_2$ was reduced [98]. Recently, Yu et al. [99] demonstrated a system of ball-milled $Mg(BH_4)_2/LiNH_2$, in a 1:1 ratio, which improved the dehydrogenation process. Their system released 6.8 wt% hydrogen below 300 ^oC and 4.6 wt% hydrogen from 300-500 $^\circ C$. Very recently, Fang et al. [100]reported that a $LiBH_4/Mg(BH_4)_2$ mixture, formed by mechanical milling and a subsequent heating process, exhibited different thermal dehydrogenation behaviour from any of the constituent materials. The sample showed a lower onset temperature, T_{onset}, and also made it clear that the decomposition reaction involved a different pathway in comparison with $LiBH_4$ and $Mg(BH_4)_2$.

The details of the reaction mechanism and the roles of the additives are not clear yet, and this knowledge is necessary for further improvement of both the desorption and the rehydrogenation properties of $Mg(BH_4)_2$.

2.6.1.8 Calcium Borohydride

$Ca(BH_4)_2$ was synthesized in the 1970s, but its crystal structure was determined in 2006 by Miwa et al. [101], who found that it was orthorhombic with space group Fddd. Nakamori et al. [102] found that if the value of the electronegativity of M increases, the dehydrogenation temperature of $M(BH_4)_n$ decreases. In addition, the theoretical hydrogen capacity of $Ca(BH_4)_2$ is 11.5 wt%. These findings were an indication that $Ca(BH_4)_2$ may have superior hydrogen storage properties to $LiBH_4$. The most likely dehydrogenation reaction based on the Density Functional Theory (DFT) is [103]:

$$Ca(BH_4)_2 \rightarrow 2/3\ CaH_2 + 1/3\ CaB_6 + 10/3\ H_2 \qquad 2.8$$

which is assumed to release 9.6 wt% hydrogen. This desorption is supposed to occur at ~98 °C based on DFT, while experimentally, it happens above 200 °C. On the other hand, *in situ* X-ray diffraction has shown that the desorption route of the hydride is:

$$Ca(BH_4)_2 \rightarrow CaH_2 + 2B + 3H_2 \quad (2.9)$$

in which the theoretically released hydrogen is supposed to be 8.7 wt % [104]. Riktor et al. [105] suggested that an unknown intermediate compound is formed during the dehydrogenation of the hydride. Partial rehydrogenation is reported to continue above 350 °C and 100 atm for two weeks [106].

Up to the present, the desorption kinetics and thermodynamics of $Ca(BH_4)_2$ are not explicitly known, while they are of considerable importance in attempts to find the nature of its hydrogen storage properties.

2.6.1.9 Lithium imide and lithium amide

In 2002, Chen et al. [107] reported a new reversible hydrogen storage system of Li-N-H, which met the gravimetric and volumetric criteria of the DOE target (Table 2.4). In this ternary system, Li forms three hydrogenated compounds: an imide (Li_2NH), an amide ($LiNH_2$), and a nitride hydride (Li_4NH). The imide forms by one of the following reactions:

$$2LiNH_2 \rightarrow Li_2NH + NH_3 \quad (2.10)$$

$$2LiH + NH_3 \rightarrow Li_2NH + 2H_2 \quad (2.11)$$

Titherley [108] prepared the amide by exothermic reaction between lithium metal and ammonia:

$$2Li + 2NH_3 \rightarrow 2LiNH_2 + H_2 \quad (2.12)$$

Therefore, the hydrogenation occurs in the two following steps:

$$Li_3N + 2H_2 \rightarrow Li_2NH + LiH + H_2 \rightarrow LiNH_2 + 2\,LiH \quad (2.13)$$

The hydrogen storage capacity of the system is 11.5 wt%, and the overall heat of the reaction is -161 kJ/mol. However, the second step is reversible below 300 °C, and by reacting the imide with hydrogen up to 7wt%, hydrogen can be stored with a favourable enthalpy ΔH = -45 kJ/mol.

The dehydrogenation process also occurs in two steps:

$$2LiNH_2 \rightarrow Li_2NH + NH_3 \quad (2.14)$$

$$NH_3 + LiH \rightarrow LiNH_2 + H_2 \quad (2.15)$$

in which the first step is the rate limiting step [109].

As with other promising candidates for hydrogen storage, to reduce the desorption temperature of the amide, most of investigations have focused on two main approaches: ball-milling and addition of catalysts. Makmaitree et al. [110] ball milled the amide and reported that T_{onset} was reduced from 120 °C to room temperature. They explained this by mechanical activation via particle size reduction. Ichikawa et al. [109] ball milled a $LiNH_2$/LiH mixture and observed that hydrogen was released over a temperature range of 180-400 °C and also that the amount of released ammonia was reduced significantly. This group then added 1 mol% of Ni, Fe, CO, and $TiCl_3$ to the ball-milled mixture and found that both NH_3 evolution and the desorption temperature were drastically reduced, particularly for the sample including $TiCl_3$, which released 5.5 wt% hydrogen between 150 °C and 250 °C. Isobe et al. [111] confiremed the results of $TiCl_3$ doping and also found that Ti and TiO_2 were effective for reducing the desorption temperature.

Although the imides and amides clearly offer some advantages for reversible and high capacity hydrogen storage, there are fundamental challenges in their practical applications due to their tendency to be hygroscopic and even pyrophoric as a result of their sensitivity to water and air, and also their low desorption kinetics and high desorption temperature.

2.6.2 Metal hydrides

The thermodynamic behaviour as well as the capacity of a metal hydride can be characterised by its Pressure-Composition Isotherm (PCI) . Fig. 2.15 depicts an ideal PCI curve of a typical metal hydride at a constant temperature. In the first step of the curve the hydrogen adsorbed by the metal is increased by increasing the hydrogen pressure, and the metal forms a solid solution with hydrogen called the α-phase. When this phase reaches its maximum hydrogen solubility, the formation of the hydride phase (β-phase) will start [112]. At equilibrium pressure (P_e), the transformation from α-phase to β-phase becomes complete. At this flat plateau pressure, both of the phases co-exist.

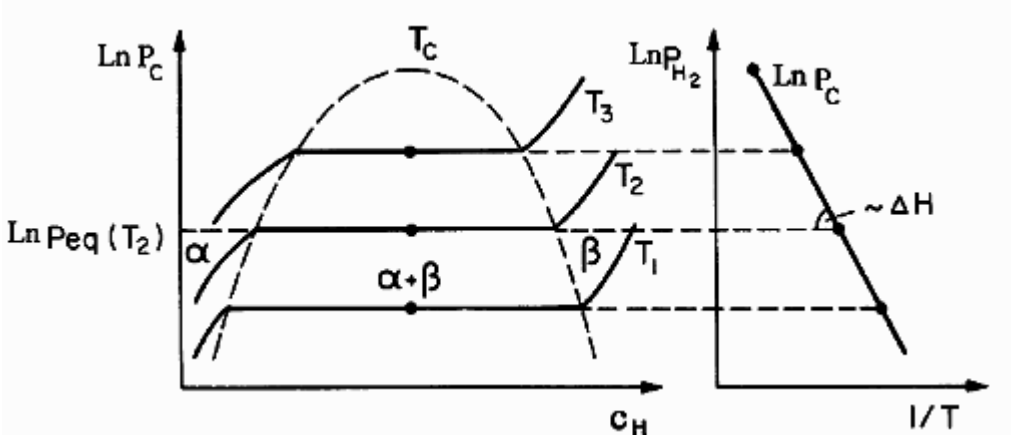

Fig. 2.15. Ideal PCI curve (left-hand side) and the corresponding Van't Hoff plot (right-hand side) for a metal hydride [113].

The plateau pressure will rise with temperature according to the Van‘t Hoff equation [122] and disappear at the critical temperature T_c:

$$LnP_e = \frac{\Delta H}{RT} + \frac{\Delta S}{R} \qquad 2.16$$

in which R is the gas constant, T is the absolute temperature, and ΔS and ΔH are the entropy and enthalpy changes per mole H_2. The enthalpy of hydride formation can be easily determined from the slope of the Van’t Hoff plot.

The reaction kinetics of metal hydriding/dehydriding is an important consideration for practical hydrogen storage applications. It has been shown that the hydrogen *absorption* reaction is composed of several different steps, including: 1) dissociation of hydrogen molecules to hydrogen atoms, 2) surface penetration of hydrogen atoms, 3) diffusion of hydrogen atoms through the hydride layer by a vacancy mechanism (α phase) or interstitially (β phase), 4) nucleation of the α or β phase, and 5) movement of the α/β phase [114, 115]. For hydrogen *desorption*, the steps include: 1) hydride decomposition at the hydride/metal interface, 2) diffusion of hydrogen atoms through α phase, 3) surface penetration of hydrogen atoms, 4) recombination of chemisorbed hydrogen atoms and physisorption, and 5) desorption to the gas phase [115, 116]. If one of the steps, in either hydriding or dehydriding, is very slow compared to the others, it is known as the rate-limiting or rate-determining step. On the other hand, there are some theoretical kinetic equations related to different rate-limiting steps which are summarized in Table 2.6 with descriptions of their corresponding models [117].

Description of the absorption/desorption kinetics is possible by plotting the left side equations in Table 2.6 versus time. The plot giving the best linearity determines the rate limiting step. Equation 2.17 describes the time dependency of the rate constant, *k*:

$$k = A\exp(-\frac{E_a}{RT}) \qquad 2.17$$

where A is a pre-exponential constant, E_a is the activation energy, and R is the gas constant.

Table 2.6. Kinetic equations related to different rate-limiting steps. f = reacted fraction, t = time, k = reaction rate constant, CV = contracting volume model and JMA = Johnson-Mehl- Avrami model.

Kinetic equation	Description
$f = kt$	Surface controlled (chemisorption)
$[-\ln(1-f)]^{1/3} = kt$	JMA 3D: Random bulk nucleation/surface and three-dimensional growth of the existing nuclei
$[-\ln(1-f)]^{1/2} = kt$	JMA 2D two-dimensional growth of existing nuclei
$1-[1-f]^{1/3} = kt$	CV 3D : contracting volume, three-dimensional growth
$1-(1-f)^{1/2} = kt$	CV 2D : contracting volume, two-dimensional growth
$1-(2f/3)-(1-f)^{2/3} = kt$	CV 3D (variable velocity): contracting volume, three-dimensional growth diffusion controlled by decreasing interface velocity

Intermetallic compounds (IMC) consist of two or more metals with a common formula: $A_xB_yH_z$. They are classified as several groups based on the stoichiometric ratios of A and B such as: AB_5, AB, and Ti-based body centred cubic (BCC) compounds.

The main studies on the AB_5 compounds have been done on $LaNi_5$. Although these materials have low hysteresis and ease of activation in the initial cycle, their costs, low hydrogen storage capacity (a maximum of 1.9 wt %) [118], and degradation during

hydriding/dehydriding are their major drawbacks. Many investigations have been conducted on them, mainly by substitution of other metals [119-122] to improve their properties. However, there has been little in the way of a breakthrough in the $LaNi_5$ based hydrogen storage materials so far.

The main studies on the AB compounds have been done on TiFe. The advantages of this compound are inexpensive materials and high volumetric density. However, low hydrogen storage capacity, high sensitivity to oxygen and moisture, and pronounced hysteresis are their disadvantages [123, 124]. Although substitution of both Ti and Fe by other metals, such as Pd, Al, and Ni [125-127] could improve the hydrogen storage properties of these compounds, the results are still too far from the target. Consequently, there have been very few reports on TiFe recently.

Ti-based BCC phase alloys have attracted great attentions recently. They can store hydrogen up to 4 wt% at room temperature [128]. Huang et al. [129] reported a hydrogen storage capacity of 3.2 wt% and a reversible capacity to ~2 wt% for $TiCr_{1.2}(V–Fe)_{0.6}$ at RT . Recently, Mi et al [130] investigated the effect of Al on $Ti_{26.5}Cr_{20}(V_{0.45}Fe_{0.085})_{100-x}Al_xCe_{0.5}$ alloy. They reported that by increasing Al content, the lattice parameter of the BCC phase and, as a result, the hydrogen desorption equilibrium pressure increased, but the capacity decreased. In spite of many studies on BCC alloys, their drawbacks, their low hydrogen storage capacity and the cost of vanadium, could not be solved until the present.

Another important metal hydride is MgH_2, but as the centre of attention of this thesis is on it, its hydrogen storage properties and related background have been described in an independent subchapter.

2.7 Magnesium Hydride

2.7.1 Introduction

Magnesium hydride (MgH_2) has attracted scientists for hydrogen storage applications due to its high energy density of 9 MJ/Kg, a theoretical hydrogen capacity of 7.6 wt%, which could translate into 2200 mAh/g Mg, low cost, and abundance in nature [141]. These characteristics make Mg one of the best candidates for hydrogen storage for vehicular applications. However there are some key drawbacks for its on-board applications such as: extremely poor absorption/desorption kinetics as a result of diffusion path limitations, high hydriding and dehydriding temperature, which is more than 300 °C at 1 atm, and high sensitivity towards moisture and oxygen [131]. Numerous investigations have aimed to improve the hydrogenation properties, which mainly have involved: i) utilizing ball milling and ii) introducing additives. In this section, a brief discussion of the *history*, *structure,* and *properties* of magnesium hydride will be presented, after that its *absorption/desorption thermodynamics,* and finally *methods to combat the drawbacks* will be explained in detail.

2.7.2 History

MgH_2 was produced first in 1912 when pyrolysis of ethylmagnesium halides yielded a small amount of magnesium hydride mixed with ethylene and magnesium halide [132]:

$2MgXC_2H_2 \rightarrow MgH_2 + MgX_2 + 2C_2H_4$ 2.18

and in 1951, pure MgH_2 was synthesized by pyrolysis of diethylmagnesium at 400 K in vacuum:

$Mg(C_2H_5)_2 \rightarrow MgH_2 + 2C_2H_4$ 2.19

finally, reacting Mg with hydrogen at 200 bar and 850 K in pthe resence of MgI_2 as catalyst, produces MgH_2 in a larger amount [133]:

$Mg + H_2 \rightarrow MgH_2$ 2.20

More recently, lower temperature production from Mg and H_2 using ball milling of nanocrystalline Mg has been investigated [134]. Developing milling methods to economically produce large quantities of metal hydrides, including magnesium hydride, is an important challenge.

2.7.3 Structure and Properties

Magnesium is a silver alkaline earth metal with atomic number 12, atomic mass 24.305 au, and oxidation number +2. It is the eighth most abundant element in the Earth's crust by mass [135]. Mg is readily ignitable and can be ignited spontaneously in the presence of water. Its ignition temperature in dry air is 918 °C, which decreases with increasing moisture content. Since it is highly reactive, the free metal is not found naturally. Fournier et al. [136] reported that oxidation of Mg at RT and 150 °C for 15 min results in an oxide layer of less than 2 nm. The crystal structure of magnesium is hexagonal with a = 0.321nm nd c = 0.521 nm, space group P63/mmc, and a density of 1.74 g/cm^3.

The uptake of hydrogen in Mg starts with adsorption and dissociation of hydrogen molecules on the magnesium surface and continues to diffusion and hydride formation.

During this process the hydrogen atoms initially occupy tetrahedral interstitial sites to form a solid solution of hydrogen in magnesium, called α-phase [137]. Furthermore, on addition of H-atoms, the β-phase will appear, which has a body-centred tetragonal lattice of rutile type with lattice parameters a = 0.452 nm and c = 0.302 nm, density 1.42 g/cm^3, and space group $P4_2/mnm$ (Fig 2.16) [133]. X-ray diffraction showed two Mg atoms at (000) and (1/2,1/2,1/2) and four H-atoms at ±(x, x, 0) and (x+1/2, 1/2 +x, 1/2) with x = 0.306 [138].

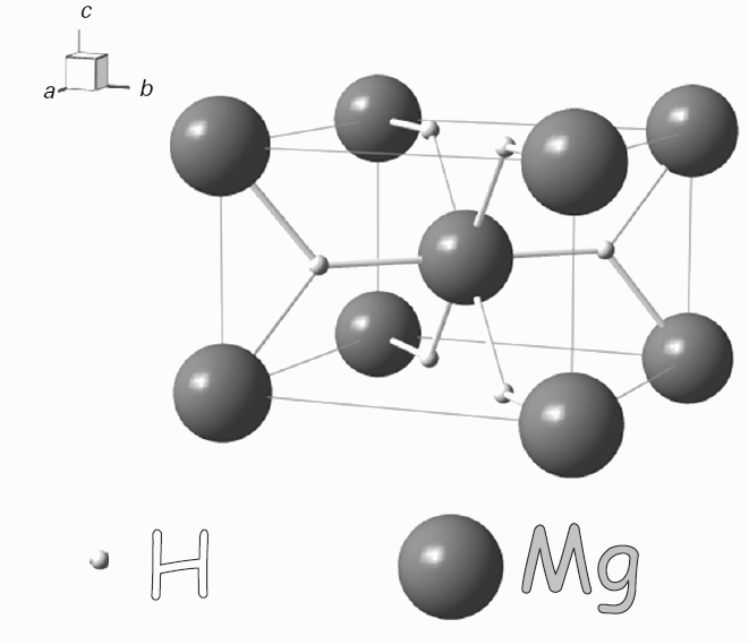

Fig. 2.16. Crystal structure of β-MgH_2[133] .

The β-MgH_2 transforms to metastable γ-MgH_2 under 7-8 GPa stress, which could occur during ball milling [137]. The structure of γ-phase is orthorhombic with lattice parameters a = 0.453 nm, b = 0.544 nm, and c = 0.493 nm, and space group Pbcn [112].

The desorption temperature of MgH_2 is more than 300 °C at a pressure of 1 atm, which is too high for practical applications.

2.7.4 Thermodynamics

MgH_2 can be formed by the exothermic reaction shown in the equation 2.20. The enthalpy (ΔH_f) and entropy (ΔS_f) of formation are about -74.5 kJ/(mol) H_2 and -135 J/(Kmol) H_2, respectively [139, 140]. Although the magnitude of the enthalpy of MgH_2 is lower than for other alkaline earth metals, it is still very high compared with the target (Table 2.4). Therefore, a range of enthalpy between 10 and 60 $kJmol^{-1}H_2$ is desirable [141], in contrast with physisorption, which is below -10 $kJmol^{-1}H_2$, and chemisorption which is higher than 60 $kJmol^{-1}H_2$.

In addition to the high heat of formation of MgH_2, its poor absorption/desorption kinetics is another drawback which is a result of the absorption mechanism. As mentioned in Section 2.6.2, the absorption starts with hydride formation at the Mg surface, in which its rate of formation is controlled by the density of nucleation sites. Then, the reaction naturally stops, because formation of a hydride layer has covered the surface and prevented the penetration and diffusion of hydrogen to the core of the Mg particles, resulting in slow kinetics [115, 141]. In the first step of the desorption process, α-phase forms at the surface of a particle, and the process continues with the formation and growth of Mg nuclei. In the final step, Mg phase is formed by a volume contraction in the particles, which supports the release of hydrogen through the Mg layers [142]. These absorption/ desorption mechanisms lead to a sluggish kinetics, even at high temperature. Many methods have been investigated by researchers to improve both thermodynamics and kinetics problems of MgH_2, which generally involve ball milling and utilising additives.

2.7.5 Ball milling

Ball milling is the most common method for improvement of the hydrogen storage properties of MgH_2. This technique is a powder processing in which powder mixtures are placed in a ball-mill vial and deformed by collision of balls. Superior samples can be achieved by altering milling parameters, such as milling mode, time, and speed, and the ball-to-powder weight ratio .

There are several types of ball milling processes, such as mechanical alloying (MA), mechanical milling (MM), reactive mechanical alloying (RMA), reactive mechano-chemical synthesis (MCS), and mechano-chemical activation synthesis (MCAS) ,which differ in their milling atmospheres and starting materials [143, 144].

Regardless of which of these types is used, ball milling has various effects on hydrogen sorption properties such as by decreasing the particle size and agglomeration of particles, increasing the surface area, introducing defects, increasing nucleation sites, and reducing the diffusion path lengths for hydrogen penetration and release. These effects could enhance the absorption/desorption time as well as the desorption temperature of MgH_2 significantly. For example Huot et al. [145] showed that ball-milled MgH_2 could fully absorb at 300 °C and desorb at 350 °C with kinetics 5 times faster than for the unmilled sample. Varine et al. [146] found a near linear reduction of the desorption onset temperature (T_{onset}) from 370 °C to 330 °C.

Although ball milling has the above-mentioned positive effects, the exact effect on hydriding/dehydriding mechanisms is not clear yet. For instant, Selvam et al. [147] believed that the rate determining step (see 2.6.2) in hydrogen desorption of MgH_2 is

the diffusion of H-atoms through the Mg grains formed on the surface of the sample. Whereas, Barkhordarian et al. [148]found that it is the recombination of H_2-molecules on the surface of the sample. In both cases, ball milling could improve the rate of dehydrogenation by reducing diffusion pathway lengths or by increasing the surface area.

Furthermore, ball-milled MgH_2 showed a phase transformation from β-phase to γ-phase (see 2.7.3) as a result of compressive stress. For example, in the Huot et al. [145] results on 2 h ball milling of MgH_2 showed that the sample contained 18% γ-MgH_2. This partially transformed γ-phase usually changes to β-MgH_2 in the first cycle. The main disadvantage of ball milling is the formation of MgO on the surface of magnesium due to oxygen contamination and pick-up in the mill [136].

2.7.6 Additives

Additives may improve hydrogen storage properties by hydrogen dissociation on their surfaces, increased defects and surface area, and/or removal of the required activation step. A combination of ball milling and a catalyst could result in a considerable improvement in both hydrogen cycling kinetics and reduction of the operating temperature.

2.7.6.1 Transition Metals

Various types of transition metals are used as catalysts for MgH_2, such as: vanadium [149-151], titanium [149, 152], nickel [153-155], niobium [156, 157], and palladium [131, 158]. Liang et al. [151] reported that ball milling MgH_2 + 5 at% V released

hydrogen completely in ~3 min at 300 °C, while pure MgH_2 released only 2 wt% hydrogen in ~30 min. The sample absorbed 2 wt% hydrogen at RT in 17 min. Dehouche et al. [150] proposed that vanadium acts as a catalyst for dissociation of H_2 molecules to H-atoms, and also exhibits high hydrogen density and diffusivity due to the small lattice parameters of vanadium. Charbonnier et al. [149] showed that MgH_2 that was ball milled for 100 h with 5 at% V absorbs 4.5 wt% hydrogen at 250 °C and 10 atm. Ti has similar effects to V. It was reported that MgH_2 ball milled with 9 wt % Ti shows complete hydrogen desorption at 300 °C [152]. Lu et al. [159] compared ball-milled MgH_2 + 5 at% Ti and pure MgH_2. Their results showed that the sample with titanium released its total absorbed hydrogen in ~8 min, which is 6 times faster than the pure sample.

Pd is another catalyst for hydrogen sorption of MgH_2. Zaluska et al. [131] added 1 wt% Pd nanopowder to MgH_2 in a shaker-style ball mill. Their results indicated that the Pd was dispersed on the MgH_2 surface. The doped sample soaked up 6 wt% hydrogen in ~ 40 min compared with 120 min for the pure sample. Another important effect of Pd was on Mg surface oxidation, and it eliminated the need for an activation step. The cost of V and Pd inhibits their broad practical applications.

Ball milling magnesium with Ni significantly improves the hydriding/dehydriding kinetics. This is because of the strong affinity of H_2-molecules for nickel, where they dissociates readily to H-atoms and adsorb onto the surface layer of nickel particles [160, 161]. Holtz and Imam [154] studied the addition of 1 at% Ni to MgH_2 and showed a 50% increase in hydrogen capacity, a decrease of 100 ºC in T_{onset} of hydriding and of 75

ºC in T_{onset} of dehydriding. Jensen et al. [162] found that MgH_2 + 2 wt% had an activation energy of 250 KJ/mol, which is 50 Kj/mol less than for their pure sample.

In summary, transition metals dissociate H_2-molecules to H-atoms, which enable them to diffuse along grain boundaries between Mg and catalysts. Therefore, the interface between Mg and the catalyst acts an active nucleation site for the hydride phase [163].

2.7.6.2 Metal oxides

Metal oxides are promising catalytic additives to MgH_2. They have both catalytic effects and act as a milling aid by creating defects in the MgH_2 structure. Because of decreasing hydrogen capacity due to adding metal oxides, most investigations have focused on small additions. Oelerich et al. [164] ball milled 0.05 wt% of V_2O_5 with MgH_2 for 120 h and found noticeable improvement in the absorption and desorption kinetics at 300 ºC. V_2O_5 was doped into MgH_2 by Jung et al. [165] as well. Their sample released 2-3 wt% H_2 at 250 ºC and 6 wt% at 300 ºC and under vacuum, within 120-360 s. The addition of Cr_2O_3 to MgH_2 was studied by several groups [165-167]. Bobet et al. [166] showed a desorption of more than 50% of the stored hydrogen in 30 min at 300 ºC. Dehouche et al. [150] fabricated a sample of MgH_2 + 0.2 mol% Cr_2O_3 and demonstrated that the desorption rate decreased by a factor of four after 1000 cycles at 300 ºC. Some studies has been made on the hydrogen storage properties of MgH_2 + Fe_2O_3 or Fe_3O_4 [168, 169]. Huang et al. [169] ball milled Mg with Fe_2O_3 (and Fe_3O_4) in hydrogen atmosphere with an atomic ratio of 20:1. The sample including Fe_2O_3 released 6 wt% hydrogen, and 5 wt% was released for the Fe_3O_4 doped sample, with T_{onset} = 300 °C. Both samples showed a rehydrogenation of 4 wt% and 4.4 wt%, respectively.

Nb_2O_5 is the most effective metal oxide additive investigated by several groups [170-173]. Barkhordarian et al. [170] reported 6.6 wt% hydrogen desorption at 250 ºC within 10 min. Complete desorption from the 100 h ball-milled MgH_2 + 4 wt% Nb_2O_5 composite occurred within 1.5 min at 300 °C. Milling for 20 h and 2 h increased the desorption time by a factor of 2 and 10, respectively. Aguey-Zinsou later [173] found that the desorption kinetics of 700 h ball-milled pure magnesium hydride is the same as 200 h ball-milled MgH_2 + 17 wt% Nb_2O_5. The lowest T_{des} reported so far is 163 °C for 20 h ball-milled MgH_2 + 1 mol% Nb_2O_5, which released 5 wt% hydrogen in 100 min [174].

The mechanism of the catalytic effects of metal oxides, the same as for other catalysts, is still unclear. Oelerich [168] proposed that the high defect density introduced on the metal oxide particles because of high energy ball milling was responsible. Friedrichs et al. [171] showed a reduction in the Nb particles after recycling, and a phase of $MgNb_2O_{3.67}$ was observed in their X-ray diffraction patterns. Based on these results, they proposed a reaction mechanism involving a lower oxidation state of Nb_2O_5 particles that introduce a network of pathways for hydrogen diffusion through the MgH_2 layers.

2.7.6.3 Intermetallics

Hu et al. [175, 176] used $TiMn_{1.5}$ and $Ti_{37.5}V_{25}Cr_{37.5}$ as additives for MgH_2 and found that the desorption temperature was in the range of 250-270 °C. Liang et al. [177] observed that ball-milled Mg + 30 wt% $LaNi_5$ transformed to MgH_2 + LaH_3 + Mg_2NiH_4 after hydrogenation. Therefore, they concluded that $LANi_5$ is not a direct catalyst for MgH_2 hydrogenation. A reactive mechanical milling (RMM)of MgH_2 + Mg_2Ni and MgH_2 + $Mg_2Ni_{1-x}M_x$ (M = Fe, Co) desorbed 5-6 wt% hydrogen at 300 °C and 0.1 atm

within 50-105 min [178]. Li et al. [179] ball milled Mg mixed with 20 wt% Y-Ni in 30 atm hydrogen pressure and found ~4 wt% absorption at RT in 40 min, 4.5 wt% at 100 °C in 100 s and 5.5 wt% at 200 °C within 200 s. Unfortunately, their composite did not release hydrogen below 300 °C, and at this temperature it desorbed ~5 wt% after 30 min. Vijay et al [180] synthesized MgH_2 + 40 wt% FeTiMn composite by mechanical milling. The sample absorbed 4 wt% and 3.8 wt% hydrogen at 80 °C and 300 °C, respectively, after 13 min. and under 3 atm hydrogen pressure. The main disadvantage of the composite was the large amount of additive required. Gu et al. [181] prepared Mg + 30 wt% $TiV_{1.1}Mn_{9.9}$ by reactive ball milling in hydrogen atmosphere for 20 h at 200 rpm. The sample absorbed 4.46 wt % hydrogen at 330 °C and 30 atm within 60 min, and 1.77 wt% in the same period and pressure at ~100 °C, with very good reversibility.

Recently Yu et al. [182] synthesized highly activated magnesium hydride by a 5 h ball milling of Mg with $Ti_{0.4}Cr_{015}Mn_{0.15}V_{30}$, (BCC), under 30 atm hydrogen pressure. The sample released 6.15 wt% hydrogen at 250 °C in 100 min and soaked up 5.66 wt% H_2 at 80 °C within 150 min. Based on the scanning electron microscope (SEM) results, they concluded that the diffusion of H-atoms in the bulk Mg increases as a consequence of embedding the nanosized BCC alloy in the magnesium aggregates.

2.7.6.4 Graphite and Carbon Nanotubes

In 1999, Imamura et al. [183] ball milled Mg with graphite and benzene additives for 20 h. Their sample started absorption at 180 °C. After that, a number of researchers investigated hydrogen absorption/desorption of Mg + graphite nanocomposites [184-186], but the kinetics were almost the same as those obtained with other additives. Huang et al. [187] fabricated a MgH_2-graphite composite by mechanically milling in

hydrogen atmosphere, using a low energy Uni Ball Mill 5. They reported that the rehydrogenation temperature of their sample was 35 °C lower than that of their as-prepared sample. In addition, their composite had noticeable desorption kinetics.

CNT was added to Mg/MgH_2 powder by reactive milling [188], and by being first mixed and then milled [189][209, 210]. The reactively milled powder absorbed 3.6 wt% hydrogen at 200 °C in 30 min. Wu et al. [189] ball milled a mixture of MgH_2 + SWCNT and reported almost 5 wt% absorption at 300 °C in 1 h and 6 wt% at 350 °C within 5 min, which did not represent any significant development in the sorption properties of MgH_2. Bouaricha et al. [190] found a significant effect on the activation of ball-milled samples by addition of graphene. The adsorbed graphene layer on Mg surfaces formed highly active carbon particles during ball milling, which removed the oxide layer from the surface, and by this addition, there was no need for any extra activation process.

Despite huge investigations into the effects of different types of carbon on the hydrogen storage properties of magnesium and magnesium hydride, there is no compelling evidence that they can act as powerful catalysts to improve MgH_2 sorption properties.

In summary, MgH_2 is still one of the most promising candidates for hydrogen storage purposes; however, in spite of the described background of investigations, its drawbacks restrict it from practical applications. Therefore, in this thesis, in proceeding from other reports, the main focus is on firstly, improvement of surface area and increasing defects by ball milling and also by addition of a hard material, such as SiC, and secondly, doping with catalysts to play different catalytic roles, such as hydrogen molecule dissociation and hydrogen pumping into interior layers of Mg.

Chapter 3

Experimental methods and materials

3.1 Materials

All the materials used are listed in Table 3.1 with relevant information.

Table 3.1. Description of materials used.

Name	Molecular formula	Purity	Particle Size	Manufacturer
Magnesium	Mg	≥99 %	44 μm	Sigma-Aldrich
Magnesium Hydride	MgH_2	99.7 %	50 μm	Sigma-Aldrich
Silicon Carbide	SiC	99.9%	<10 nm	Academy of Science, China
Nickel	Ni	99.9%	1 mm	Sigma-Aldrich
Titanium	Ti	99.9%	5-9 mm	Sigma-Aldrich
Vanadium	V	99.7%	0.5 mm	Sigma-Aldrich
Manganese	Mn	99 %	1.5 mm	Sigma-Aldrich
Chromium	Cr	99.5%	2 mm	Sigma-Aldrich
Carbon nanotubes (multiwalled)	MWCNT	>95%	Outer diameter 20-30 nm, length 0.5 μm	Sigma-Aldrich
Argon	Ar	>99.5	N/A	BOC
Hydrogen	H_2	>99.99%	N/A	BOC
Helium	He	>99.99 %	N/A	BOC

3.2 Materials synthesis

3.2.1 Uni-Ball-Mill 5

In the Uni-Ball-Mill 5, the motion of the balls is controlled by the external magnets [191]. As shown in Fig. 3.1, the ferritic steel balls in the vial are attracted to the inside surface of the jar by strong Nd-Fe-B permanent magnets placed outside the vial. Therefore, this kind of ball milling allows the operator to control the milling energy by adjusting the magnet position.

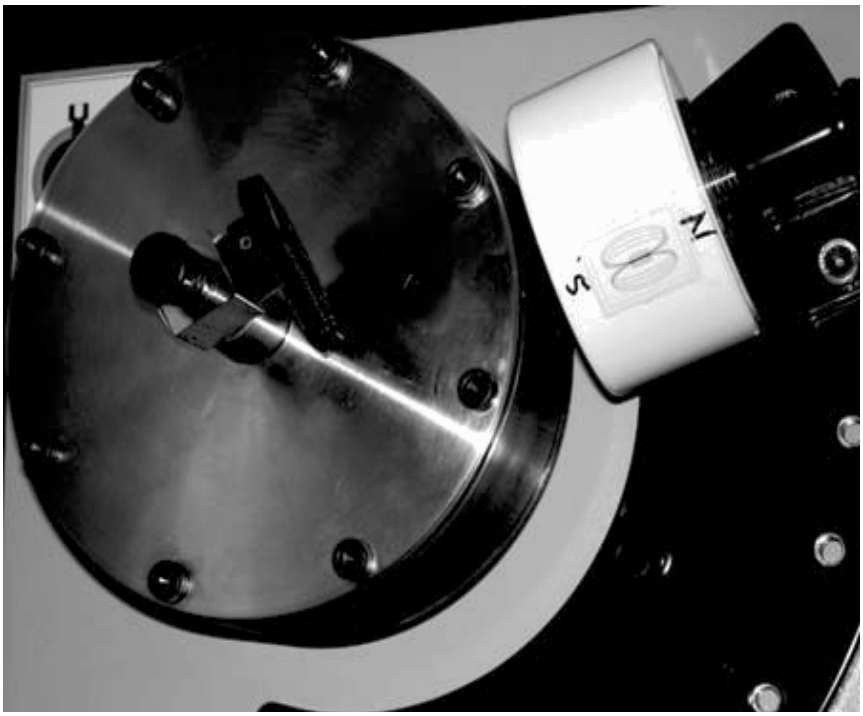

Fig 3.1. Milling vial and magnet mounted in Uni-Bball-Mill for the mechanical strong impact mode.

By changing the magnet positions, four milling modes are available: low energy shearing, high energy shearing, low energy impact, and strong impact modes (Fig 3.2). Also, there are other advantages of this instrument, such as less contamination from the

balls and the vial because of low rpm and the presence of valves on the jar for filling with inert gases such as hydrogen. There are various parameters of the Uni-Ball-Mill which affect the ball-milling process of a composite, and they have to be fixed before starting an experiment. They include number of balls, milling speed, milling time, vial atmosphere, ball-to-powder weight ratio (B/P), and the distance between the magnet and the jar (working distance). The magnet-jar distance is fixed in our laboratory and is 2 mm.

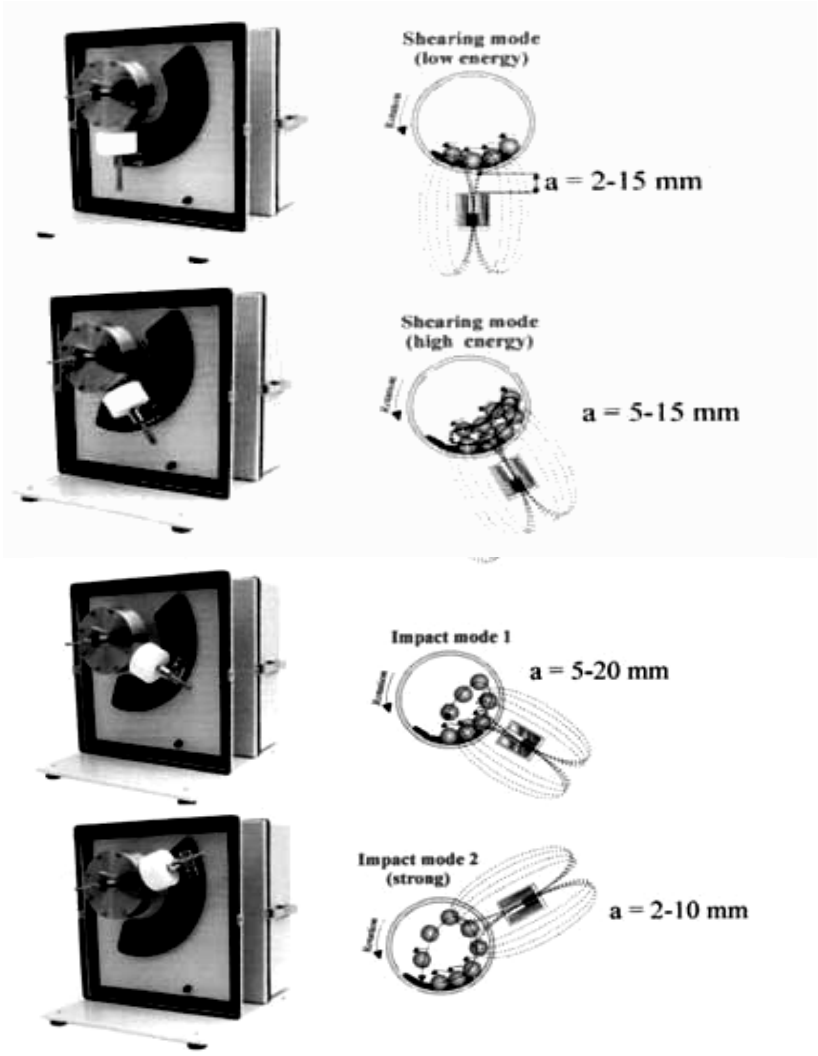

Fig. 3.2. Motion of balls in the magnetic ball mill [191].

MgH_2-SiC (Chapter 4), MgH_2-SiC-Ni (Chapter 5), and MgH_2-BCC (Chapter 6) have all been synthesized by this ball-milling instrument.

3.2.2 QM-3SP2

QM-3SP2 is a planetary ball mill in which rotating jars are installed on a revolving disk (Fig. 3.3(a)). This kind of ball mill potentially can impart high energy to the powder [192]. The motion of the shell and balls is shown in the schematic diagram in Fig. 3.3(b). When the turn-plate rotates, the tank axis makes planetary movements, and the balls in the tanks grind and mix samples at high speed.

QM-3SP2 is the requisite instrument for mixing, fine grinding, and small sample production. Its features are:

- Gear-drive guarantees high uniformity and repeatability of experiments;
- Fast rotational speed, high efficiency and fine granularity;
- Four samples with different sizes and materials in one experiment available;
- Continual speed regulation;
- Ideal rotary speed selection according to experimental results;
- Timed powering-off, positive and negative revolution if required;
- Features low centre of gravity, good rigidity, compact structure, safety, reliable operation, low noise, no pollution, and low wear.

All samples in Chapter 7 (Mg-BCC-CNT), and the Mg+10wt%Ni (ball-milled) and Mg-Ni (ball-milled-cast) samples (Chapter 8) were fabricated using this ball-milling instrument.

(a)

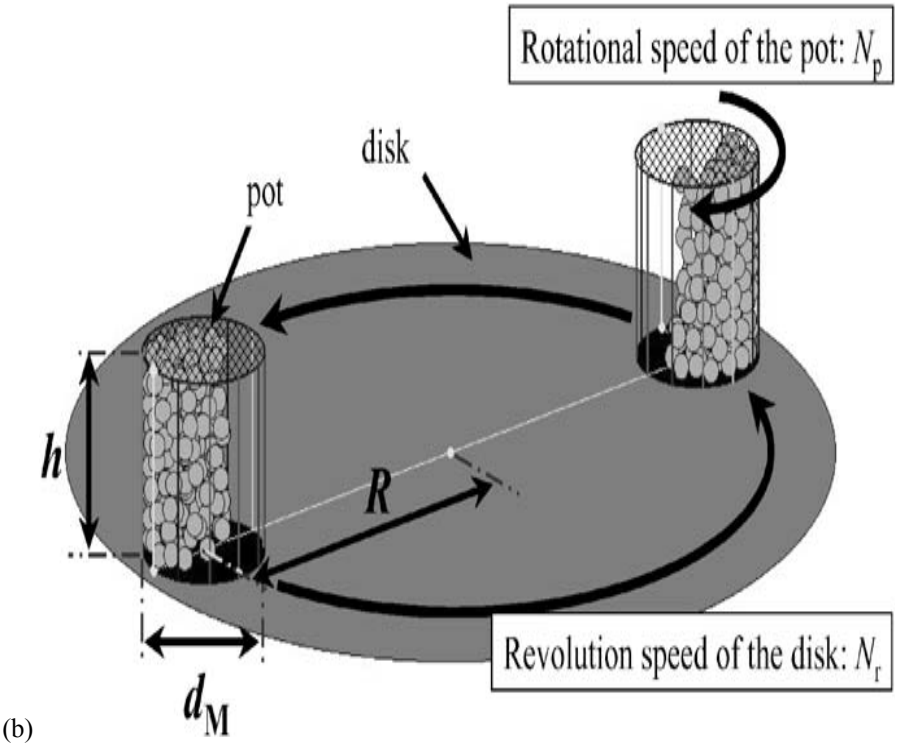

(b)

Fig 3.3. a) QM-3SP2 planetary ball mill. b) A schematic diagram of the planetary ball mill [192].

3.3 Physical analysis

3.3.1 X-Ray diffraction

X-ray diffraction (XRD) patterns for MgH_2-SiC (Chapter 4) and MgH_2-SiC-Ni (Chapter 5) samples were obtained using a Philips PW 1730 generator and diffractometer with Cu K_α radiation (λ = 0.15418 nm) and operated at 40 kV and 30 mA. This equipment is useful for a range of powder, crystal, and thin film samples. The XRD patterns of the MgH_2-BCC (Chapter 6), MgH_2-BCC-CNT (Chapter 7), and the Mg+10wt%Ni (ball-milled) and Mg-Ni (ball-milled-cast) samples (Chapter 8) were obtained by the GBC-MMA X-Ray Diffractometer . It is a versatile compact diffractometer capable of an extended range of materials analysis functions, including θ-θ mode. It also maintains a horizontal sample stage, has a new advanced microprocessor controller, and has new sample stages for large, heavy, and bulky samples.

3.3.2 Transmission Electron Microscopy

Transmission Electron Microscopy (TEM) enables researchers to study a specimen's structure in detail, even details as small as a single column of atoms. The sizes, shapes, and arrangement of the particles which make up a composite, as well as the elements and compounds in the sample, and their relative ratios in areas of a few nanometers can all be observed by TEM. The TEM installed in our laboratory is a JEOL 2011 that uses a 200 kV LaB_6 filament, is equipped with 2 cameras, and is capable of both conventional and cryo-TEM. Its operation software is jeol Fas Tem and Gatan Digital Micrograph. The TEM analysis of MgH_2-SiC (Chapter 4) is based on this instrument.

3.3.3 Scanning Electron Microscopy

The scanning electron microscope (SEM) used for all samples was a JEOL JSM-6460A . It is a low vacuum capable SEM with a conventional tungsten filament electron source, which is well equipped for imaging as well as microanalysis. In addition, it is capable of collecting secondary electron images at the acceleration voltage of 30 kV with a maximum resolution of 3 nm. The filament supplies a high beam current capacity for backscattered electron images and X-ray mapping. It also is equipped with a quantitative energy dispersive spectrometer (EDS) for chemical analysis. Analysis Station software controls the operation and allows users to capture images and analyse data by EDS and X-ray maps on the SEM.

3.3.4 BET

Surface area is an important characteristic which can affect the quality and utility of materials, and the best method to measure it is the Brunauer-Emmett- Teller (BET) method. Therefore, the surface area of the first series of samples (MgH_2-SiC) was measured by BET using a Quanta-Chrome Nova 1000 instrument.

3.4 Hydrogen sorption properties

3.4.1 Differential Scanning Calorimeter

The most commonly used thermal analysis technique is differential scanning calorimetry (DSC). It measures the alteration in the enthalpy of a composite due to changes in its physical and chemical properties, such as melting, oxidation, hydrogen desorption, and other heat-related changes, as a function of temperature or time and

provides quantitative and qualitative data during phase transitions. Two DSC instruments have been used for thermal analysis of our samples.

3.4.1.1 DSC Q100

With this system (Fig. 3.4), reversible and non-reversible thermal changes can be identified, and exact determination of the heat capacity of a sample can be monitored. Its temperature range is -90 °C to 500 °C, the required sample weight is 5-20 mg in an aluminium crucible with a pressed lid, and the purge gas is 50 mL/min nitrogen. The desorption temperatures (T_{des}) for MgH_2-SiC, MgH_2-SiC-Ni, and MgH_2-BCC were measured by this instrument.

Fig 3.4. DSC Q100.

3.4.1.2 Mettler Toledo DSC1

The other DSC apparatus was a Mettler Toledo DSC1 (Fig. 3.5), with a temperature range from -70 °C to 1200 °C, sample required weight of 5-20 mg in an aluminium crucible, and gas flow

between 0 and 200 mL/min, with capability to switch up to 4 gases such as: air, argon, nitrogen, and oxygen. All samples were loaded into the crucible in a glove box and transferred in an argon filled bottle to the DSC apparatus to prevent sample oxidation. The T_{des} of the Mg-BCC-CNT, Mg+10wt%Ni (ball-milled), and Mg-Ni (ball-milled-cast) samples were measured using this facility.

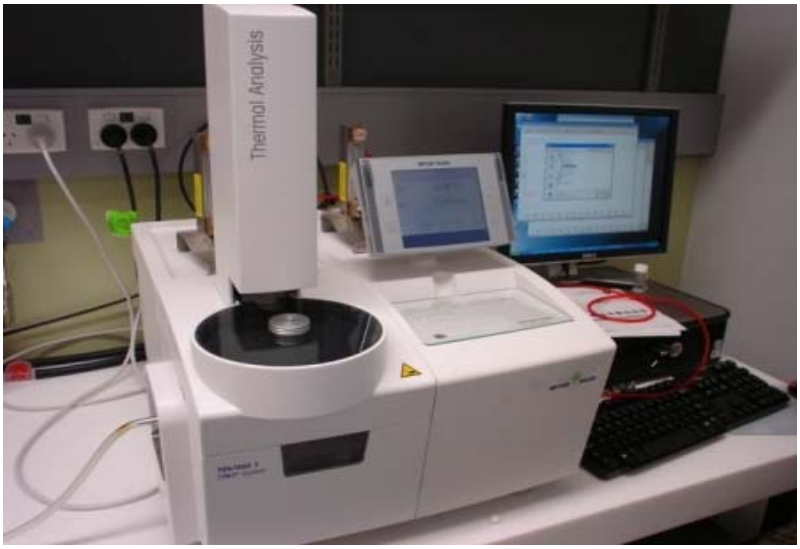

Fig 3.5. Mettler Toledo DSC1 apparatus.

3.4.2 Hydrogen Content

The hydrogen sorption properties of all of the samples were studied by Sievert's method [193] using an Advanced Materials Corporation (AMC) Gas Reaction Controller (GRC) instrument (Fig 3.6) which performs a quantitative analysis of the gas-solid reaction.

All of the samples were placed in channel 1 (ch1hld) in a sample holder with dimensions of 9.3 mm dia. × 25 mm × 1.7 cm and a temperature range of RT to 500 °C and 20-30 atm hydrogen pressure. The connected computer is operated by the software control program, GrcLV, which performs fully automatic operation.

To calculate the accurate amount of absorbed/desorbed hydrogen, N_0 mol of hydrogen is first removed from the reservoir of the GRC (V1 in the Figure), and then the desired amount is transferred to the reaction chamber where the sample is held (Ch1hld or Ch2hld). If the remaining molar amount of the hydrogen after gas-solid reaction is N_g, the molar amount of the hydrogen absorbed by the sample, N_s, is:

$$N_s = N_0 - N_g \quad 3.1$$

and the weight percent (wt%) of absorbed hydrogen is given by:

$$wt\% = (N_s M_g / m) \times 100 \quad 3.2$$

where m is the mass of the sample and the molar mass of hydrogen is : $M_g = 1.0079 \times 2$ mol.

The hydrogen absorption kinetics was studied in *soak* mode. In this mode, the system fills the sample holder with the desired pressure and graphs the amount of absorbed hydrogen versus time. *Release* mode is used for studying desorption kinetics. In this mode, the pressure over the sample is reduced to a desired value by evacuating the holder, and a graph is drawn of desorbed hydrogen versus time. To study the pressure-composition isotherm (PCI) of a composite, the *PCI* (either *absorption* or *desorption*) mode was used.

Operation procedure for any of the above-mentioned modes is:

- Place the prepared sample into the holder in the glove box.
- Run the software.
- Enter mass, density, and other required data on the sample.
- Select mode and related data such as pressure and temperature.
- Run the program.

- Review the output data.
- Remove the sample and repeat the steps for a new sample.

(a)

(b)

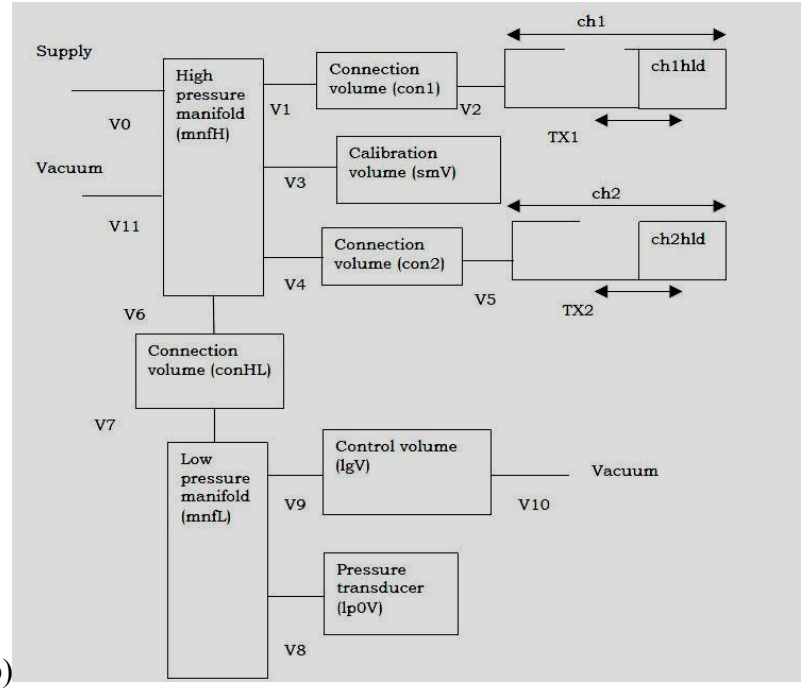

Fig. 3.6. (a) AMC Gas Reaction Controller. (b) A schematic of the chambers in the GRC unit.

The desired pressure, temperature, and other contributing data were different for different samples and are mentioned in the "experimental details" of each chapter.

To determine the hydrogen content absorbed by MgH_2-SiC during ball milling, carbon-hydrogen-nitrogen (CHN) analysis was carried out using a Carlo Erba Elemental Analyser Model 1106.

Chapter 4

Hydrogen storage properties of MgH_2–SiC composites

4.1 Introduction

As described in Section 2.7, magnesium metal or magnesium-based materials (alloys and composites) are considered to be promising candidate hydrogen storage materials, due to their high hydrogen storage capacity (e.g. MgH_2: 7.6 wt%), high reversibility, and low cost. However, the high thermodynamic stability of MgH_2 (ΔH= 74.5 kJ mol^{-1} H_2) limits its practical applications.

It has been reported that catalytic elements are beneficial in terms of governing the dissociation of molecular hydrogen, the diffusion of atomic hydrogen into the magnesium lattice, and hydride nucleation, while the fine particles produced by ball milling have more fresh surface area and active sites, which provide shorter and easier hydrogen diffusion paths (see 2.7.5). Thus, the kinetics of hydrogen storage is improved considerably in nanocrystalline MgH_2 produced by ball milling and the addition of suitable catalysts (see 2.7.6).

In this chapter, MgH_2/SiC composites were fabricated by ball milling Mg powder with SiC nanopowder in a Uni-Ball type mill under H_2 for 24 or 48 h. To the best of our knowledge, this is the first systematic investigation on MgH_2/SiC composites. By using SiC with a high hardness (9.2 on Mohs scale) as an additive, we successfully decreased the grain size of the MgH_2, increased the interface density, and prevented the agglomeration of MgH_2 crystallites, which play an important role in hydrogen storage

properties. Results showed that a small amount of SiC has a positive effect on the kinetics, but it shows negative effects when the proportion of SiC is high (> 10 wt%).

4.2 Sample Preparation

MgH_2/SiC composites were fabricated through milling Mg powder (with Mg in the mixture fixed at 2 g in order to make the results comparable) with calculated amounts (2, 5, 10, 20 wt%) of SiC under a high purity hydrogen (99.999%) atmosphere for 24 h or 48 h. Milling was performed in shearing mode (see 3.2.1). After ball milling, the cylinder was opened in an argon filled glove box and all the powders were handled in high purity argon to protect them from oxidation and the absorption of moisture.

The direct consequences of the ball-milling process were a crystallite size reduction in the Mg and the uniform dispersion of the SiC nanoparticles within the Mg matrix. Meanwhile, Mg reacted with hydrogen gas and formed MgH_2, which was evidenced by the decreased pressure of hydrogen inside the ball-milling vial. The change in the hydrogen pressure with ball-milling time was monitored and recorded, as shown in Fig. 4.1. It can be observed that the 5 wt% SiC doped sample shows the quickest pressure decrease, which suggests that the addition of SiC is beneficial to the formation of MgH_2 nanocrystallites during the ball-milling process. However, on increasing the SiC doping level to 10 and 20 wt%, the pressure decrease slowed down, especially for the 20 wt% SiC doped sample, where the rate of decrease in the hydrogen pressure is even lower than that of the un-doped sample (pure Mg). After 24 h of ball milling, the pressure was still going down, suggesting that a 24 h ball milling is not enough for samples to convert to MgH_2 completely.

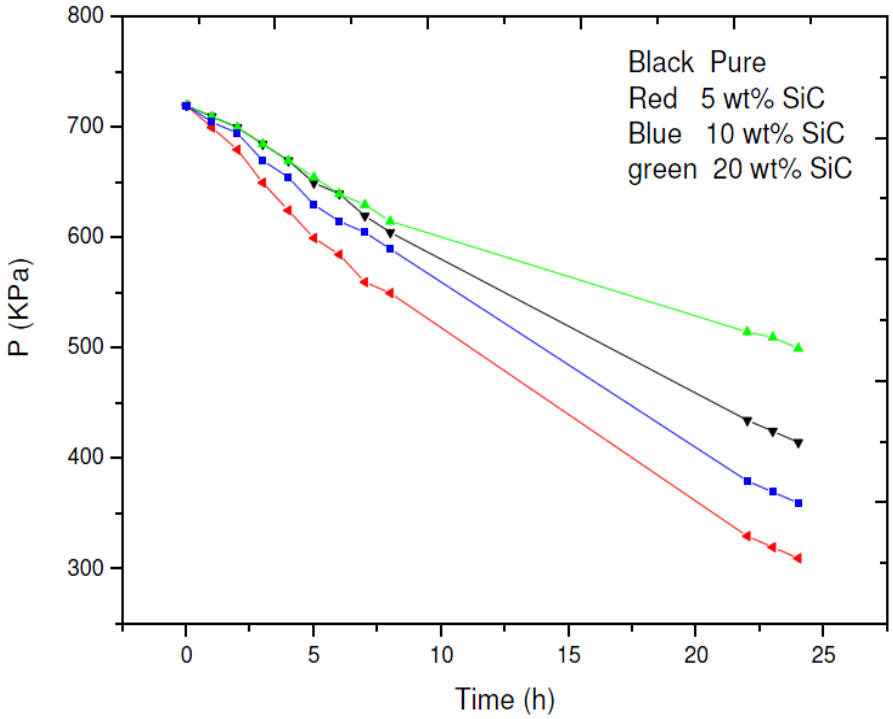

Fig. 4.1. Change of hydrogen pressure inside the ball-milling vial as a function of the ball-milling time.

4.3 Structure

4.3.1 X-ray diffraction

X-ray diffraction (XRD) patterns of the as-prepared samples and the samples after hydriding/dehydriding were obtained using a Philips PW 1730 generator and diffractometer (see 3.3.1).

The XRD patterns of the as-prepared samples (Fig. 4.2) exhibit peaks corresponding to Mg, β-MgH_2, and γ-MgH_2, together with Mg. Also, a weak peak is present at around 43.5°, which we have attributed to MgO, while there is no evidence of any SiC structure, due to the nanocrystalline nature of the SiC (< 10 nm).

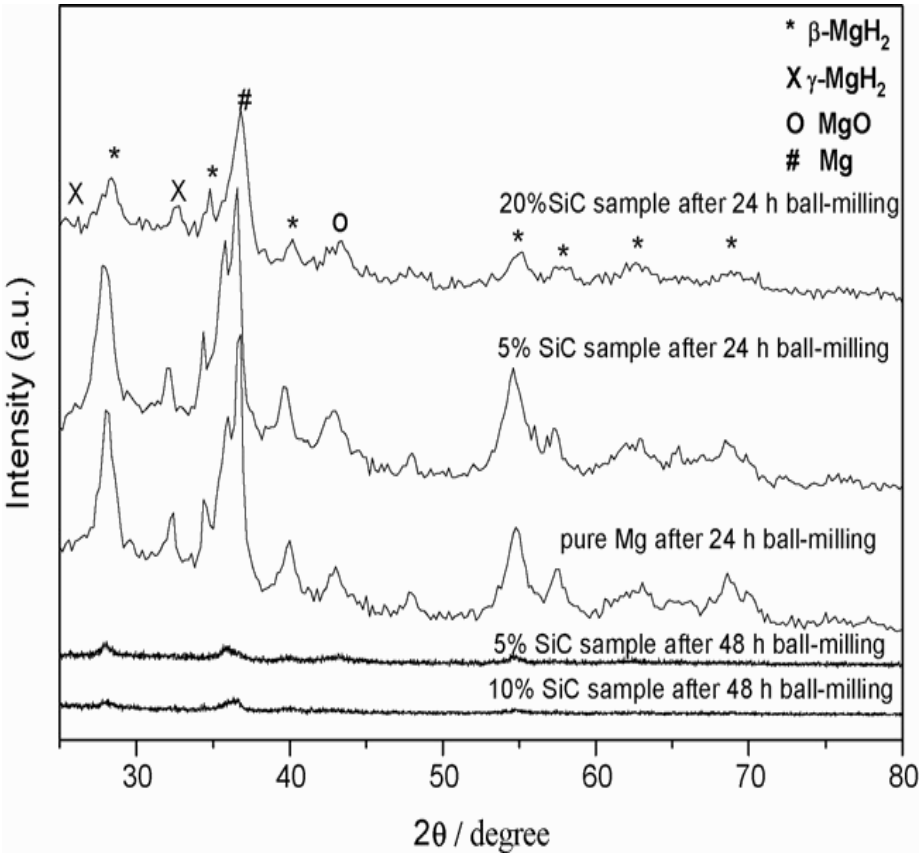

Fig. 4.2. X-ray diffraction patterns of the as-milled samples.

The broadening of peaks of the β-MgH_2 makes it possible to estimate the grain size, which is 21.8, 17.6, and 9.2 nm for the un-doped, 5 wt% SiC, and 20 wt% SiC doped samples, respectively. The results clearly demonstrate that the addition of SiC can help to generate smaller MgH_2 nanocrystals. By extending the ball-milling time to 48 h, it was found that the MgH_2 peaks in the XRD pattern became very broadened, and the Mg impurity peaks disappeared (as shown in Fig. 4.2), indicating that long ball milling is beneficial for the conversion of Mg powder to MgH_2 and that it is also helpful for reducing the grain sizes of the MgH_2 powders. In addition, there is a slight shift in the peaks indicating enlargement in the lattice parameters of the unit cells for doped samples.

4.3.2 TEM analysis

The microstructure of the 20 wt% SiC doped sample was further investigated by TEM and high resolution TEM (HRTEM) using a JEOL 2011 analytical instrument (see 3.3.2) with selected area electron diffraction (SAED) and dark-field imaging. As previously reported [194, 195], in the TEM chamber, hydrogen atoms are quickly knocked out by the electron beam, leading to decomposition, so the structures discussed here mainly refer to the grain structure of Mg. However, since the ring width in the diffraction patterns was found to be the same for MgH_2 before and Mg immediately after decomposition, the Mg grain size can be used to infer the MgH_2 one. TEM bright-field images (Fig. 4.3(a)) show the presence of dark particles embedded in the Mg matrix. By measuring the particle size in the relevant dark-field image, it was found that the majority of particles are less than 10 nm in size. The SiC component was identified from measurement of the lattice fringe spacings of the HRTEM image shown in Fig. 4.3(c).

The Mg particles under hydrogen are brittle, and during the ball-milling process, the hard SiC nanocrystals are uniformly distributed among the fragments of MgH_2. When the amount of SiC is high (> 10 wt%), the SiC nanocrystals may block the diffusion paths of hydrogen to some extent, and lead to a negative effect. The selected area electron diffraction pattern confirms that the as-prepared sample consists of a mixture of SiC, MgO, Mg, and MgH_2, which is consistent with the XRD results.

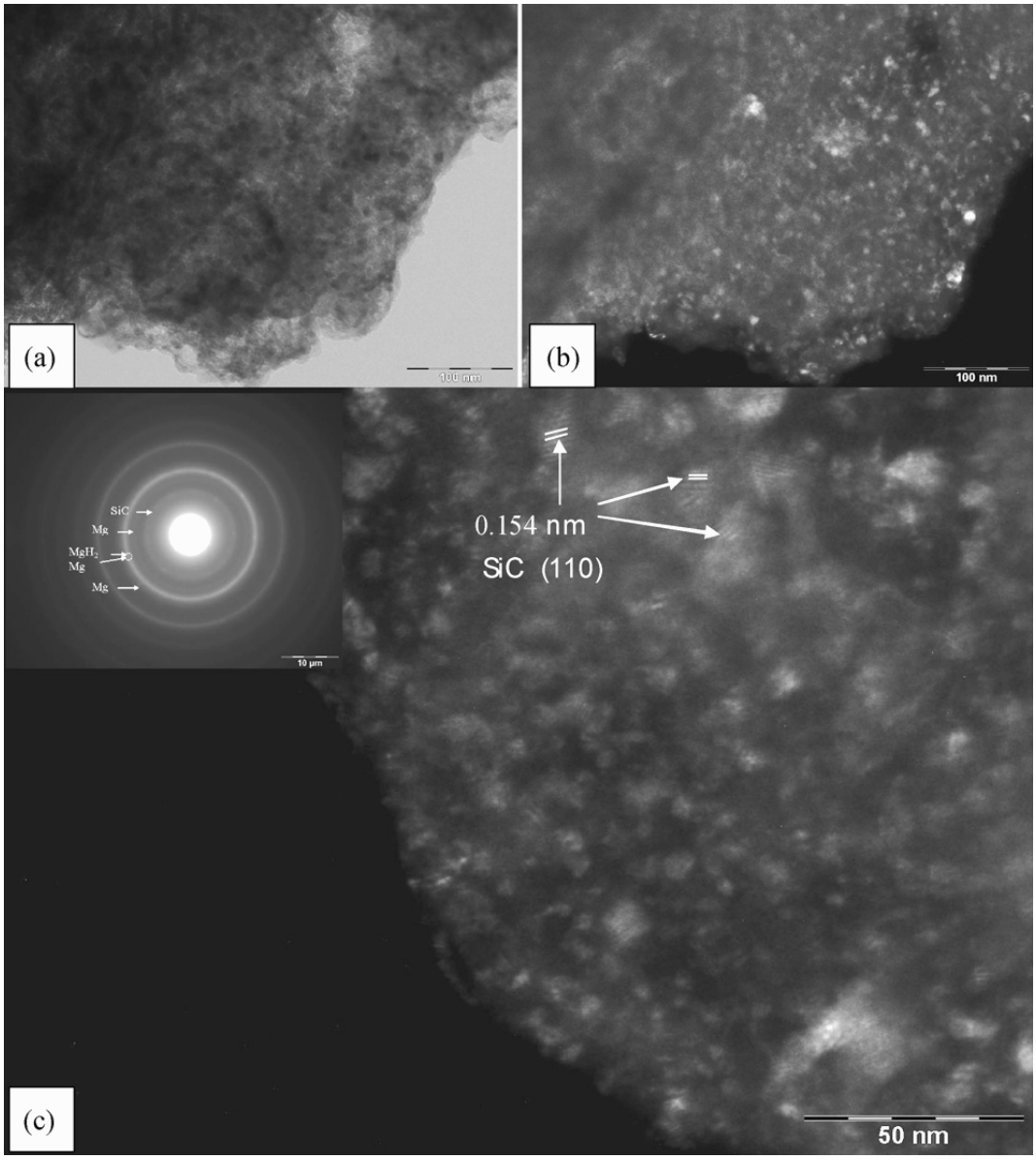

Fig. 4.3. TEM images of the as-prepared MgH_2 + 20 wt% SiC sample: (a) bright-field and (b) dark-field images at low magnifications; (c) dark-field image at higher magnification. Inset in (c) is the SAED pattern of the as-prepared MgH_2 + 20 wt% SiC sample.

4.4 Morphology

Fig. 4.4 shows scanning electron microscope images of the as-prepared MgH_2–SiC composites with different SiC ratios, which were characterized by using the JEOL (see

3.3.3). Samples were prepared by dispersing powders on lacy carbon support films. For all the samples, the particles have irregular shapes and are agglomerated together, which is a typical morphology for ball-milled powders. There is a broad particle size distribution for the un-doped sample, with various sized particles in a range from less than 1 μm to more than 10 μm. However, the uniformity of the particle size is improved for the SiC doped samples, especially for the samples with higher doping levels.

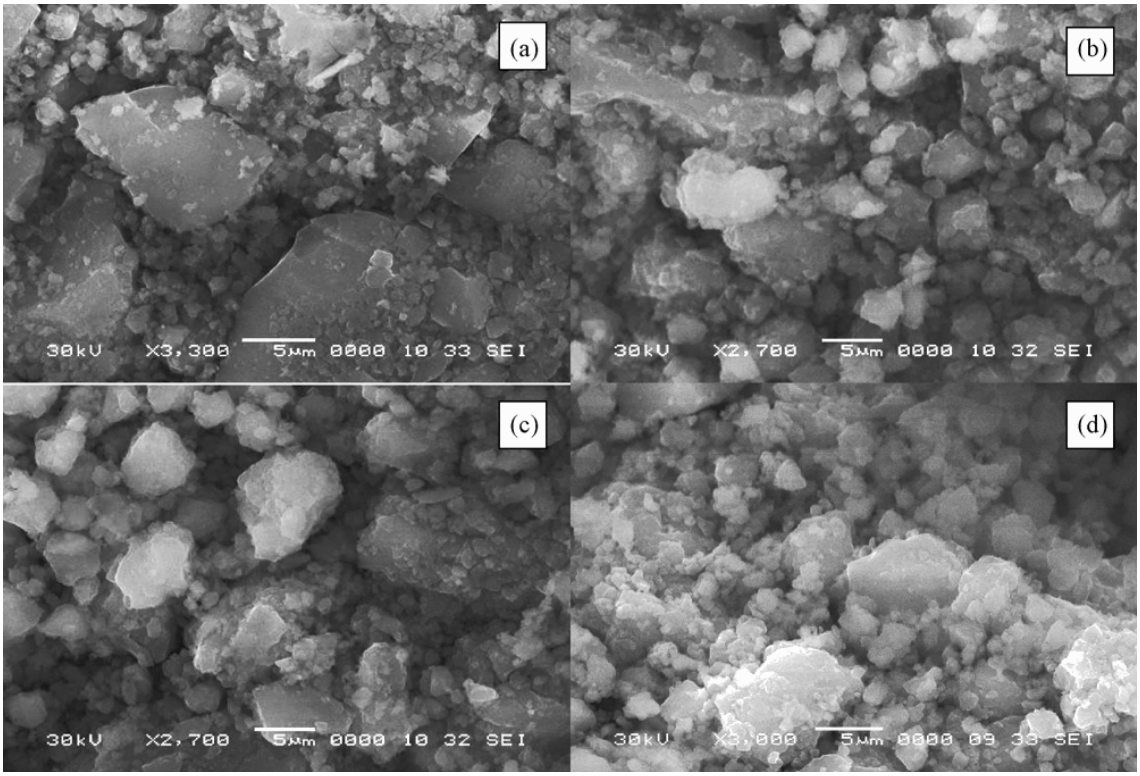

Fig. 4.4. SEM images of the as-milled samples after 24 h ball milling: (a) un-doped; (b) 5 wt% SiC; (c) 10 wt% SiC; and (d) 20 wt% SiC doped MgH_2 samples.

In fact, the Brunauer-Emmett-Teller (BET) surface area (see 3.3.4) of the as-prepared samples increases with increasing SiC doping level and is 7, 10, 12, and 16 m^2g^{-1} for the 0, 5, 10, and 20 wt% SiC doped sample, respectively. The SiC component in the composites helps to break the MgH_2 particles into smaller sizes due to the hardness of

the SiC. A smaller particle size enhances hydrogen absorption/desorption, because it decreases the diffusion length of hydrogen and makes the particle's reactive surface larger [196].

4.5 Thermal analysis

Thermal properties of samples were studied using a differential scanning calorimeter (DSC, Q100, see 3.4.1.1), with an argon flow rate of 50 ml min^{-1} at a heating rate of 10 °C min^{-1} up to 480 °C.

The DSC traces in Fig. 4.5 reveal the hydrogen desorption behaviour of the as-milled samples. The onset desorption temperature is reduced by about 20 °C between the 20 wt% SiC doped sample and the un-doped one.

On further comparison of the desorption peaks with those of the un-doped sample, it was found that the 20 wt% SiC doped sample shows a lower desorption temperature, by about 20 °C, than the un-doped one. All the SiC doped samples show a lower onset and a lower desorption temperature than the un-doped sample, and the hydrogen desorption temperature decreases with increasing SiC content.

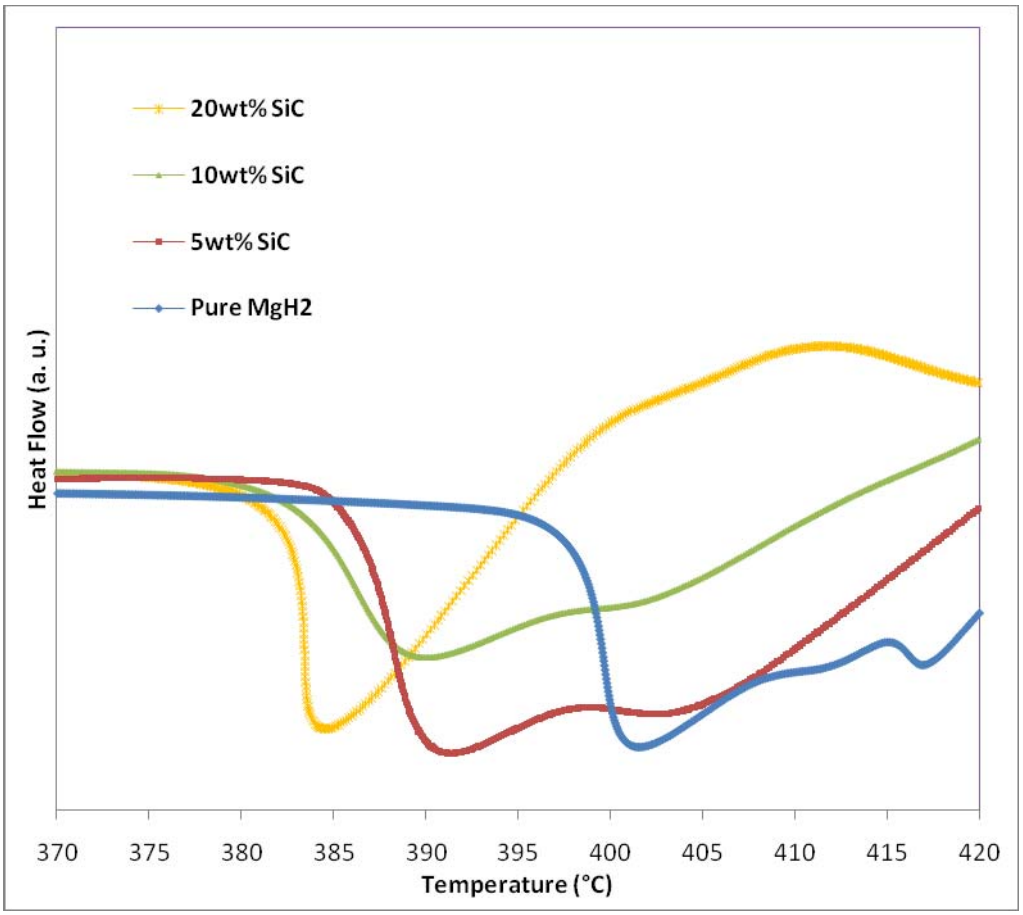

Fig. 4.5. DSC curves of as-milled samples after 24 h ball milling.

4.6 Hydrogenation and desorption

The hydrogen absorption/desorption behaviour and pressure-composition isotherms (PCI) of the samples were evaluated by the Sieverts method, using an AMC Gas Reactor Controller (see 3.4.2). The samples were dried under vacuum and degassed first, then the reactor was heated to 300 °C or 350 °C, and the samples were activated by hydriding/dehydriding 3 times.

4.6.1 Hydrogen Absorption

Fig. 4.6 shows the influence of SiC addition on the hydrogen absorption kinetics of MgH_2 under 30 bar hydrogen at 350 °C. The addition of the SiC improved the absorption kinetics of MgH_2 (Table 4.1). SiC-added samples with SiC amounts higher than 5 wt% required about 30 s to absorb 95% of their maximum absorbed H_2 content, while the bare MgH_2 and the MgH_2 + 2 wt% SiC samples took more than 50 s to reach this value. It was also found that the highest absorption performance in terms of capacity and kinetics was recorded for the 5 wt% SiC doped MgH_2.

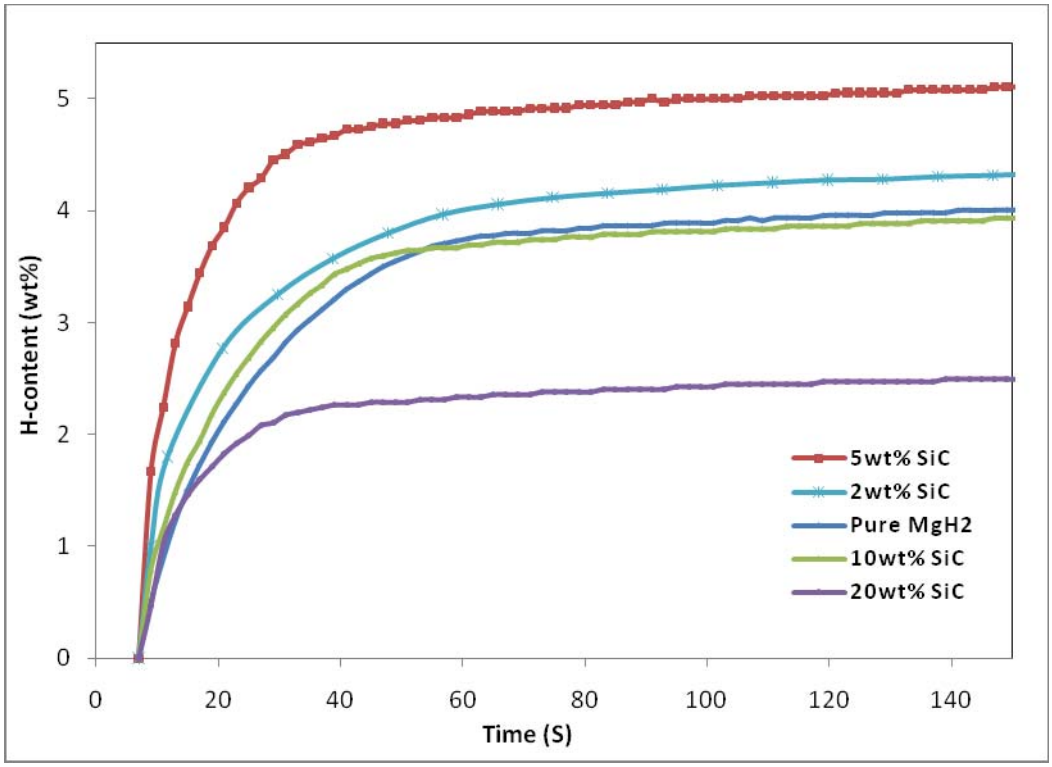

Fig. 4.6. Comparison of hydrogen absorption kinetics of the MgH_2 and the MgH_2 + *x* wt% SiC (*x* = 2, 5, 10, 20), at 350 °C under 30 bar hydrogen.

Table 4.1 Absorption rates, capacity, and hysteresis factor for MgH_2 and MgH_2 + *x* wt% SiC (*x* = 5%, 10%, or 20%) samples

Sample	Hydrogen Capacity (wt%)	Absorption rate between 0-30 s (wt% s^{-1})	Hysteresis factor
MgH_2-SiC (5 wt%)	6.349	0.150	0.347
MgH_2-SiC (10 wt%)	5.462	0.103	0.535
MgH_2-SiC (20 wt%)	3.458	0.90	0.556
MgH_2 (Pure)	5.620	0.067	0.345

4.6.2 Hydrogen Desorption

Fig. 4.7 presents the desorption behaviour of the samples under an initial hydrogen pressure of ~0.1 bar at 350 °C. Compared with the bare MgH_2 sample, the desorption kinetics increased significantly with low SiC addition (2 and 5 wt% SiC). The 5 wt% SiC-added sample shows the optimum desorption kinetics: it desorbed ~4.0 wt% of hydrogen in 400 s. However, the desorption rate became slower for the samples with increased amounts of SiC, especially for the MgH_2 + 20 wt% SiC sample. It is obvious that too much SiC addition will degrade the hydrogen absorption/desorption kinetics.

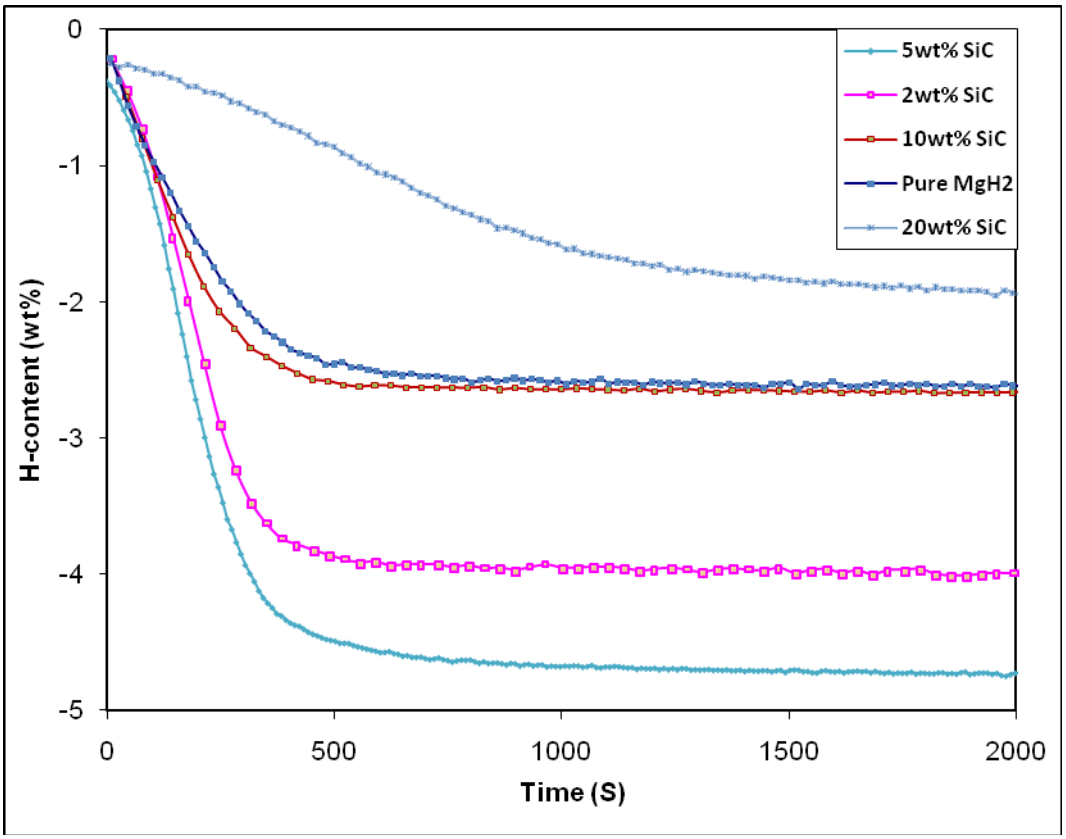

Fig. 4.7. Hydrogen desorption of the MgH_2 and the MgH_2 + *x* wt% SiC (*x* = 2, 5, 10, 20) under an initial hydrogen pressure of ~0.1 bar at 350 °C.

4.6.3 PCI

Fig. 4.8 shows pressure-composition-isotherm (PCI) curves of the samples at 350 °C. The PCI curves obtained in absorption and desorption mode exhibit single plateau behaviour for all samples. The hysteresis factors for different samples, defined as $\ln(P_{absorption}/P_{desorption})$, were calculated [197]. Here $P_{absorption}$ and $P_{desorption}$ are the plateau pressures of the absorption and desorption from the PCI curves, respectively.

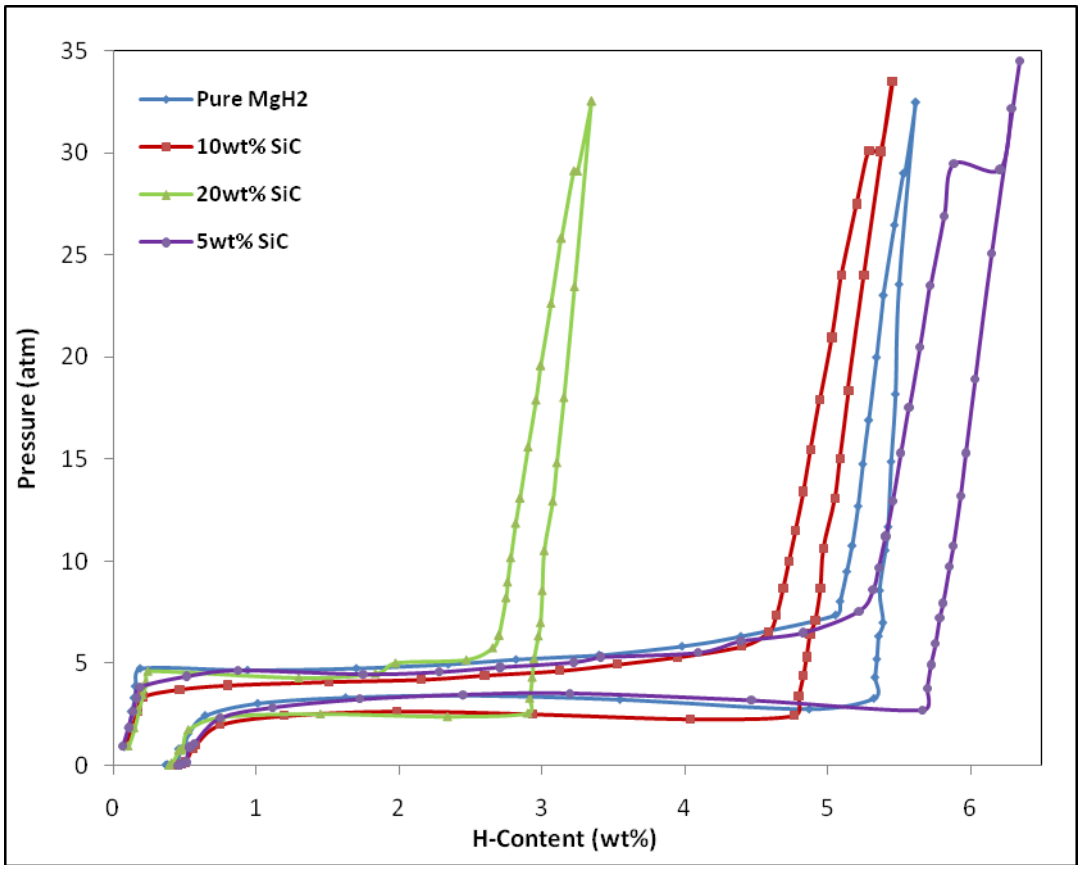

Fig. 4.8. Comparison of PCI absorption and desorption curves of the MgH_2 and the MgH_2 + x wt% SiC (x = 5, 10, 20 wt%), at T = 350°C.

The hysteresis factor is a quantitative measure of hysteresis loss, which originates from the strain and disorder of the β-MgH_2 lattice. The strain and disorder expand during absorption and relax during desorption, and the higher strain and disorder will increase the plateau pressure [198].

The hysteresis factors for the 10 and 20 wt% doped samples are much higher than that of the un-doped MgH_2 (Table 4.1), suggesting that the addition of a large amount of SiC during ball milling introduces strain and disorder into the MgH_2 lattice. However, the hysteresis factor for the 5 wt% doped sample is almost the same as that for the un-doped

one. The 5 wt% doped sample gave the best performance in terms of the capacity, the hydrogen absorption/desorption kinetics, and the hysteresis.

Considering the negative effects of heavy doping (low capacity, slow kinetics, and high hysteresis) and the lower hydrogen desorption temperature (from DSC results), we believe that a large amount of SiC can block the hydrogen diffusion, although its hardness can help to break up MgH_2 particles, thus reducing the grain size and increasing the active surface area of the MgH_2, thereby improving the hydrogen absorption/desorption kinetics. To further improve the hydrogen storage properties of MgH_2, a combination of a low amount of SiC with some other catalysts which can act as a bridge for hydrogen diffusion and a gateway for hydrogen breaking/recombination at the Mg/MgH_2 particle surface, is necessary. Research to optimize MgH_2–catalyst SiC composites is being conducted in our laboratory through tuning the components and material processing.

4.7 Conclusion

The effect of the addition of SiC in the range of 2–20 wt% on the hydrogen storage properties of MgH_2 prepared by ball milling has been studied for the first time. It has been found that the hardness of the SiC helps to reduce the grain size and increase the surface area of the MgH_2, which is beneficial to the hydrogen absorption/desorption properties of the MgH_2. However, heavy SiC doping introduces negative effects as well, such as lower capacity, high hysteresis, and a decreased absorption/desorption rate compared to the lightly doped sample. It is believed that the large amount of SiC in the heavily doped samples could block the H_2 diffusion paths, and this blocking effect overtakes the positive effects from the smaller grain size and higher surface area.

Further improvement of the hydrogen storage properties of MgH_2 may be achieved by combining a low amount of SiC with some other catalysts which could act as a bridge for hydrogen diffusion and a gateway for hydrogen breaking/recombination at the Mg/MgH_2 particle surface.

Chapter 5

Effects of SiC nanoparticles with and without Ni on the hydrogen storage properties of MgH_2

5.1 Introduction

In the previous chapter, MgH_2-SiC composites were fabricated and the results showed that hydrogen storage properties were improved by using a hard material with good conductivity (SiC), which could decrease the grain size of MgH_2, increase the concentration of defects, and prevent agglomeration of MgH_2 particles. The optimum results were for the MgH_2–5wt% SiC sample and a higher amount of SiC will introduce negative effects (see 4.8). In addition, it was predicted that doping the MgH_2–SiC system by a good catalyst, which can act as a bridge for hydrogen diffusion and emerge from MgH_2 particles, could have additional improvement in hydrogen storage properties of Magnesium.

On the other hand, Ni is a promising catalyst to improve the hydrogen storage properties of Mg-based hydrides. Liang et al. reported that adding 5wt% Ni enables MgH_2 to release 5wt% of hydrogen at 300 °C in about 6 min. Kanoya et al. [199] showed that Mg–Ni–Fe composite prepared by only a 15 min ball milling can absorb and desorb almost 7.5wt% at 350 °C . Hanada et al. [153] reported that 2 mol% nano-Ni shows superior hydrogen storage properties and that 6.5wt% hydrogen is desorbed in the range of 150–250 °C at a heating rate of 5 °C /min. They believe that the nanosize nature of

the Ni particles had a strong effect in terms of H_2 dissociation and H-atom recombination.

In this chapter, in order to further improve the hydrogen storage properties of MgH_2, MgH_2–SiC(5wt%)–Ni(10wt%) composite was fabricated by ball milling Mg powder with SiC and Ni nanopowders in a H_2 atmosphere for 24 h. The results showed that the addition of Ni to the sample enhanced the hydrogen storage properties of MgH_2. Based on the kinetics investigation, it is proposed that the good dispersion of SiC/Ni particles among the MgH_2 has changed the rate-determining steps from ‘‘surface controlled’’ to ‘‘nucleation and three dimensional growth of the existing nuclei’’.

5.2 Samples' Preparation

Pure MgH_2 powder, MgH_2+5wt%SiC and MgH_2+5wt%SiC+10wt%Ni were synthesized by milling Mg powder, SiC nanopowder, and Ni nanopowder (see table 3.1) in a magnetically controlled Uni-Ball-Mill 5 (see 3.2.1) for 24 h under hydrogen atmosphere. For all of the samples, the starting pressure was 720 kPa, the ball-to-powder weight ratio was about 44:1, and the rotation speed 30 rpm. After ball milling, the cylinder was opened in an argon filled glove box. The fabrication conditions for all these samples were kept the same as in previous chapter (MgH_2–SiC composites) for comparison purposes.

Fig 5.1 shows the change in the hydrogen pressure with ball-milling time. The rate of pressure reduction for the MgH_2+5wt% SiC+10wt% Ni sample is faster than other samples explicitly which suggests that doping the system of Mg-SiC with nano nickel particles is valuable to the formation of MgH_2 during ball-milling process. The same as

MgH_2-SiC samples (see 4.2), after 24 h the pressure is slowly going down for the MgH_2+5wt% SiC+10wt% Ni sample as well which prove that this time is not enough for the conversion of Mg to MgH_2. However, as the aim of the investigation was the effect of the catalyst, it does not affect the conclusion.

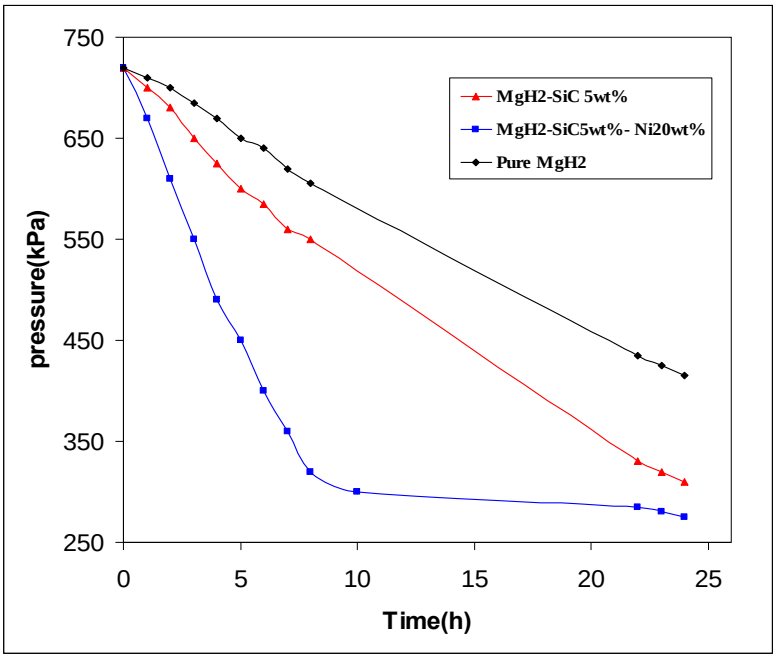

Fig 5.1. Change of hydrogen pressure inside the ball milling vial as a function of the ball-milling time.

5.3 X-ray diffraction

The phase compositions of the as-prepared samples were investigated with a Philips PW 1730 X-ray diffractometer (see 3.3.1). Fig 5.2 shows the XRD patterns obtained from the as-prepared composites. They exhibit peaks corresponding to β-MgH2 (Joint Committee on Powder Diffraction Standards (JCPDS) Card No. 12-0697), Mg, and a weak peak of MgO. The Mg peak indicates that a 24 h ball milling is not enough for samples to be completely converted to hydride, which is similar to the case of MgH_2–

SiC nanocomposites (see 4.3.1), while the Mg peak of the sample with Ni is weaker compared to samples without Ni. Considering that all samples were handled and ball milled under exactly the same conditions, we believe that Mg converts to MgH_2 faster in the presence of Ni.

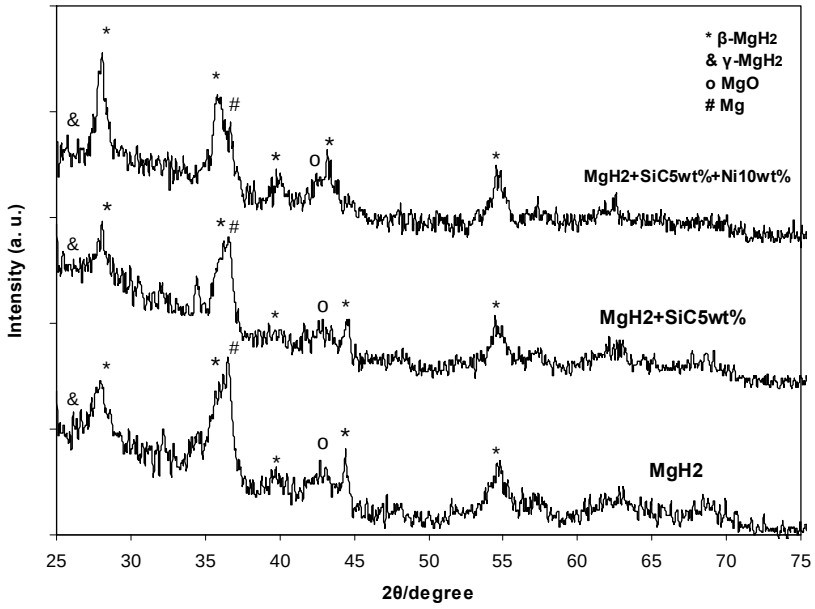

Fig. 5.2. XRD patterns for as-prepared samples.

For the MgH_2 and MgH_2–SiC samples there are two peaks corresponding to γ-MgH_2 (JCPDS No. 351184), but these peaks are very small for the sample with nickel, which is probably due to broad diffraction and increasing X-ray absorption as a result of the product being highly deformed. There is no any peak related to any interaction between Mg and Ni such as Mg_2Ni or $MgNi_2$.

The XRD patterns for all samples showed magnesium hydride converted totally to magnesium after dehydrogenation. Fig. 5.3 shows it for the MgH_2+5wt% SiC+10wt% Ni sample.

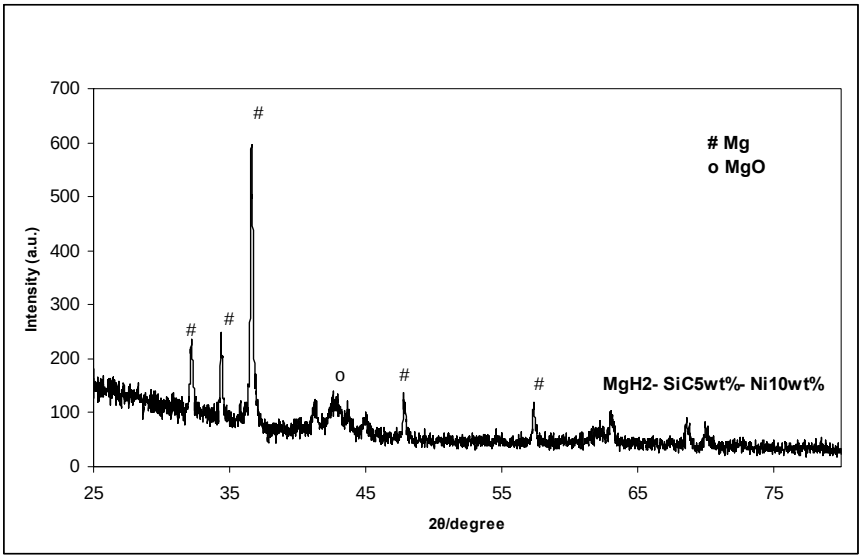

Fig. 5.3. X-ray diffraction patterns of the MgH_2+5wt% SiC+10wt% Ni sample after dehydrogenation.

5.4 Morphology

Scanning electron microscope mapping (see 3.3.3)of magnesium, SiC, and Ni allowed visualization of the distribution of these elements. SEM images are shown in Fig 5.4.

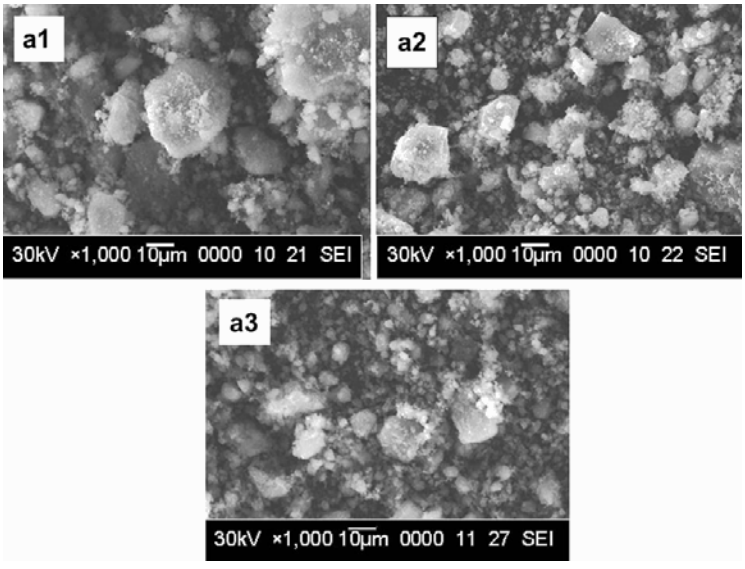

Fig. 5.4. SEM images for the samples: (a1) pure MgH_2, (a2) MgH_2–SiC 5wt%, (a3) MgH_2–SiC 5wt%–Ni 10wt%.

The images of the samples in Fig 5.4 are almost the same, except that agglomeration for the pure MgH_2 sample is a bit more extensive than for the others, and it confirms our results in last chapter that SiC helps to break MgH_2 particles into smaller sizes due to its natural hardness (see 4.4). Furthermore, the existence of SiC in the samples can prevent agglomeration of MgH_2 particles. This property of SiC can improve MgH_2 hydrogen hydriding/dehydridyng properties because of the decreased diffusion length. The SEM mapping images in Fig. 5.5 show that both nickel and silicon carbide are dispersed homogeneously among the MgH2 particles.

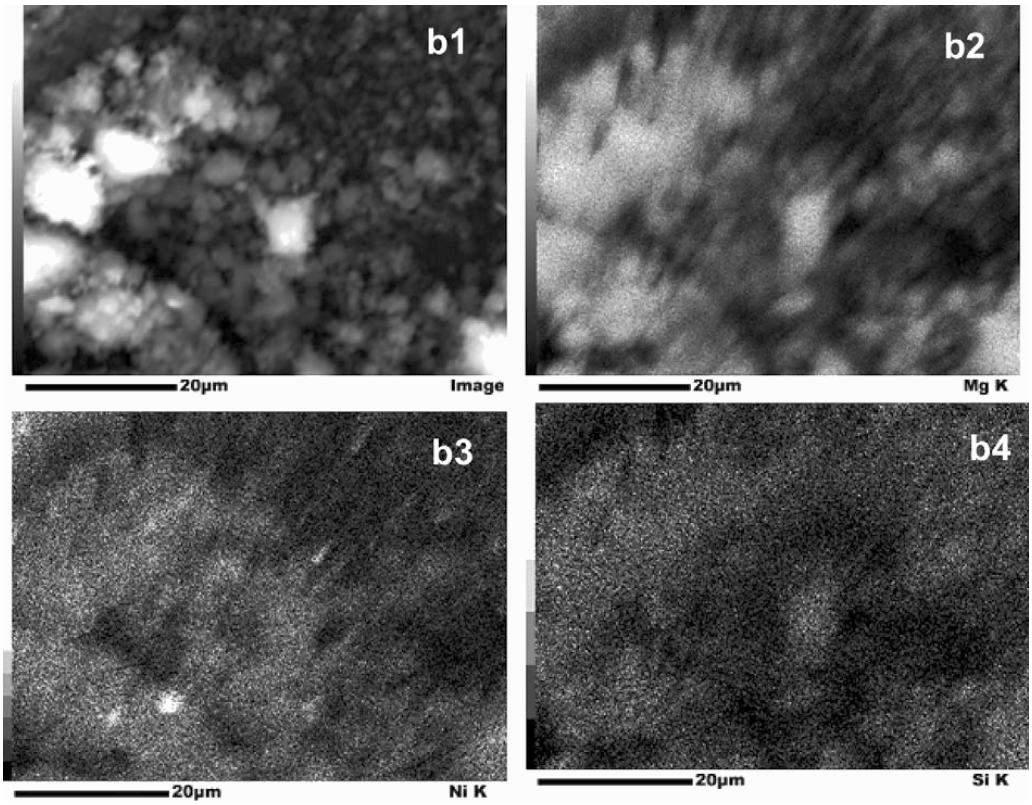

Fig. 5.5. Mapping of the MgH_2–SiC–Ni sample: (b1) shows a micrograph of the overall area of the sample to be mapped. (b2), (b3) and (b4) show the elemental mapping of Mg, Ni and Si, respectively.

5.5 Thermal analysis

Differential scanning calorimetry (DSC, Q100, see 3.4.1.1) analysis was conducted to investigate the thermal behaviour of the samples with an argon flow rate of 50 ml/min and a heating rate of 10 °C/min to 500 °C. Fig. 5.6 shows the DSC traces of the samples. As can be seen from the figure, the desorption temperature, T_{des}, is reduced by about 20 °C for MgH_2–SiC and by about 80 °C for the sample with Ni. These results are in agreement with our previous results which showed that T_{des} is decreased by increasing the amount of SiC in MgH_2 (see 4.5) and, on the other hand, that adding Ni can significantly reduce T_{des}.

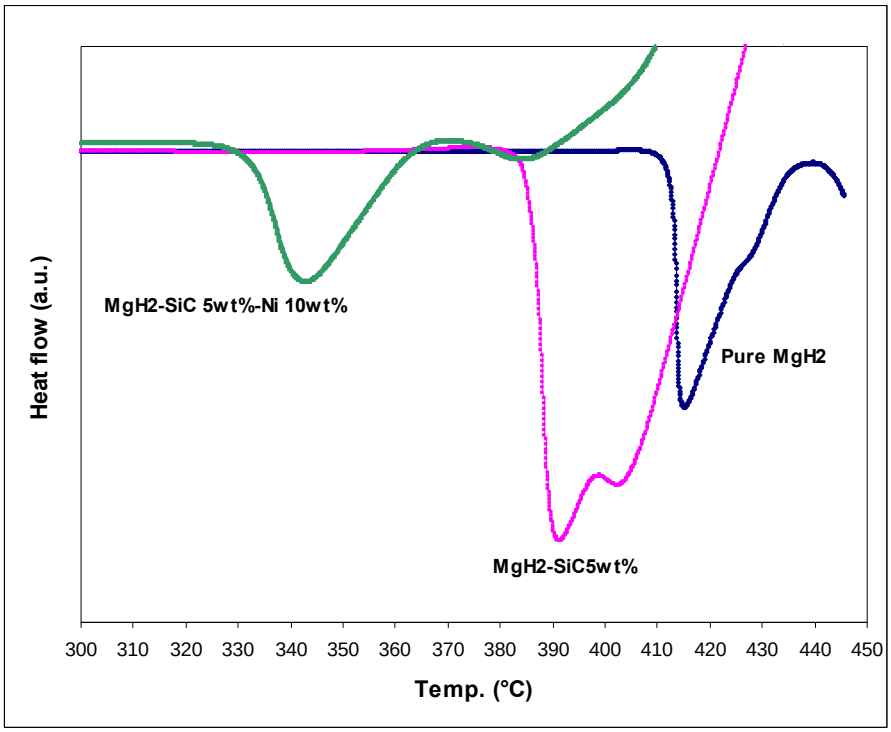

Fig. 5.6 DSC curves for all samples.

5.6 Hydrogenation and desorption

The hydrogen absorption/desorption of the samples was studied by Sievert's method at 300 °C using an AMC pressure– composition isotherm measurement instrument (see 3.4.2). The samples were put into a holder in the glove box and were activated by hydriding/dehydriding 3 times before testing.

5.6.1 Hydrogen Absorption

Hydrogen absorption (under 30 atm hydrogen pressure) of the samples at 300 °C is shown in Fig. 5.7. The MgH_2–SiC– Ni absorbed 5.1wt% hydrogen at this temperature, while for SiC doped and un-doped samples this amount was reduced to 4.5 and 3.3wt%, respectively. At 300 °C also, the sample with Ni absorbed 95% of its maximum hydrogen capacity within 59 s. So, the addition of SiC and Ni powder improved both the hydrogen absorption kinetics and the hydrogen storage capacity of MgH_2 in this fabrication and under these measurement conditions.

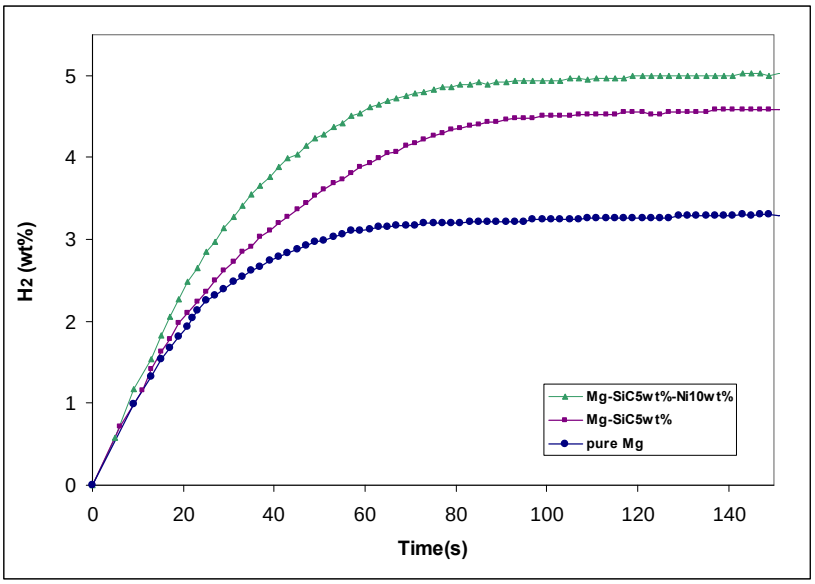

Fig. 5.7. Hydrogen absorption for all samples at 300 °C and 30 atm.

5.6.2 Hydrogen desorption

Hydrogen desorption behaviours (under 0.1 atm) of the samples at 300 °C is shown in Figs. 5.8. MgH_2–SiC–Ni decomposed and desorbed 4.7wt% hydrogen at 300 °C, while the MgH_2–SiC and pure MgH_2 samples released 4.3 and 2.7wt%, respectively, at the same temperature. SiC can improve the hydrogen storage properties of MgH_2 powder by decreasing the grain size and increasing the defect concentration in MgH_2 particles, with the optimum results occurring for MgH_2–SiC 5wt%. Additional improvements are found by adding Ni to MgH_2–SiC 5wt% composite, which is related to the strong catalytic effect of Ni nanoparticles in recombination hydrogen atoms to hydrogen molecules.

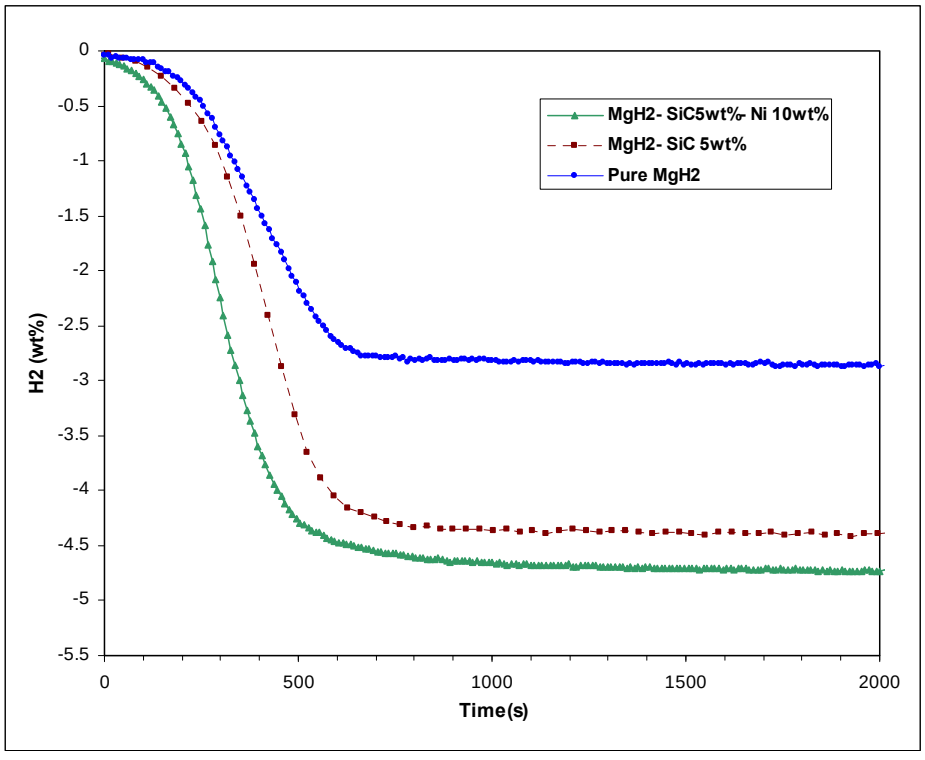

Fig. 5.8. Hydrogen desorption for the samples at 300 °C and 0.1 atm pressure.

5.6.3 PCI

A comparison pressure-composition-isotherm (PCI) absorption and desorption curves of the MgH_2+5wt% SiC and MgH_2+5wt% SiC+10wt% Ni samples are shown in Fig. 5.9. The hysteresis factor, $\ln(P_{absorption}/P_{desorption})$, for these samples are 1.17 and 0.6 respectively. This factor is a quantitative measure of hysteresis loss, which originates from the strain and disorder of the magnesium hydride lattice (see 4.6.3). The calculated amount of hysteresis factore indicates that although addition of SiC introduce strain and disorder into the MgH_2 lattice during ball-milling, however doping the sample with Ni improve returning back of the lattice and becoming relax.

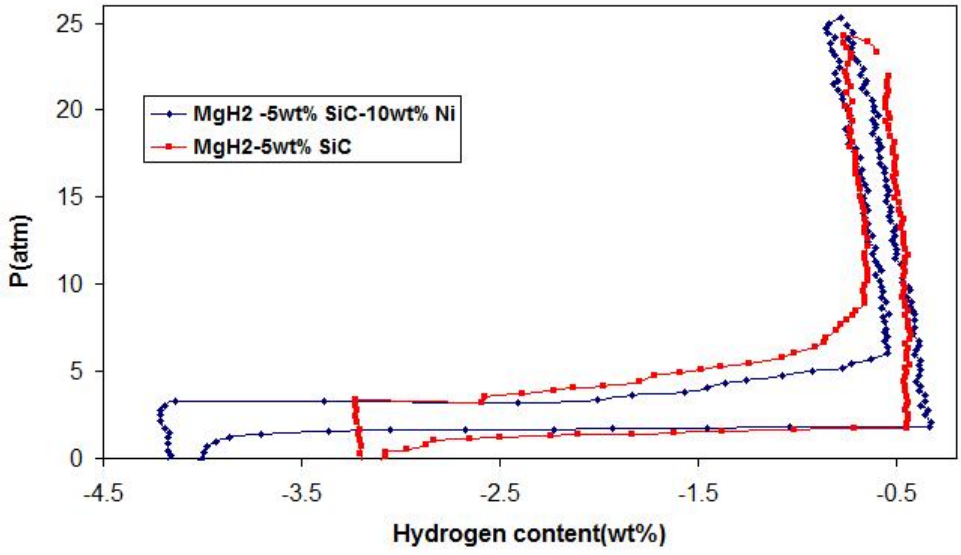

Fig. 5.9. Comparison of PCI absorption/desorption curves of the MgH_2+5wt% SiC and MgH_2+5wt% SiC+10wt% Ni samples.

It was found from the previous chapter's results that low amount of SiC improves hydrogen storage properties by reducing the grain size and increasing the active surface area of MgH_2. It was expected that doping the MgH_2-SiC system by a catalyst, which can act as a gateway for hydrogen dissociation and recombination at the magnesium and

magnesium hydride particles surface, could have additional improvement in hydrogen sorption properties. The significant improvement in important aspects of hydrogen sorption properties of MgH_2-SiC-Ni system, such as the: hydrogen storage capacity, the hydrogen absorption/desorption kinetics, and the hysteresis, verified this prediction.

To find that which hydrogen absorption/desorption steps of magnesium may modify by SiC and SiC-Ni addition, the hydriding/dehydriding kinetics investigation has been studied.

5.7 Hydriding/dehydriding kinetic investigation

It has explained in section 2.6.2 that hydrogen absorption and desorption are composed of several steps and the one which is very slow in comparison with the other steps is known as the rate-limiting step. There are also some theoretical kinetics equations related to different rate-limiting steps which are summarized in Table 2.6 with descriptions of their corresponding models. Description of the absorption and desorption kinetics is possible by plotting the left side equations in Table 2.6 versus time and the plot giving the best linearity determines the rate limiting step (see 2.6.2).

The resulting curves of kinetic equations applied to absorption data are shown in Fig. 5.10. As can be seen, the kinetic rate-determining steps for both pure and Ni-doped samples are best described by three-dimensional growth diffusion controlled by decreasing interface velocity (CV-3D, variable velocity).

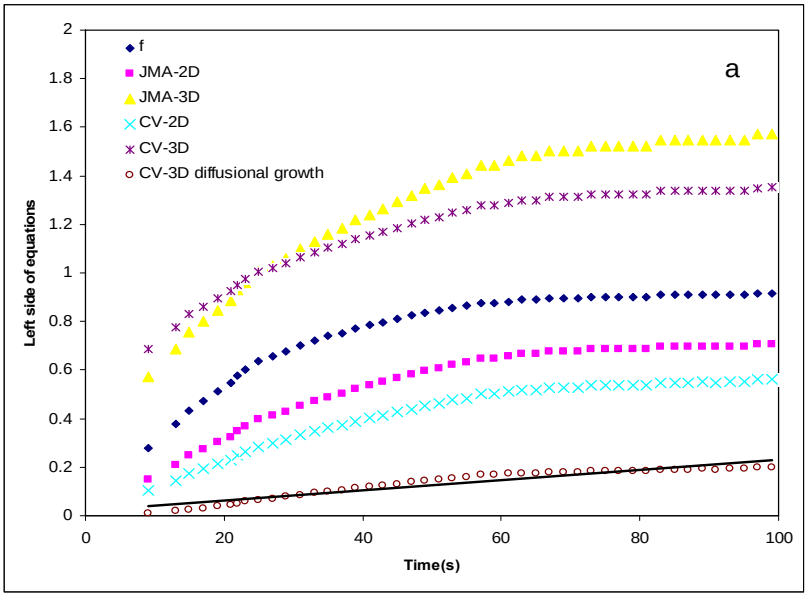

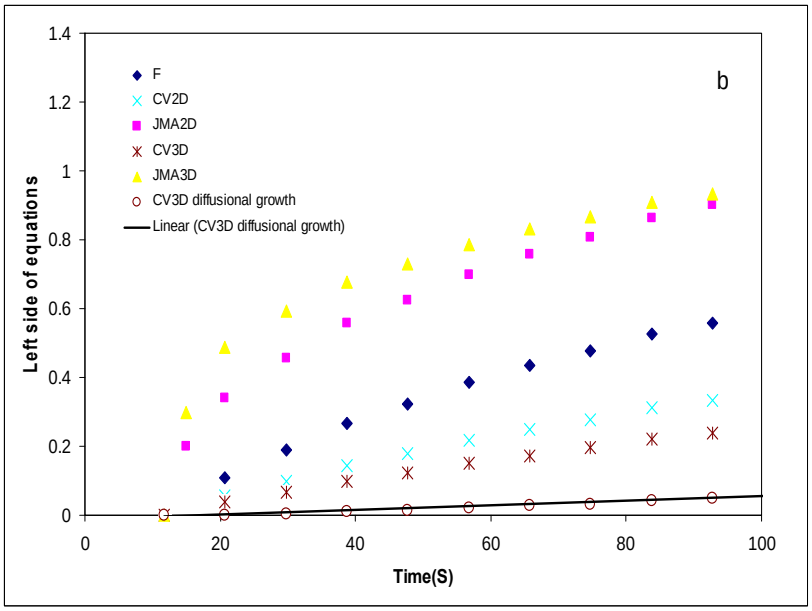

Fig. 5.10. The resulting curves of different kinetic equations applied to absorption data of (a) un-doped MgH_2, and (b) MgH_2–SiC–Ni.

When a layer of magnesium hydride is formed, diffusion of hydrogen atoms through this protective hydride layer will control the reaction. The velocity of hydrogen penetration decreases with increasing thickness of the hydride layer. The resulting kinetics of the absorption reaction is in agreement with Yonkeu et al. [200] on the

catalytic effects of body centred cubic (BCC) alloys and Barkhordarian et al. [148] on the catalytic effects of Nb_2O_5.

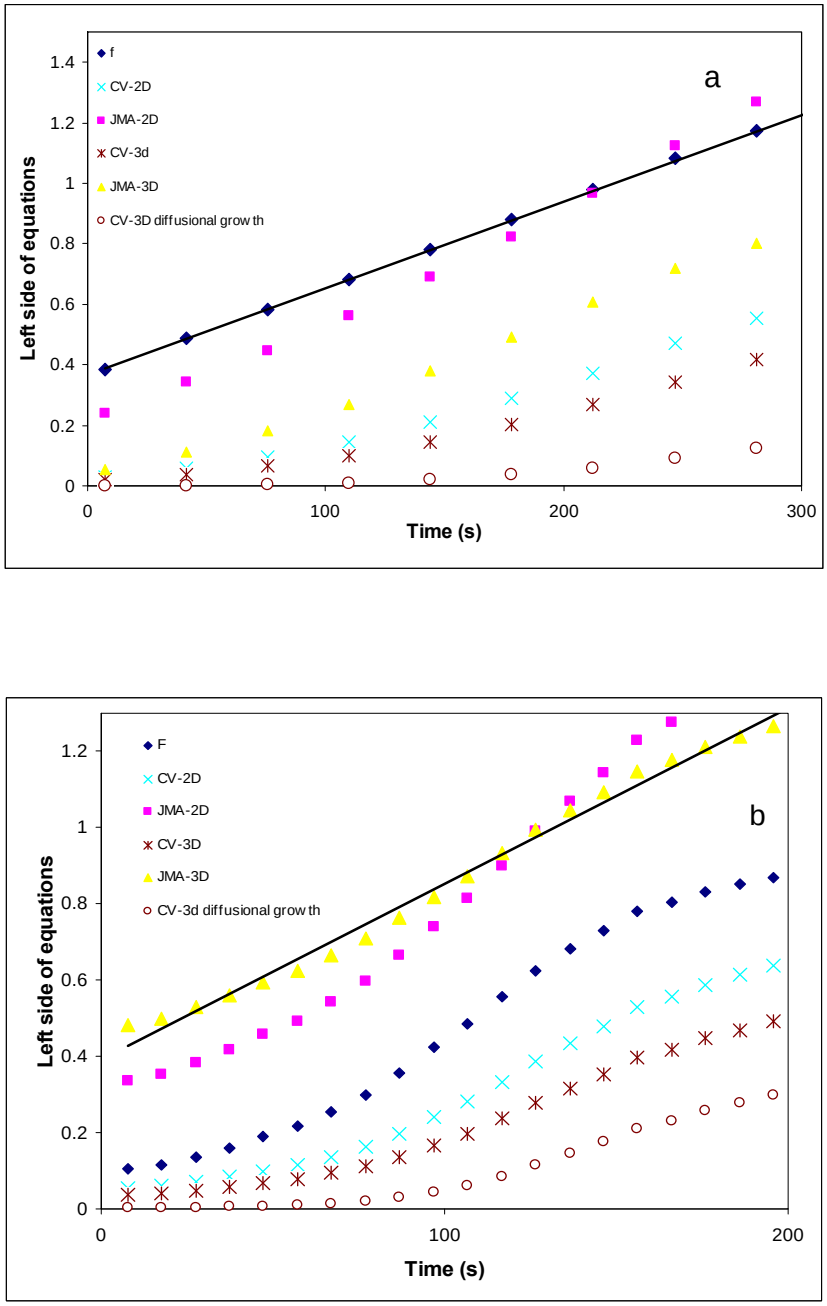

Fig. 5.11. The resulting curves of different kinetic equations applied to desorption data of (a) undoped MgH_2, and (b) MgH_2–SiC–Ni.

The hydrogen desorption reaction for pure MgH_2, as shown in Fig. 5.11(a), is controlled by recombination of chemisorbed hydrogen atoms (surface controlled), which is to be expected because magnesium has no catalytic effect towards the recombination of hydrogen atoms into hydrogen molecules. However, Ni is a good catalyst for hydrogen molecule dissociation to hydrogen atoms and vice versa, and for the sample with Ni, the hydrogen desorption reaction is controlled by bulk nucleation and three-dimensional growth of the existing nuclei (JMA-3D), which are Mg in our case (Fig. 5.11(b)).

A good dispersion of the nanosized Ni particles, as shown in the SEM images, increases the amount of nucleation sites, which is responsible for the bulk desorption properties. Liang et al. [152], and Honada et al. [153], claimed that two-dimensional growth of existing nuclei (JMA-2D) is the rate-limiting step for their Ni doped Mg samples. The difference is perhaps related to the existing and good dispersion of SiC in our samples. SiC nanoparticles increase the concentration of defects that change the growth of nuclei from two-dimensional to three-dimensional.

5.8 Conclusion

In this chapter, the effects of the addition of SiC 5wt% and SiC 5wt%–Ni 10wt% on the hydrogen storage properties of MgH_2 were investigated. The results of adding SiC confirmed our results in previous chapter and improved the hydrogen absorption/ desorption kinetics and capacity of MgH_2 by increasing the surface area and defect concentration. An additional improvement was achieved by adding Ni to the MgH_2/SiC composite because of catalytic effects of Ni. Kinetic investigation showed that for un-doped MgH_2, the rate-limiting step during desorption is the recombination of chemisorbed hydrogen atoms (surface controlled), while for the SiC/Ni doped sample,

that step is bulk nucleation and three-dimensional growth of the existing nuclei, which is related to the catalytic effect of Ni towards recombination of hydrogen atoms into hydrogen molecules and the increase in defects caused by SiC.

Chapter 6

Hydrogen storage properties of Mg-BCC composite

6.1 Introduction

One type of materials which showed good catalytic effects on hydrogen storage properties of magnesium are Ti-based body centred cubic materials (see 2.7.6.3). There are different kinds of these materials which vary by changing the proportion of Ti and other elements in the combination, such as V, Mn and other transition metals. Gu et al., [181] and Liu et al. [201] investigated the effects of two kinds of body centre cubic alloys on hydrogen storage properties of MgH_2 and found that these alloys improve the hydrogen absorption kinetic of MgH_2 by acting as a hydrogen diffusion path.

In this chapter, 10 wt% of a new body centre cubic alloys, $Ti_{0.4}Mn_{0.22}Cr_{0.1}V_{0.28}$ called BCC, added to MgH_2 by using uni ball mill 5. In addition to investigate the effect of ball milling condition of the hydrogen storage properties, two samples with ball to powder weight ratio (BPWR) of 200 and 100 , has been fabricated and hydrogen storage properties and the structural changes of the composites have been studied in details.

6.2 Sample Preparation

In the first step, the BCC alloy sample was prepared by magnetic levitation melting method. A fifty grams ingot was turned over and remelted for 4 times to ensure its homogeneity. Then the BCC alloy was quenched on a water-cooled rotating molybdenum disc with a rate of 20 m/s. In the second step, MgH_2 and MgH_2+10wt%

BCC composites were fabricated through ball milling Mg powder (see 3.1) with calculated amount of the BCC. The ball milling machine was uni-ball mill type in impact mode (see 3.2.1) and all samples were ball milled under hydrogen atmosphere for 24h with starting hydrogen pressure 700 kPa and rotation speed 30 rpm. To find the effect of ball milling conditions on the MgH_2+10wt% BCC composites, two samples were fabricated with ball to powder weight ratios (BPWR) 100 and 200. All handling of the powders, before and after ball milling, were performed in an argon filled glow box (oxygen and water content, each below 1ppm).

During ball milling Mg reacted with hydrogen gas and formed MgH_2 which was evidenced by the decreased hydrogen pressure inside the ball milling vial. This decreasing of the pressure is shown in Fig. 6.1. It can be observed that the pressure decrease for both the BCC doped samples quicker than pure one which it means the BCC acts as a catalyst to convert Mg to MgH_2 during ball milling. After 24h ball milling, the hydrogen pressure was still decreasing which suggest that this time is not enough for the samples to become hydride completely. XRD patterns confirmed these results (see 6.3).

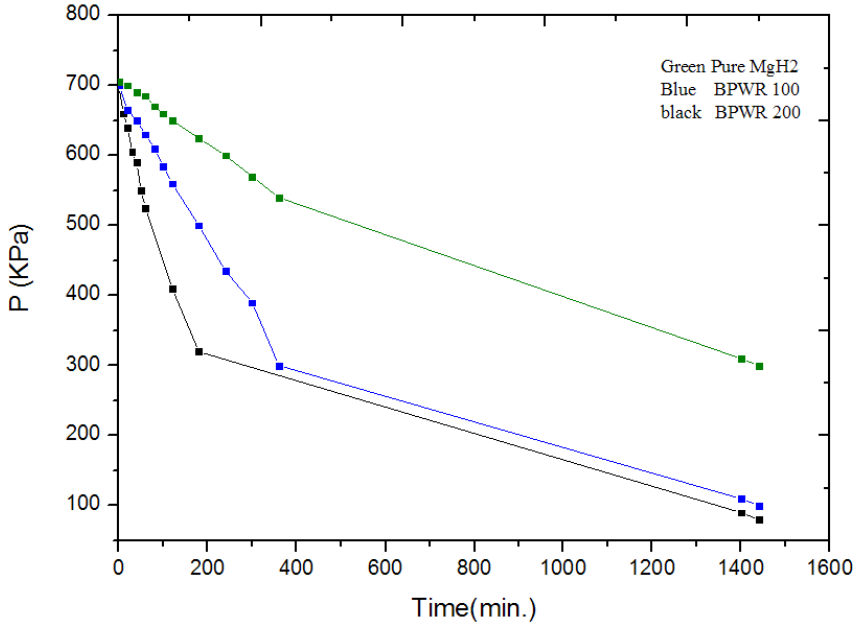

Fig. 6.1. Change of hydrogen pressure as a function of ball milling time.

6.3 X-ray diffraction

X-ray diffraction (XRD) patterns of the as-prepared samples were obtained with a Philips PW 1730 generator and diffractometer (see 3.3.1).

The XRD patterns which are shown in Fig. 6.2. The peaks correspond to β-MgH_2 (JCPDS-12-0697), Mg, and a weak peak of MgO. No other peaks of any new composite were present which indicates that no new alloy phase was formed. The Mg peak for the pure sample is larger than those of the Mg-BCC samples, which is similar to our previous results on MgH_2-SiC (see 4.3.1) and MgH_2-SiC-Ni (see 5.3.1), while the BCC as a catalyst had a very good effect on the conversion of magnesium to magnesium hydride. An additional improvement in this conversion can be observed by increasing the ball to powder weight ratio (BPWR) and the BPWR 200 sample shows the largest peak of MgH_2. The XRD patterns also exhibit a peak broadening that is corresponds to

increasing amounts of defects and disorder in the samples during ball milling and, as a result, composite materials with smaller crystal size were formed [201].

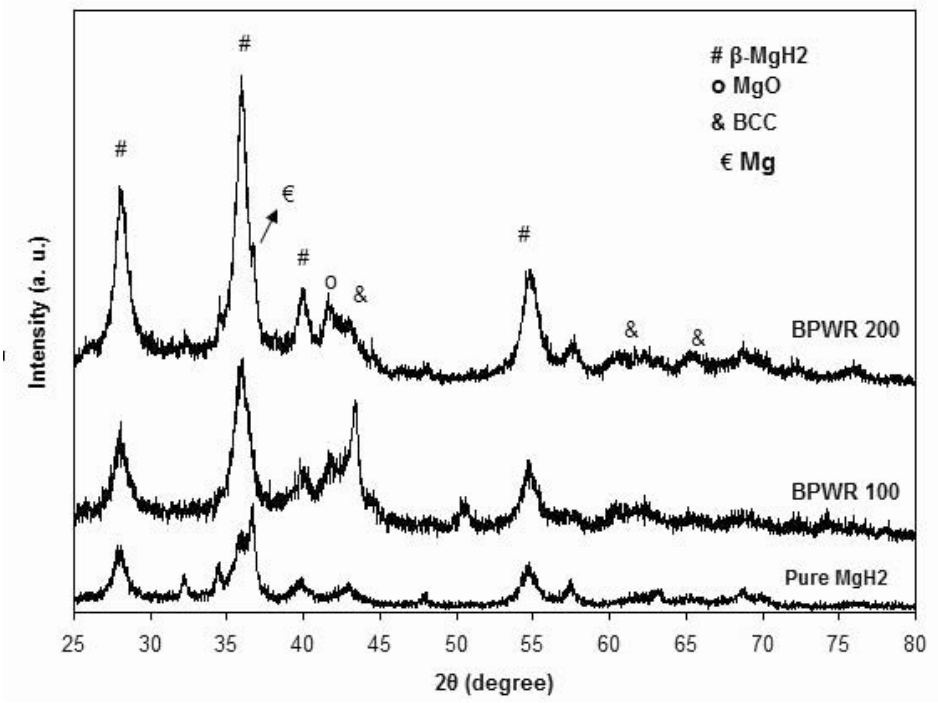

Fig. 6.2. XRD patterns of as-prepared samples.

6.4 Morphology

The morphology of the composites and visualization of the distribution of the elements were characterized by using scanning electron microscopy (see 3.3.3) and SEM mapping, respectively.

Energy dispersive spectroscopy (EDS) element maps of MgH_2-BCC (BPWR 200) are shown in Fig. 6.3. This mapping shows that all elements in the BCC are distributed homogeneously among the MgH_2 particles.

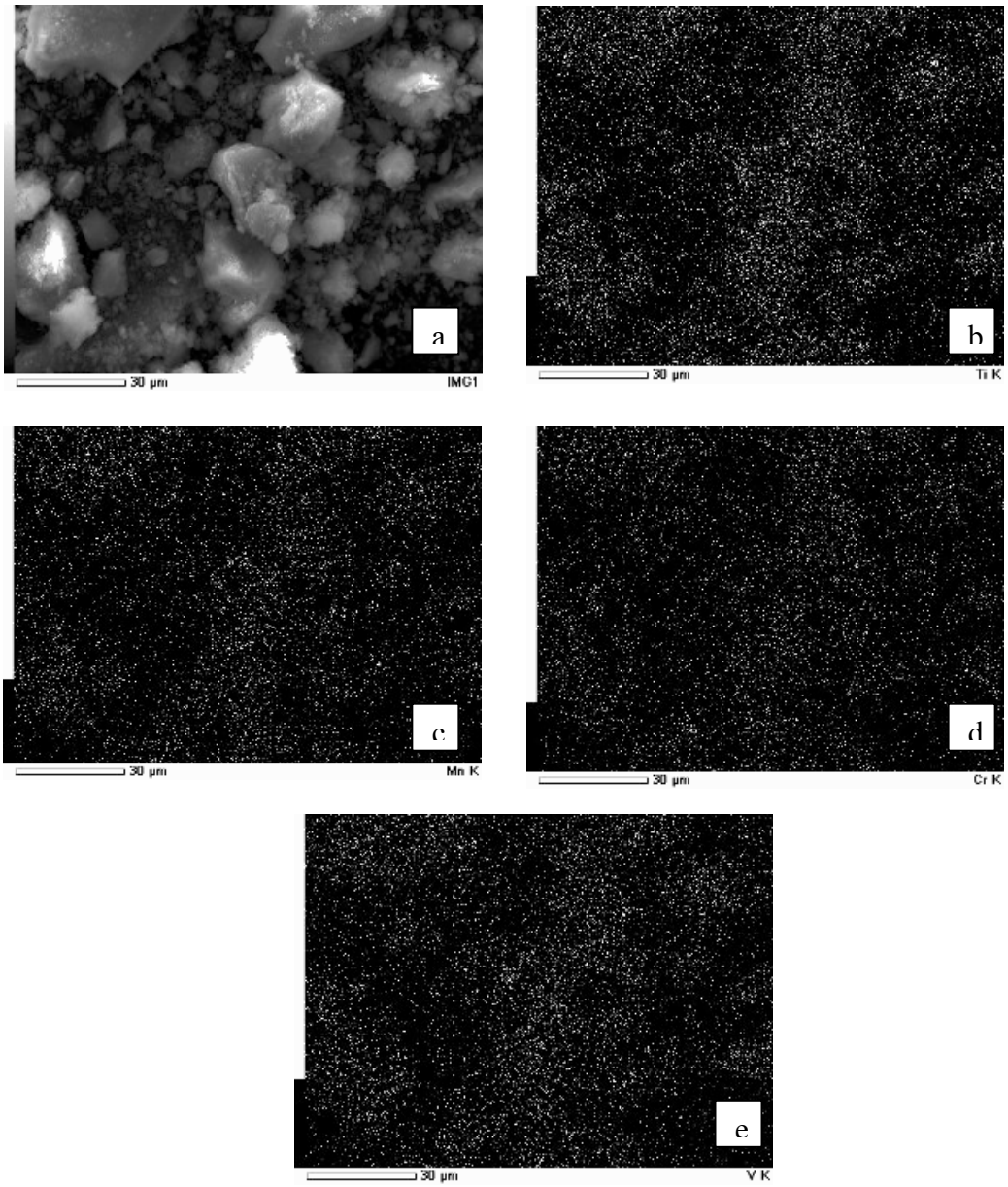

Fig. 6.3. Mapping of the MgH_2-10wt% BCC with BPWR 200: (a) shows a micrograph of the overall area of the sample to be mapped, (b) elemental mapping of Ti, (c) Mn, (d) Cr, and (e) V.

SEM images are shown in Fig. 6.4 for the as-prepared samples. It can be seen that agglomeration is greater for the pure MgH_2 sample than for the samples with the BCC. This might be because the hardness of the BCC particles is higher than that of Mg, and

the BCC can thus break MgH_2 particles into smaller sizes and prevent them from agglomerating. By increasing the BPWR, the agglomeration for the sample becomes less. A smaller particle size and less agglomeration enhance hydrogen storage properties by decreasing the diffusion path of hydrogen atoms [196]

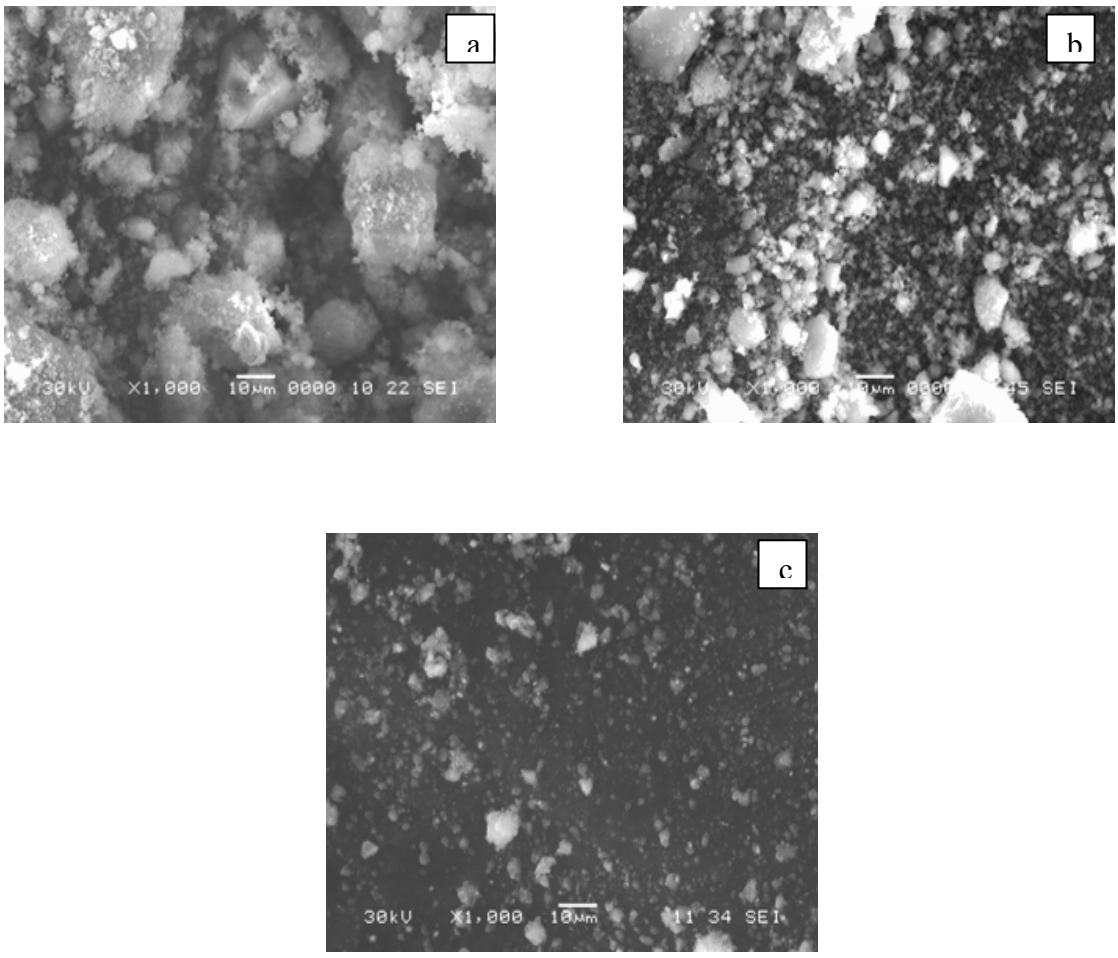

Fig. 6.4. SEM images for the as-prepared samples: (a) pure MgH_2, (b) BPWR 100, (c) BPWR 200.

6.5 Thermal analysis

Thermal properties of samples were investigated using a differential scanning calorimeter (DSC Q100, see 3.4.1.1) with a 50 ml/min argon flow rate and a heating rate of 10 °C/min from room temperature to 430°C. The results for all samples are shown in Fig. 6.5. The onset desorption temperature, T_{onset}, is reduced by doping with BCC. This reduction for the samples with BPWR 100 and 200 is 52°C and 70°C respectively. Also the temperature of desorption, T_{des}, is reduced for the doped samples by 35°C and 50°C compared to the pure sample for the BPWR 100 and 200 samples, respectively.

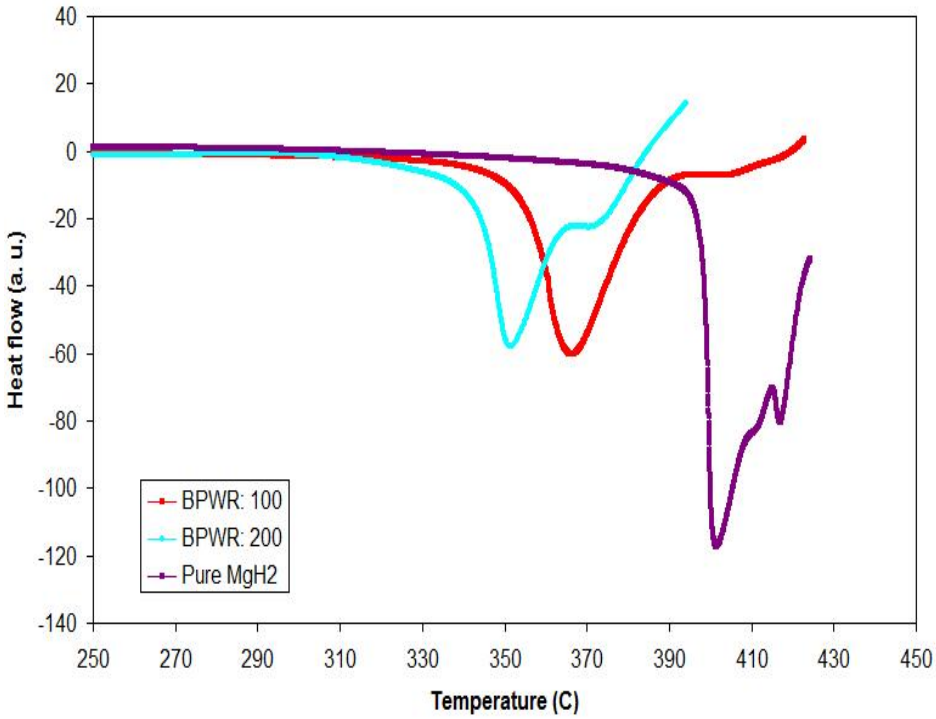

Fig. 6.5. DSC traces for as-prepared samples.

6.6 Hydrogenation and desorption

The hydrogen sorption and pressure-composition isotherm (PCI) behaviour of the samples was studied by Sievert's method at 350°C using an AMC gas reactor controller (see 3.4.2).

6.6.1 Hydrogen Absorption

Hydrogen absorption behaviour of the composites at 350°C and under 30 atm hydrogen pressure is shown in Fig. 6.6. The maximum hydrogen absorbed by pure MgH_2 in this condition is 3.1 wt% while for BPWR 200 and 100 samples it is 4.8 wt% and 4.6 wt%, respectively. The sample with BPWR 200 composite required 60 s to absorb 95% of its maximum capacity, and this time for the sample with BPWR 100 is 65 s which indicates that the absorption kinetics of these samples is much faster than for the pure MgH_2 sample.

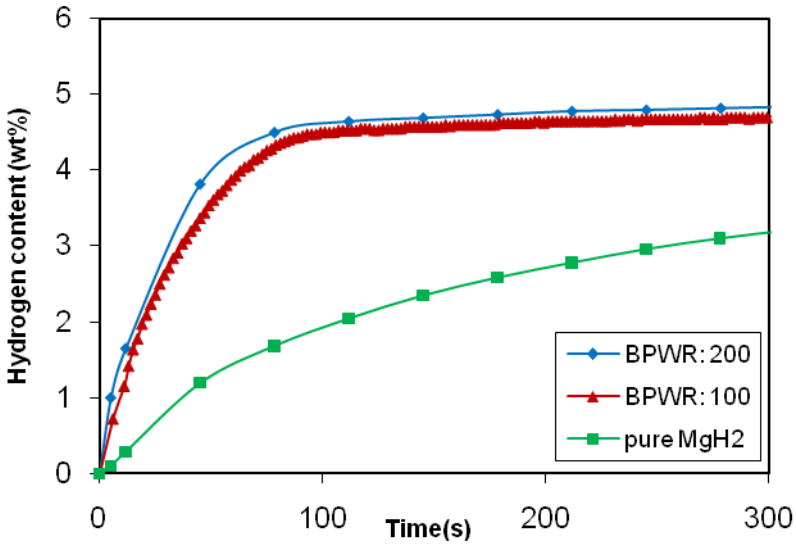

Fig. 6.6. Hydrogen absorption curves for the samples at 350ºC and under 30atm hydrogen pressure.

6.6.2 Hydrogen desorption

The desorption curves of all of the powders under an initial hydrogen pressure of 0.1 atm and at 350 °C are shown in Fig. 6.7. As can be seen from the figure, desorption kinetics for MgH_2-BCC composites has increased significantly. The sample with BPWR 200 shows the optimum desorption kinetics by absorbing ~ 4wt% hydrogen in 300 s.

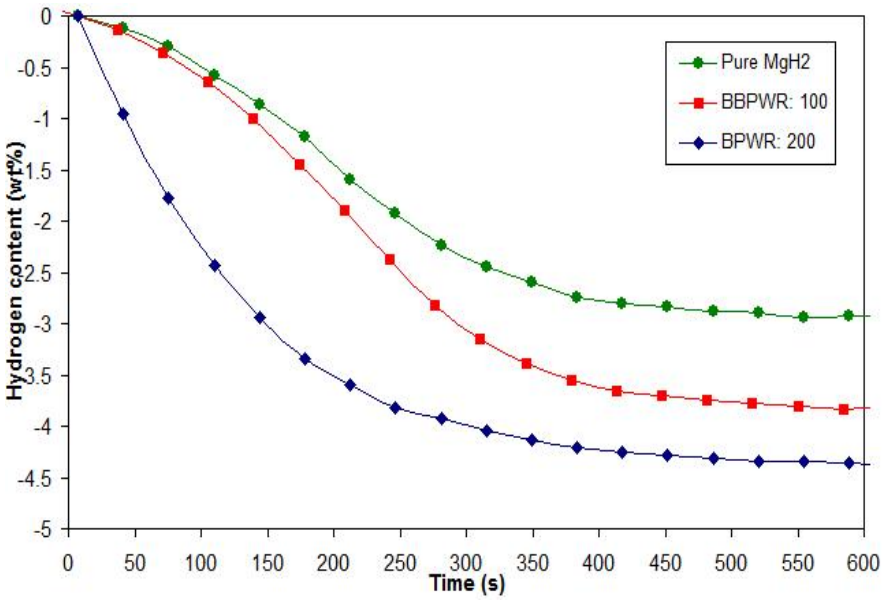

Fig. 6.7. Hydrogen desorption curves for the samples at 350 ºC and under 0.1 atm hydrogen pressure.

These improvements in both absorption and desorption kinetics and capacity might be related to two different effects of the BCC on Mg powder. The first one is a strong catalytic effect of the BCC, which facilitates dissociation of hydrogen molecules to hydrogen atoms by the following reaction at low temperature:

$$(BCC) + \frac{x}{2}H_2 \Rightarrow (BCC)H_x \qquad 7.1$$

The second one is the effect of the hardness of the BCC particles, which breaks MgH_2 particles into smaller sizes and prevents them from agglomerating during ball milling. A

smaller particle size and less agglomeration decrease the diffusion path of hydrogen atoms during both absorption and desorption.

6.6.3 PCI

Fig. 7.8 shows the PCI curves of pure and BPWR 200 samples at 350 °C. It is believed that the plateau pressure is correlated with the unit cell volume of the alloy [202]. If the unit cell volume decreases, the interstitial sites for hydrogen atoms become smaller and the penetration of the hydrogen is more difficult, so the plateau pressure increases [203].

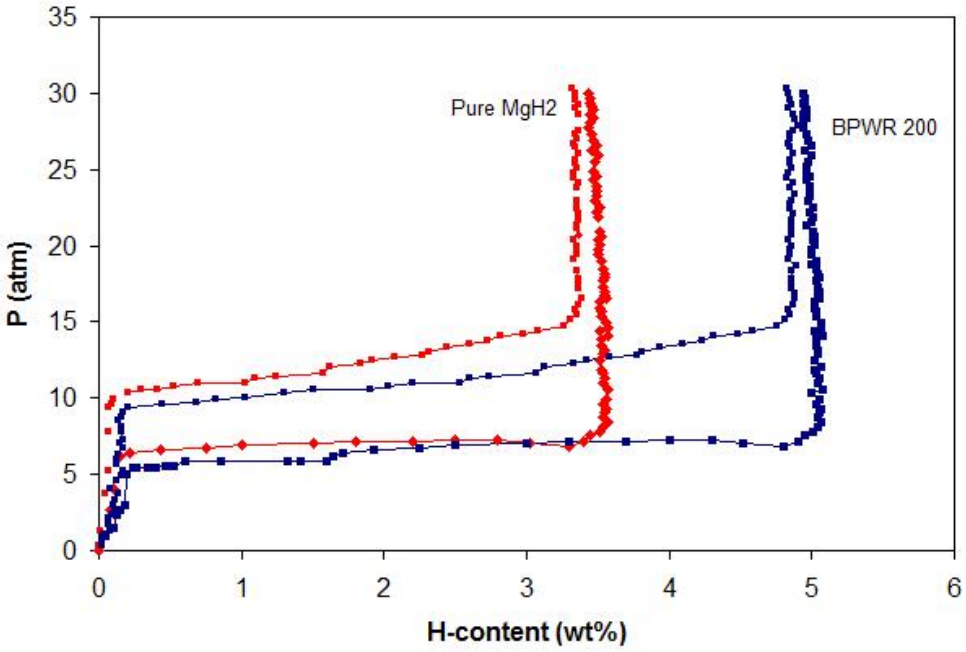

Fig. 6.8. PCI curves of pure MgH_2 and BPWR 200 samples at 350 ºC.

In these samples, the absorption plateau pressure decreases for the doped samples, and therefore the BCC increases the unit cell volume. In addition, there is a difference in hydrogen absorption and desorption equilibrium pressure, called hysteresis. Hysteresis originates because of the presence of transformation strains and disorder during

hydriding and dehydriding [204]. Based on Fig. 8, the hysteresis factors, defined as ln ($P_{desorption}/P_{absorption}$), are 0.47 and 0.56 for the BPWR 200 and pure MgH_2 samples respectively, which indicates that the BCC reduces the hysteresis.

6.8 Conclusion

The effects of the addition of 10wt% BCC ($Ti_{0.4}Mn_{0.22}Cr_{0.1}V_{0.28}$) on the hydrogen storage properties of MgH_2 prepared by ball milling have been investigated. It has been found that the BCC decomposes hydrogen molecules into hydrogen atoms on its surface and absorbs them into the alloy, leading to the formation of BCC hydride. Then, hydrogen diffuses from the BCC in to the Mg particles, resulting in magnesium hydride. Therefore, the BCC acts as a bridge during hydrogenation. In addition, the PCI curves indicates that the BCC increases the unit cell volume of the sample, which helps hydrogen atoms to easily penetrate into and come out of the unit cell, and this increases both the capacity and the absorption/desorption kinetics.

Chapter 7

Effects of BCC alloy with and without CNT on the hydrogen storage properties of MgH_2

7.1 Introduction

In the previous chapter, it was demonstrated that ball milling magnesium with $Ti_{0.4}Mn_{0.22}Cr_{0.1}V_{0.28}$ improved the hydrogen storage properties of the MgH_2. On the other hand, carbon nanotubes (CNTs) exhibited excellent catalytic effects on the hydrogen sorption properties of magnesium based alloys (see 2.7.6.4). A combination of CNTs with transition metals has been found to lead to an especially great enhancement of hydrogen dissociation and diffusion into Mg nanoparticles [205].

In this chapter, the effect of the combination of 10wt% of $Ti_{0.4}Mn_{0.22}Cr_{0.1}V_{0.28}$, hereafter referred to as BCC due to its body centred cubic structure, with a small amount of CNT (5wt%) on the hydrogen storage properties of MgH_2 has been investigated and compared with the performances of pure MgH_2 and MgH_2+10wt% $Ti_{0.4}Mn_{0.22}Cr_{0.1}V_{0.28}$.

7.2 Sample preparation

The BCC alloy sample was prepared by magnetic levitation melting of the constituent metals, all with purity of more than 99.9%. A 50 g ingot was turned over and remelted four times to ensure higher homogeneity, and then it was quenched on a water-cooled rotating molybdenum disc that was spinning at the rate of 20 m/s. After preparation of the BCC, 0.9 g of pure MgH_2 (Sigma-Aldrich, powder H-storage grade) and 0.1 g of

BCC were introduced into stainless steel vials of a QM-3SP2 planetary ball-milling instrument. The samples were ball milled for 24 h with a ball to powder weight ratio of 20 and a speed of 400 rpm. In the last step, the MgH_2+10wt%BCC+5wt%CNT (termed Mg-BCC-CNT) was fabricated by adding 5 wt% multiwall carbon nanotubes (MWCNT, Sigma-Aldrich, > 99.9%) to the ball milling vial with MgH_2+10wt% BCC composite and milling the mixture for 2 h. For comparison, pure MgH_2, and MgH_2 + 5wt% BCC (termed Mg-BCC) samples were also fabricated using the same ball-milling technique. All handling of the powders, before and after ball milling, was performed in an argon filled glove box (with oxygen and water content each below 1 ppm) in order to prevent any oxidation of the samples.

7.3 X-ray diffraction of as-prepared samples

XRD patterns of the as-milled samples, obtained by the GBC-MMA X-Ray Diffractometer (see 3.3.1), are shown in Fig. 7.1. The main peaks match β-MgH_2 (JCPDS-12-0697), but there are small peaks corresponding to γ-MgH_2 (JCPDS 351184), the BCC, MgO, and even Mg. The presence of the orthorhombic γ-phase is a result of alteration in the microstructure because of the ball milling [206]. Despite the low quantity of the BCC in the composite, its phase could be observed and is in agreement with Reference [181]. However, there are no peaks which indicate formation of any new alloy phase as a result of reaction between MgH_2 and the BCC. The existence of the weak Mg peak indicates that the commercial magnesium hydride was partially dehydrogenated during ball milling. Diffraction peaks of the composites are considerably broadened as a consequence of reduction of particle size, as well as the increase in defects and the mechanical strains created within the lattice by the ball milling [201].

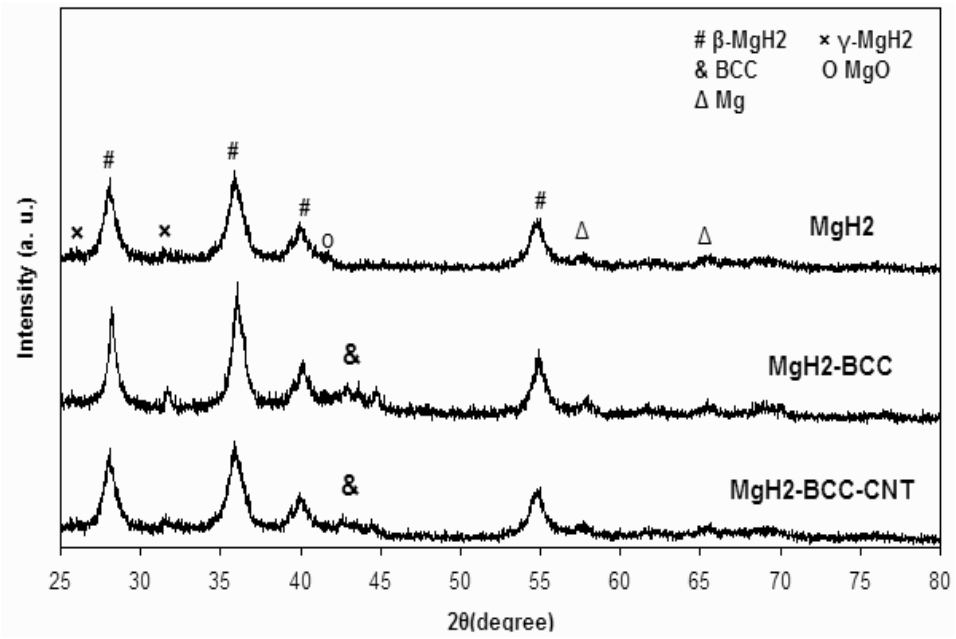

Fig. 7.1. XRD patterns for as-milled samples.

7.4 Morphology

Fig. 7.2 shows the morphology of the composites and the distribution of the elements which are characterized by using scanning electron microscopy (see 3.3.3). It can be explicitly seen that the particle size of the sample with BCC (Fig. 7.2(b)) is smaller than that of pure MgH_2 (Fig. 7.2(a)), while the MgH_2-BCC-CNT (Fig. 7.2(c)) has a particle size that is much smaller than in either of the others. In addition, agglomeration is lower for the samples with CNT than in the samples without CNT.

To monitor the dispersion of the BCC particles, EDS was conducted, and a backscattered electron composition (BEC) image of the Mg-BCC sample with the EDS element analysis are shown in Fig. 7.3. The larger gray particles are MgH_2, and the white particles are the BCC.

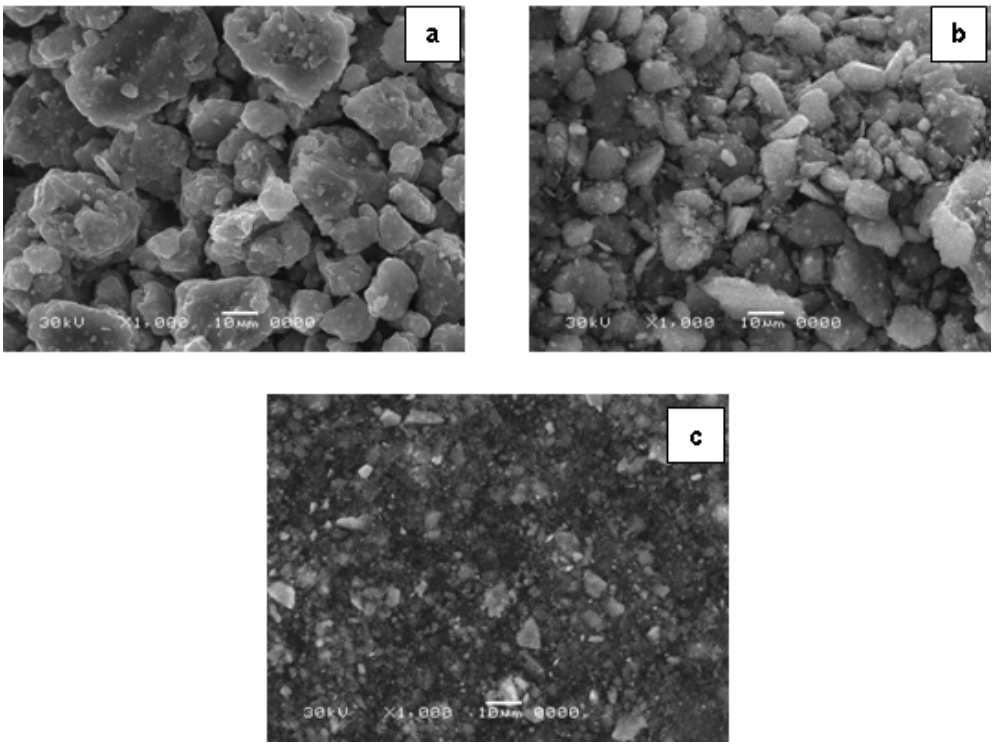

Fig. 7.2. SEM images of all samples: a) pure MgH_2, b) Mg-BCC, c) Mg-BCC-CNT.

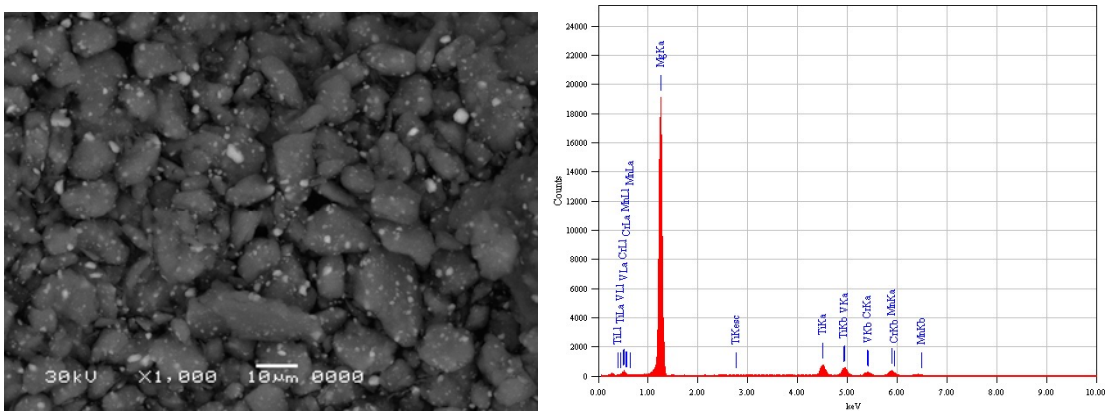

Fig. 7.3. Backscattered electron composition (BEC) image of the Mg-BCC sample (left and its EDS element analysis (right).

It can be clearly observed that the BCC particles are distributed uniformly among the MgH_2 particles. Although the BCC is on the surface of the MgH_2 particles, based on the BEC image, it is expected that they are in the interior of the particles as well, due to the

24 h of high-speed ball milling. Therefore, based on the morphology, it is predictable that the hydrogen sorption properties of the samples with the BCC and CNT will be improved as a result of a clearly smaller particle size, less agglomeration, and homogeneous dispersion of the catalysts among the MgH_2.

7.5 Desorption temperature

The desorption temperature and hydrogen capacity of the as-prepared composites were determined by using an AMC gas reactor controller (see 3.4.2) in profile release mode, in which the samples were heated up from room temperature to a maximum of 500 °C with a heating rate of 10 °C/min and a pressure of 1 atm. Both the desorption temperature, T_{des}, and the hydrogen content were measured and graphed using the software package supplied with the instrument as shown in Fig. 7.4. Before the measurement, the sample holder was evacuated at room temperature for 30 min.

Based on the graphs, T_{des} for both doped sample was reduced significantly. The onset temperature of hydrogen release, T_{onset}, for the pure sample is 350 °C, while for the MgH_2-BCC and MgH_2-BCC-CNT samples, T_{onset} is 280 °C and 245 °C, respectively. T_{des} was reduced by 125 °C and 66 °C for the MgH_2-BCC-CNT and MgH_2-BCC samples, respectively, in comparison with the pure MgH_2. In addition the differences between T_{des} and T_{onset} show that hydrogen release from the sample including CNT was much easier. The hydrogen contents for all samples are almost the same (~ 6 wt %), and the very small difference between them could be related to error of the instrument.

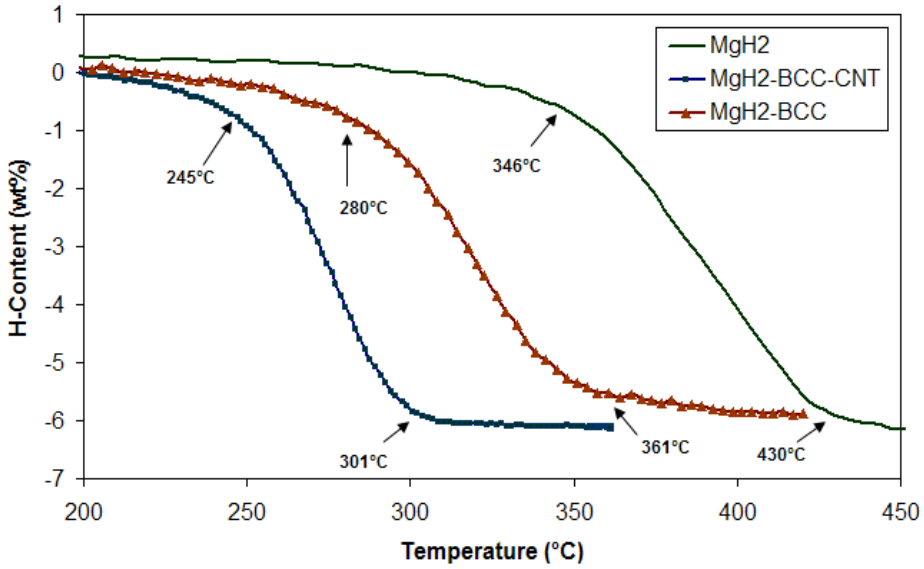

Fig. 7.4. Initial hydrogen release of all as-prepared samples in profile release mode.

7.6 Hydriding and dehydriding

After dehydrogenation under profile mode and for each sample, the temperature of the sample holder was set at 300 °C (and then 250 °C), and the sample chamber was evacuated for 1 h to remove any remaining hydrogen desorbed by the sample and to fix the temperature. Then, the hydriding/dehydriding kinetics were studied at these temperatures at a hydrogen pressure of 30 atm and 0.1 atm, respectively.

7.6.1 Hydrogen absorption and desorption at 300 °C

The absorption kinetics results at 300 °C (shown in Fig. 7.5) indicate that both doped samples absorbed hydrogen more rapidly than the pure one and that MgH_2-BCC-CNT has the fastest absorption rate. It soaks up 90% of its maximum absorbed hydrogen (H_{max}) in 150 s while the times for MgH_2-BCC and pure MgH_2 are 195 s and 1680 s, respectively. Also, note that H_{max} has increased as a result of the addition of the BCC and BCC-CNT. The desorption kinetic curves at 300 °C (Fig 7.6) illustrate that 90% of

H_{max} release occurs at 500 s, 179 s, and 93 s for pure MgH_2, MgH_2-BCC, and MgH_2-BCC–CNT, respectively.

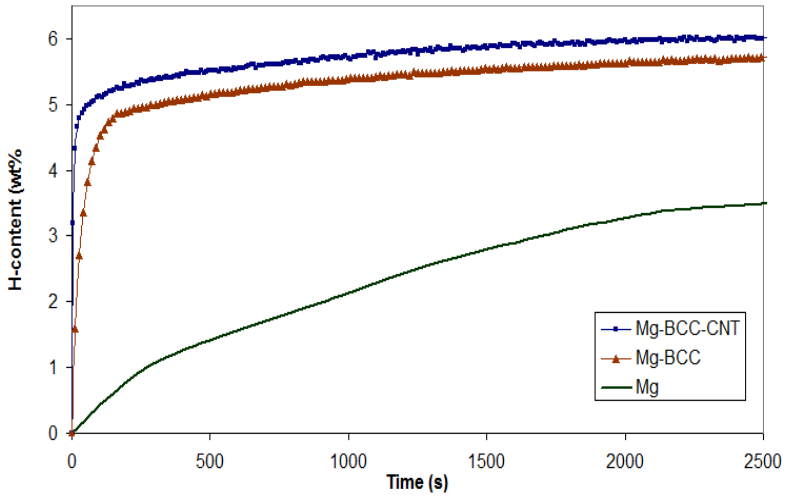

Fig. 7.5. Hydrogen absorption of the samples at 300 °C and 30 atm.

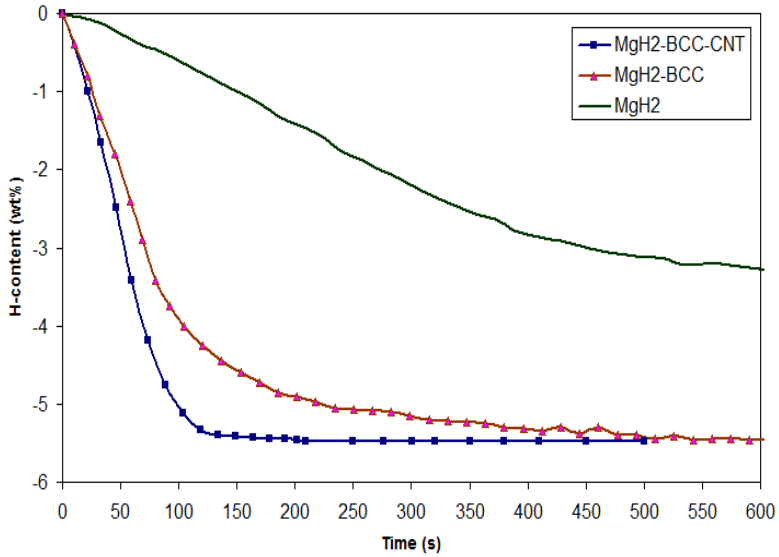

Fig. 7.6. Hydrogen desorption at 300 °C and 0.1 atm for all samples.

7.6.2 Hydrogen absorption and desorption at 250 °C

Fig. 7.7 and 7.8 present the corresponding hydrogen absorption and desorption kinetics at 250 °C. All samples absorb and release hydrogen more slowly at lower temperature,

and the hydrogen storage capacity decreases as well. However, these reductions are very minor for the doped samples, particularly for the MgH_2-BCC-CNT, as it absorbs more than 5 wt% hydrogen in ~500 s and releases it in less than 800 s.

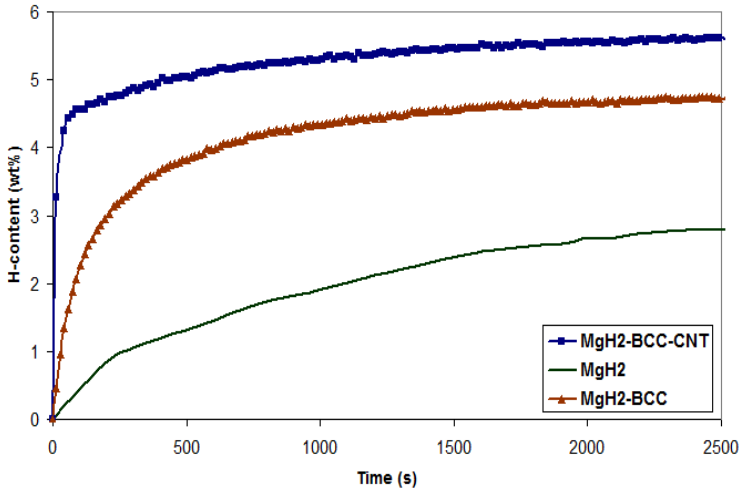

Fig. 7.7 Hydrogen absorption at 250 °C and 30 atm.

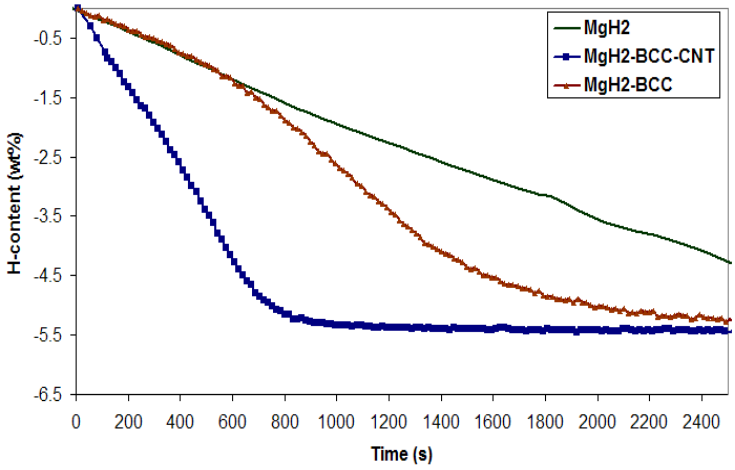

Fig. 7.8. Hydrogen desorption at 250 °C and 0.1 atm for all samples.

7.7 XRD after dehydrogenation

Fig. 7.9 shows the XRD patterns for the dehydrogenated samples. It can be observed that the major phase after dehydrogenation is magnesium, however, there are peaks

corresponding to the BCC and MgO which overlap in the MgH_2-BCC pattern. Although all the sample handling was done in an argon filled glove box, oxidation due to periodic opening of the milling jar and the AMC sample holder in the glove box could be the reason for the appearance of MgO phase. The peaks became sharper for the dehydrided samples, which indicates a reduction in defects and mechanical strain through hydriding/dehydriding processes. In addition, there is a slight shift in the peaks (as is shown in the Fig. 7.9 inset for the most intense peak), indicating extra enlargement in the lattice parameters of the unit cells for both MgH_2-BCC and MgH_2-BCC-CNT composites.

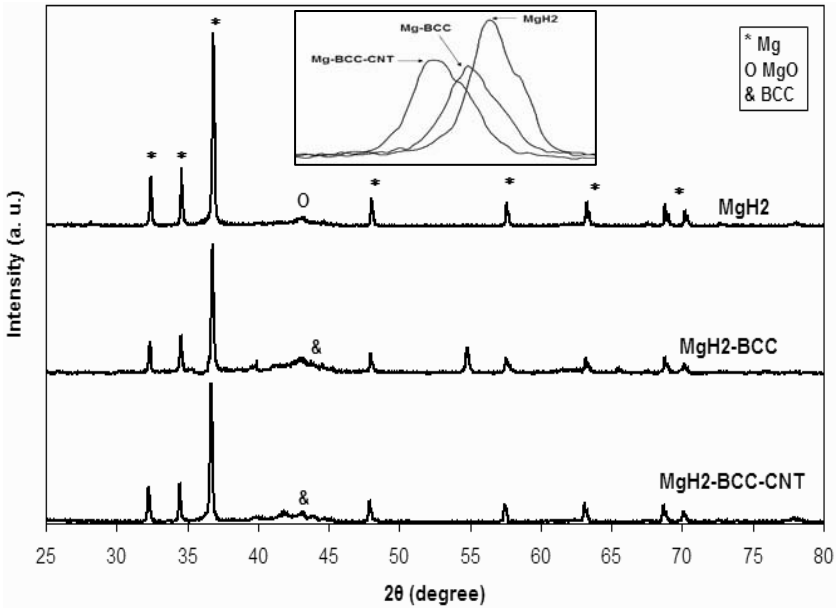

Fig. 7.9. XRD patterns for the samples after dehydrogenation. The enlarged area in the inset shows the shift of the peak with highest intensity.

7.8 Discussion

The results demonstrate that 1) the BCC improves the hydriding/dehydryding kinetics and maximum hydrogen capacity, 2) the Mg-BCC-CNT system shows superior

hydrogen storage properties, and so 3) the BCC and CNT have synergistic effects on all aspects of hydrogen sorption properties. On the other hand, the hydriding and dehydriding mechanisms could be the keys to insight into the reasons for these special effects. It is accepted both theoretically [207] and experimentally [205] that: 1) dissociation of H_2 molecules into H-atoms on the surface of the magnesium, 2) diffusion of H-atoms along the grain boundaries, and 3) absorption/desorption of the *catalyst* and transformation of H and Mg atoms into MgH_2 molecules at catalyst/Mg interfaces, are the three critical steps of the hydrogenation process. The energy barrier for H_2 dissociation of pure MgH_2 is 1.15 eV [207], which means that more than 400 °C is required for dissociation, although this amount of energy will decrease in the presence of a catalyst. For example, it is 0.201 eV and 0.103 eV for V and Ti, respectively [208]. Although further investigation seems to be necessary to find the exact energy barrier for H_2 dissociation on the BCC surface, as it is a composite of transition metals, the barrier could be very low. Therefore, the main catalytic effect of the BBC could be dissociation of hydrogen molecules at low temperature and improvement of the first step of the hydrogenation mechanism.

In addition, as described in our previous chapter and other references [181, 182, 209], the BCC can absorb the H-atoms at low temperature to form BCC hydride by the following interaction:

$$(BCC) + \frac{x}{2}H_2 \Rightarrow (BCC)H_x \qquad (1)$$

The BCC hydride then releasing hydrogen at the Mg/BCC interfaces. Therefore, the second effect of the BCC alloy is to work as an atomic hydrogen bridge which facilitates the transformation of H atoms and so, improves the 3rd step of the hydrogenation process.

On the other hand, because the outer regions of the Mg particles and their grain boundaries are completely hydrogenated, the centres of grains may be unreachable for hydrogen atoms. After a 2 h ball milling, CNTs retain their nanotube structure, and they aggregate along the grain boundaries of magnesium particles [208], so they may facilitate access of H-atoms to the magnesium grains, which increases both the absorption kinetics and the hydrogen storage capacity. Therefore, for the MgH_2-BCC-CNT sample, the effect of the CNTs is enhancement of the 2nd step by improvement of the diffusion path of H-atoms along the grain boundaries.

The desorption mechanism is the reverse process to the absorption. The H-atoms interact with the BCC to form "BCC hydride" on the magnesium particle surfaces. In addition, CNTs (for the MgH_2-BCC-CNT sample) facilitate the emergence of hydrogen from the grain boundaries. Finally, the BCC recombines the H-atoms into hydrogen molecules, with a resulting improvement in the dehydriding kinetics and desorption temperature.

7.9 Conclusion

The effects of the addition of 10wt% BCC ($Ti_{0.4}Mn_{0.22}Cr_{0.1}V_{0.28}$) with and without CNTs on the hydrogen storage properties of MgH_2 were investigated. The results showed that homogeneously distributed catalysts significantly improve the desorption temperature, the maximum absorbed hydrogen and the hydriding/dehydriding kinetics. The effects of the BCC on the hydrogenation could be reduction of the barrier energy for dissociation of hydrogen molecules into hydrogen atoms and also promotion of hydrogen pumping into the Mg/BCC interfaces, while CNTs (for the MgH_2-BCC-CNT

sample) facilitate access of H-atoms to the interior of Mg grains. Furthermore, during dehydrogenation, the “BCC hydride” forms on the Mg/BCC interfaces, and then the BCC releases H-atoms more rapidly than Mg, while it also facilitates the recombination of H-atoms into H_2 molecules. CNTs facilitate the emergence of hydrogen from the grain boundaries during desorption.

Chapter 8

A multi-scale production approach for Mg hydrogen storage alloys

8.1 Introduction

It is reported that the *as-cast* eutectic Mg- Mg_2Ni can provide necessary interfaces for hydrogen diffusion into Mg layers. For example, Reilly and Wiswall [210] have reported that Mg_2Ni in the Mg-Ni system interacts readily with hydrogen and thereby catalyses the hydride formation of MgH_2. Cermak et al. [211] reported that eutectic Mg-Mg_2Ni provides interphase boundaries where hydrogen diffusion can take place with high diffusivity, followed by penetration into the Mg phase. On the other hand, as it described in previous chapters and section 2.7.5 the effects of ball milling, such as breaking the surface oxide layers and producing more surface area and active sites [138], and a large area of grain boundaries [212], leads to reduced diffusion paths through which hydrogen can be dissolved into Mg particles. Moreover, transferring hydrogen atoms into the interior layers of Mg is one of the most important effects of a catalyst, and this could be possible by placement of the catalyst particles in deeper layers of Mg particles, which ball milling *after* casting may facilitate. Therefore, fabricating *Mg + Ni* by casting, ball-milling, and the combination of casting and ball milling are worth considering in investigating the important role of processing in hydrogen sorption properties. For these purposes, in this chapter, various fabrication methods, such as casting, ball-milling and the combination of casting and ball milling, and their influence on the hydrogen sorption properties of Mg-6 wt% Ni alloys are

discussed. By understanding the interrelationship between microstructure and hydrogen sorption properties, we aim to find optimised fabrication conditions for the Mg-Ni system.

8.2 Sample preparation

Mg-6 wt% Ni base alloy with an average mass of 1 kg was melted in a steel crucible in an electric resistance furnace at 760 °C under covering gas (CO + SF_6) atmosphere. Commercial purity magnesium (99.8%) and nickel (99.8%) were used for the alloying. Chips of the alloy were prepared by drilling the cast ingot. Then, the obtained chips were ball milled by using two different ball-milling instruments: the first one was a QM-3SP2 planetary ball-milling instrument, in which samples were ball milled for 60 h at 400 rpm with a ball to powder weight ratio of 20:1, and under argon atmosphere. At the end of this time, 5wt% multi-wall carbon nanotubes (MWCNTs) were added to the sample and ball milled for 2 h. The second one was a Magnetic Uni-Ball-Mmill 5, in which samples were ball milled under hydrogen atmosphere with an initial pressure of 700 kPa in impact mode [191] at 15 rpm for 60 h. The reason for the addition of the CNTs was to speed up the activation process, which is explained completely in some reports [213, 214][187].

Another sample was prepared for comparison: ball-milled Mg + 6wt%Ni powder was prepared by the QM-3SP2 planetary ball-milling instrument under the same conditions as the ball-milled-cast sample. For this sample, 5wt% MWCNT was added at the end of the procedure, and the mixture was ball milled for 2 h. All sample handling was carried out in a purified Ar-filled glove box with a level of water/oxygen below 1 ppm. Table 1 gives brief information on all the prepared samples.

Table 1. Brief details on the fabricated samples with the code used.

Sample	Preparation Method	Code
As-cast Mg- 6wt% Ni alloy	Melting and casting process	Cast
Mg- 6wt%Ni (as-cast) + 5wt% CNT	Planetary Ball-milling	BM-cast
Mg-6wt%Ni (as-cast) + 5wt% CNT	Uni-ball-mill 5	UniBM-cast
Pure Mg+6wt% Ni + 5wt% CNT powder	Planetary Ball-milling	BM-powder

8.3 X-ray patterns

Figure 8.1 shows the XRD patterns of the as-prepared samples of the cast, BM-cast, and BM-powder obtained by a GBC-MMA X-Ray diffractometer (see 3.3.1). As the uniBM-cast sample is already hydride, its XRD pattern is compared with hydride samples later in Fig. 8.7.

The main peaks in these samples are Mg. For the cast and BM-cast samples, there are some peaks related to Mg_2Ni, although these peaks, in the same way as the others, are broadened in the BM-cast sample as a consequence of ball milling. However, while there are some peaks of Ni in the as-prepared BM-powder sample, there are no peaks of Mg_2Ni in its pattern, indicating that Mg and Ni did not have enough reaction time during ball milling. There is a slight shift in the peak positions in the ball-milled samples, which indicates an expansion in the crystal structure in comparison with the cast sample. There is no diffraction peak for CNTs in any of the samples both because the content was low and because of the possibility of disruption of its structure during ball milling. However, there is a peak for MgO in the BM-powder which is a result of oxidation of this sample during preparation.

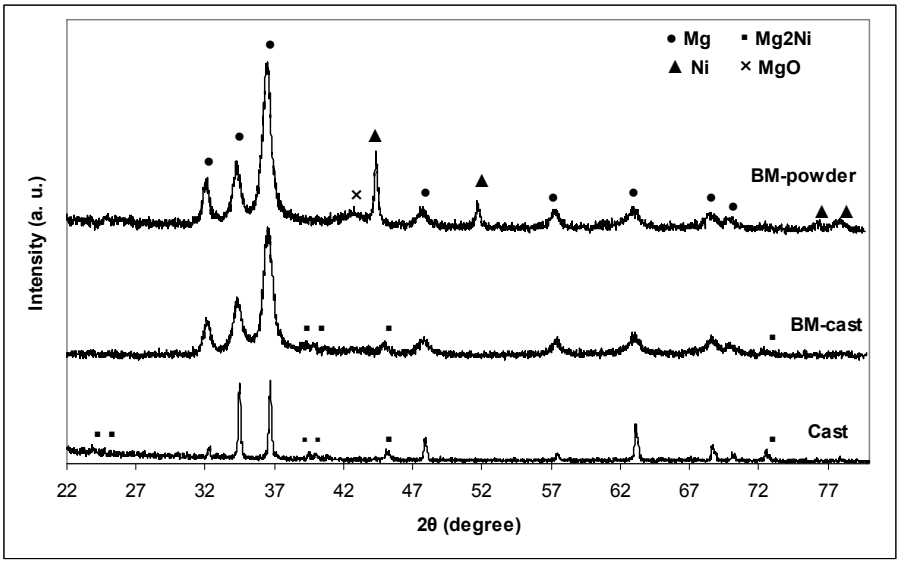

Fig. 8.1. XRD patterns of as-prepared samples.

8.4. Morphology

The morphology of the samples was investigated by scanning electron microscopy (see 3.3.3), and the obtained images are shown in Fig. 8.2. The cast sample (Fig 8.2(a)) consists of a eutectic mixture of Mg-Mg_2Ni in an α-Mg matrix, as reported by Aminorroaya et al. [214]. However, ball milling of the cast sample breaks the chips into powder particles in a size range from a few hundreds nanometres to a few tens of microns (Fig. 8.2(c)). BM-powder, as shown in Fig 8.2(d) has particles of a similar size to the BM-cast. Fig 8.2(b) shows an image of the uniBM-cast sample. The eutectic structure is completely disturbed, and the particle size and agglomeration of its particles are also lower than in BM-cast and BM-powder samples. This could be because of the hydrogenation and lubricant effects of CNTs during hydrogenation. A backscattered electron composite image (BEC) of the BM-cast sample is shown in Fig. 8.3. In this figure, the bright particles are Mg_2Ni, which are distributed uniformly among the Mg particles.

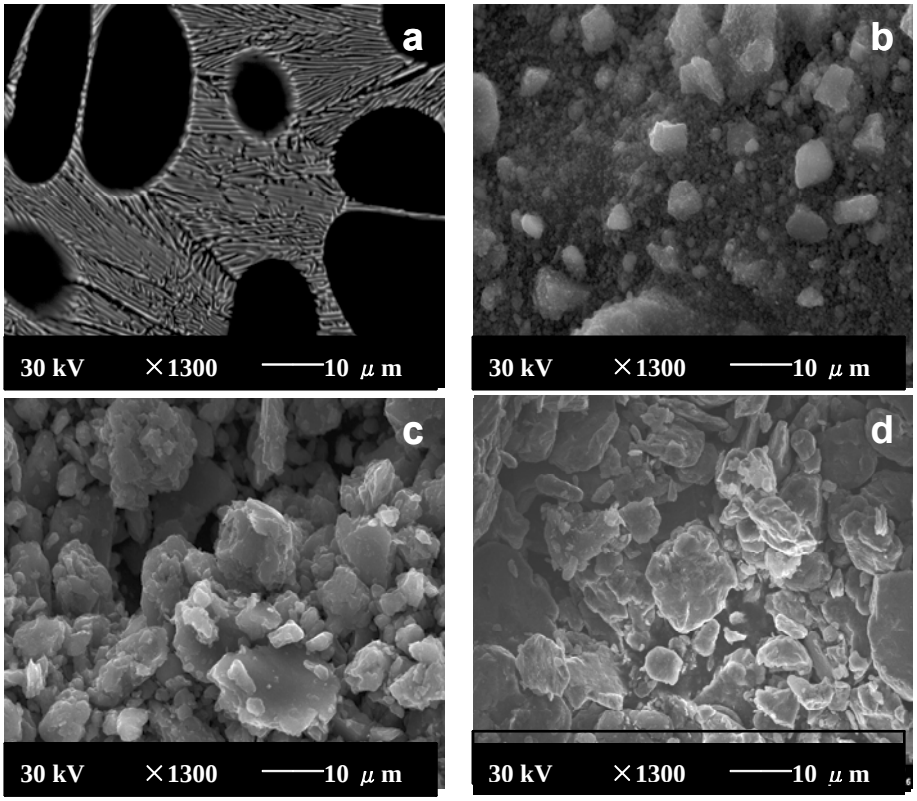

Fig. 8.2. SEM images of all samples: a) cast, b) uniBM-cast, c) BM-powder and d) BM-cast.

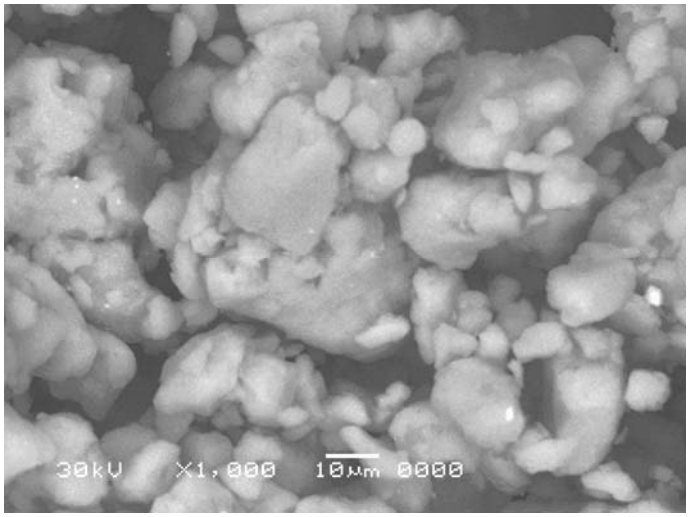

Fig. 8.3. Backscattered electron composition (BEC) image of the BM-cast sample. Bright particles are Mg_2Ni.

8.5 Hydriding and dehydriding

The hydrogen absorption/desorption behaviour were evaluated by the Sieverts method at 250 °C and 200 °C, using an AMC Gas Reactor Controller (see 3.4.2).

8.5.1 Hydrogen Absorption

Figure 8.4 demonstrates the hydrogen absorption at 250 °C under a hydrogen pressure of 20 atm. All ball-milled samples exhibit superior absorption properties under these conditions in comparison with the cast sample. The maximum hydrogen capacity (H_{max}) for the BM-powder and BM-cast samples is approximately 5 wt%, approaching 80% of H_{max} within 11 s and 40 s respectively. H_{max} for the uniBM-cast is about 4.6 wt%, with 80% of hydrogenation of the sample complete in almost 45 s. The cast sample could absorb only 1.6 wt% hydrogen after 300 s exposure to hydrogen under the same conditions, but its maximum capacity after 30 min. is ~2.8 wt%.

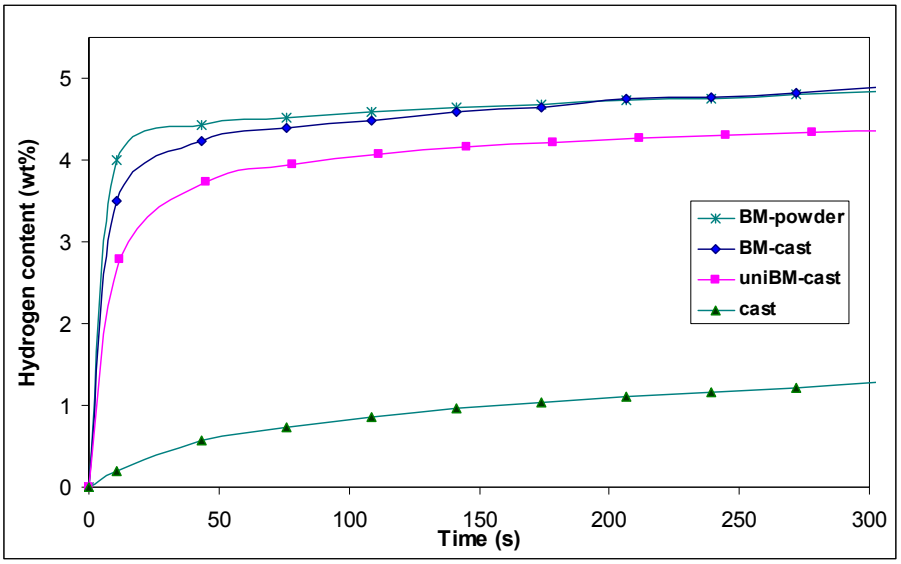

Fig. 8.4. Hydrogen absorption at 250 °C and 20 atm.

The hydriding behaviours of the samples at 200 °C (Fig. 8.5) are almost the same as at 250 °C, allowing for the slightly slower kinetics for all samples, which is normal because of the lower temperature. The BM-powder, uniBM-cast, and BM-cast samples absorb 80% of their maximum hydrogen capacities in ~43 s, ~75 s and ~78 s, respectively.

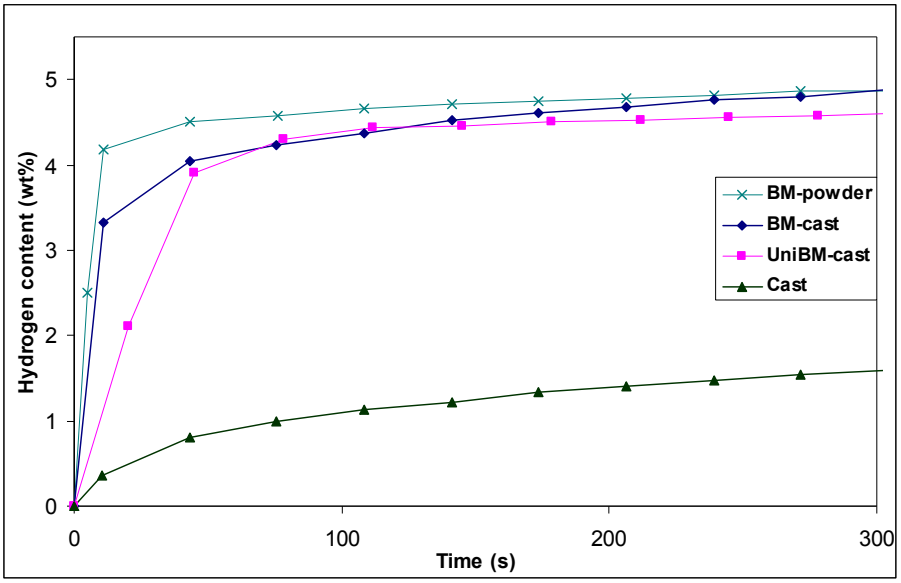

Fig. 8.5. Hydrogen absorption at 200 °C and 20 atm.

The hydrogen absorption behaviour of the samples indicates that ball milling is a better method to improve the kinetics. Hydrogen absorption, generally, is much more dependent on the nucleation and growth of the hydride, which is MgH_2 in this case. It is well known that defects and more active surface area facilitate the nucleation, and the best known method for introducing defects and active sites is ball milling. However, ball-milled samples do not show any considerable differences in hydrogen absorption behaviour, with or without prior casting.

8.5.2 Hydrogen Desorption

Hydrogen desorption of all samples at 250 °C and under 0.1 atm hydrogen pressure is shown in Fig. 8.6. The first result from the figure is that the desorption rate under these conditions is slower than the absorption rate, which is in agreement with our results in previous chapters and other reports [215]. Secondly, the cast sample releases 80% of its H_{max} in ~1100 s, and this amount for the BM-powder, which has the fastest desorption kinetic, is released in 1078 s. The BM-cast and uniBM-cast samples show lower rates, which are ~1220 s and ~1400 s, respectively. Therefore, the desorption kinetics for the samples are very similar. This could be another result of introducing defects and active sites during ball milling. The third result based on this figure is that the released hydrogen for all of the samples is lower than their absorbed hydrogen, which indicates that a small amount of hydrogen remains in the composites at this temperature, even after 100 min. None of the composites showed any desorption at 200 °C, even after 2 h.

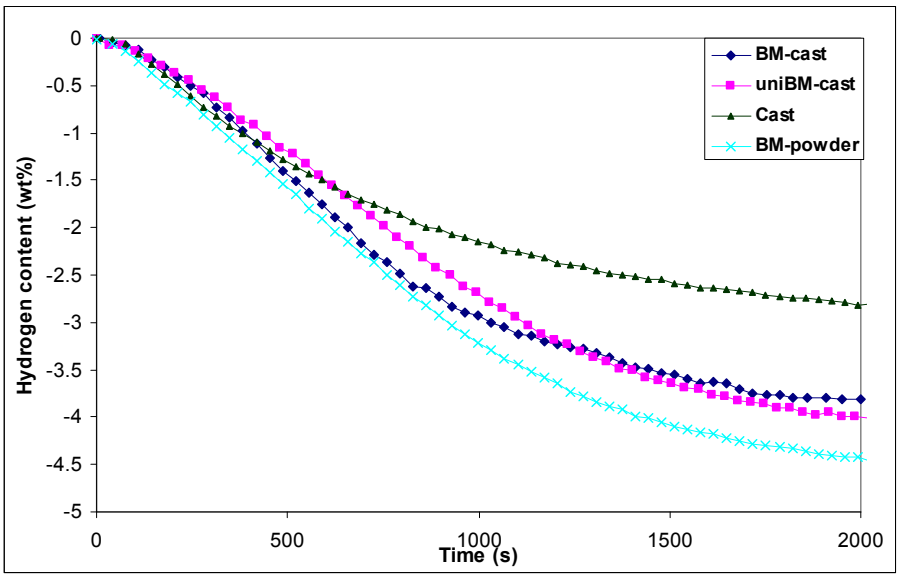

Fig. 8.6. Hydrogen desorption at 250 °C and 0.1 atm.

8.6 XRD of hydrogenated samples

Fig. 8.7 shows the XRD patterns of the samples after hydrogenation and for the as-prepared uniBM-cast sample. The main peaks for all samples here are β-MgH_2, however, there some peaks corresponding to Mg_2NiH_4, γ-MgH_2, MgO, and Mg_2NiO_2. The peaks of Mg_2NiH_4 indicate that Mg_2Ni phase has turned into its hydride phase under these conditions (250 °C and 20 atm), despite its low content in the samples. Also, all peaks in the uniBM-cast sample are much more broadened than in the other samples, which is a result of the ball milling with larger balls and impact mode, in which the balls drop onto the sample from the highest point of the jar [14]. However, this peak broadening appears too wide at 2θ = ~36° in comparison with the other peaks. This could be a result of the overlapping of two peaks: a β-MgH_2 peak at 2θ = 35.9° and a Mg_2NiH_4 peak at 2θ = 36.8°.

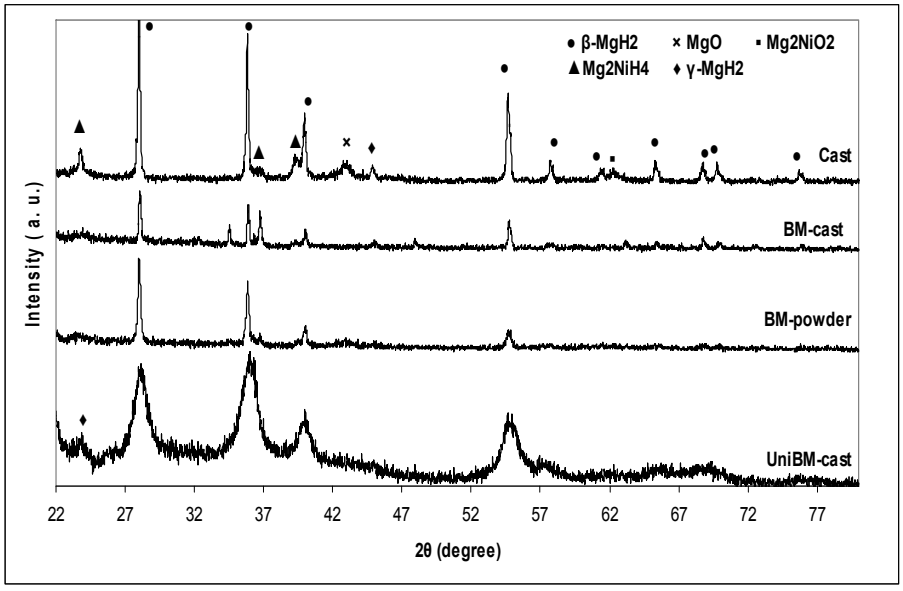

Fig. 8.7. XRD patterns of all samples after hydrogenation.

As can be seen from Fig. 1, there are some peaks related to Ni in the BM-powder pattern, while there is no peak related to Mg_2Ni before hydrogenation. However, after hydrogenation of this sample, there are no peaks of Ni particles in the XRD patterns, while there are some peaks corresponding to Mg_2NiH_4. It seems that Ni particles, which are agglomerated with Mg particles during ball milling, are turned to Mg_2Ni under the absorption conditions and help the sorption kinetics of the sample. In spite of handling the samples in the glove box, there are two peaks corresponding to two oxide phases: MgO and Mg_2NiO_2 in the cast and BM-cast samples.

8.7. Desorption Temperature

Fig 8.8 shows the DSC traces for all samples with a heating rate of 10 °C/min. All ball-milled composites show a lower onset and desorption temperature compared with the cast sample. The onset desorption temperature (T_{onset}) for the BM-powder sample is 50 °C, lower than for the cast one. In addition, the BM-cast and uniBM-cast show 30 °C and 45 °C reduction in T_{onset} in comparison with the cast sample, respectively. The BM-cast and BM-powder samples have 2 peaks in their DSC traces, while the cast and the uniBM-cast show one peak, which is much broadened. It seems there were two peaks for these two samples as well, but their peaks overlapped, resulting in one broadened peak.

There are two reasons for this phenomenon. Firstly, Mg_2Ni absorbs hydrogen and is converted to Mg_2NiH_4, which releases hydrogen at lower temperature than pure MgH_2 [158]. However, as MgH_2 and Mg_2NiH_4 are attached to each other either in the cast or ball milled samples, they can not release their hydrogen separately and without any effects on each other. Secondly, all samples have both γ and β phases of MgH_2 in their

compositions, and the γ-phase decomposes before the β-phase (see 2.7.3). Therefore, the DSC behaviour could be a combination of these two reasons. In the first step, γ-MgH_2 and Mg_2NiH_4 release their hydrogen, which is followed by a contraction in the volume of these particles. Both of these decomposition behaviours are attributed to the development of elastic strains, which act as external forces for β-MgH_2 decomposition, so that a part of this phase becomes dehydrided. However, β-phase particles still remain in the sample to decompose in the second step, as shown in the DSC traces.

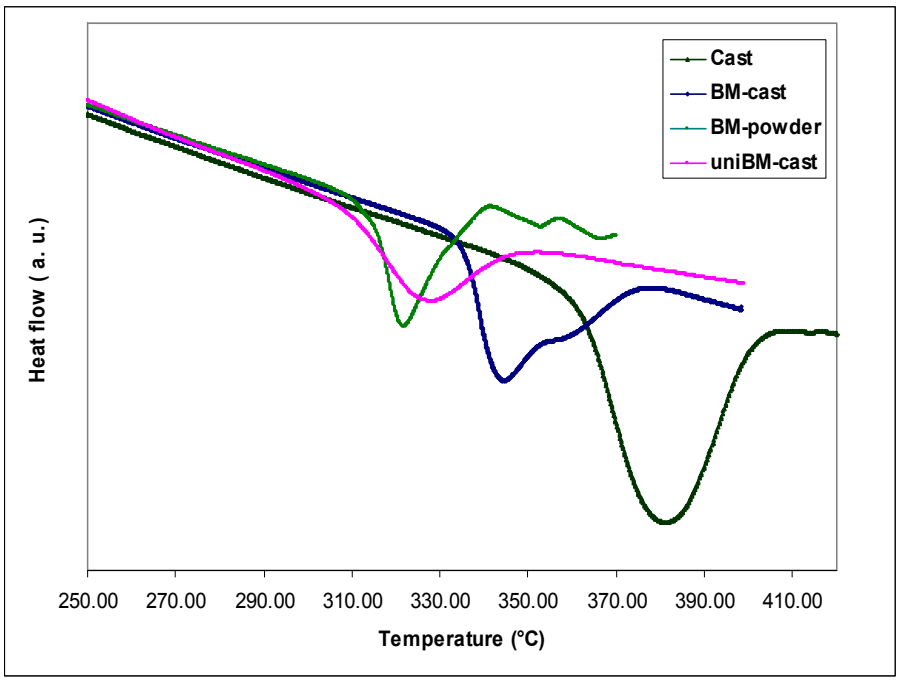

Fig 8.8. DSC traces for all samples after hydrogenation.

Conclusion

In this chapter, a comparison between the hydrogen storage properties of Mg + 6wt%Ni in three states, cast, ball-milled-cast (by either planetary or magnetic Uni-Ball-Mill), and ball-milled-powder has been studied, with multi-walled carbon nanotubes added to the ball-milled samples to speed up the activation. The results indicated that preparation

of *Mg+ catalysts* by ball milling leads to remarkable hydrogen sorption properties in comparison with casting, as a consequence of introducing defects and active sites during ball milling. However, because the preparation by casting is a cheap method, ball milling of the cast material would be cheaper than ball milling of fine Mg nanopowder.

Chapter 9

Summary and Conclusion

Magnesium is one of the promising candidates for hydrogen storage because of its high storage capacity, good reversibility and low cost. However, the high desorption temperature and poor sorption kinetics limited its practical applications particularly for on-board purposes. The main objective of the present study is improvement of hydrogen storage properties of MgH_2. For this purpose, Mg and/or MgH_2 powders are doped with different kinds of additives, mainly through ball milling, and the experiments and results have been described in previous chapters. In this chapter, a brief of the works and founded results is summarized.

10.1 MgH_2-SiC composites

1. As ball-milling is a method for improvement of surface area, an additive with high hardness may act as nano-balls during ball milling and causes additional improvements in surface area of MgH_2. Therefore, pure MgH_2 and MgH_2+x wt% SiC (x= 2, 5, 10, 20) were prepared by magnetic uni-ball-mill and their experimental results were compared.

2. The hardness of SiC reduces the grain size, increases the surface area and preventes the agglomeration of MgH_2 particles during ball milling. These effects result in the reduction of desorption temperature for all samples including SiC. Up to 5wt% SiC doping increases hydrogen storage capacity and improves both absorption and desorption kinetics and also reduces the hysteresis.

3. Increasing the amount of SiC to more than 5wt% introduces negative effects such as poor kinetics, lower capacity and higher hysteresis. As SiC is not a catalyst, these results might be related to blocking the diffusion path of hydrogen atoms.

10.2 Mg-SiC-Ni nanocomposites

1. After improvement of hydrogen diffusion path, adding a good catalyst like Ni would have additional improvements in hydrogen storage properties of MgH_2. Therefore, a sample of Mg+5wt% SiC+ 10 wt% Ni was prepared by reactive ball milling and its results were compared with the samples without Ni.

2. Mg particles convert to MgH_2 during ball milling much faster in presence of Ni and also, desorption temperature is decreased 80° C in comparison with the sample without Ni.

3. Hydrogen storage capacity and absorption/desorption kinetics significantly was improved by addition of Ni to the system. This could be a result of improvement of the surface area by SiC and catalytic effect of Ni for hydrogen molecules dissociation.

4. Hydriding/dehydriding kinetic investigation proved that the rate-limiting step for pure sample during desorption is the recombination of chemisorbed hydrogen atoms while for the Ni doped sample it changes to bulk nucleation and three-

dimensional growth of the existing nuclei as a result of catalytic effect of Ni towards recombination of hydrogen atoms and raising defects due to presence of SiC.

10.3 MgH_2-BCC composites

1. It has been shown that different kinds of Ti-based body centred cubic alloys have significant catalytic effects on MgH_2 sorption properties. Therefore, a new kind of these alloys, $Ti_{0.4}Mn_{0.22}Cr_{0.1}V_{0.28}$ (named BCC), was ball-milled with Mg in hydrogen atmosphere with different ball to powder weight ratio (BPWR).

2. The conversion of Mg to MgH_2 for the samples including the BCC is much faster than the pure one and the MgH_2-BCC sample have smaller particle size and less agglomeration. In addition, the desorption temperature decreases as a result of the BCC doping.

3. Hydrogen storage capacity and absorption/desorption kinetics for the MgH_2-BCC samples improve significantly. Additional improvements are achieved for the sample with higher BPWR. Furthermore, the PCI curves indicate an expansion of the unit cell in presence of the BCC.

4. These results may be related to catalytic effect of the BCC on hydrogen molecules dissociation by hydrogen absorption/desorption at low temperature. In which the BCC becomes hydride first and then desorbs its absorbed hydrogen in to the Mg particles.

10.4 MgH_2-BCC-CNT composition

1. It has been reported that a combination of CNTs with transition metals lead to a great improvement of hydrogen storage properties of MgH_2, therefore, a combination of the BCC ($Ti_{0.4}Mn_{0.22}Cr_{0.1}V_{0.28}$) with multi walled carbon nanotube (CNT) was ball-milled with MgH_2 in a planetary ball milling and its hydrogen storage properties compared with pure MgH_2 and MgH_2-BCC which were prepared with the same method.

Furthermore

2. The BCC particles distribute homogeneously among the MgH_2 particles on both surface and interior layers as a results of high energy ball milling. Furthermore, the desorption temperature is reduced up to 125 °C for the sample include CNT. Moreover, because the difference between T_{des} and T_{onset} is low for this sample, it releases hydrogen much easier than the samples without CNT.

3. The hydrogenation and dehydrogenation for MgH_2-BCC-CNT sample is rapider than both pure and MgH_2-BCC samples both in 300 °C and 250 °C. Moreover the maximum hydrogen absorbed is much higher for both doped samples in comparison with the pure one. These results indicate that the BCC and CNT have synergistic effects on all aspects of hydrogen storage properties of MgH_2.

4. The catalytic effects of the BCC are 1) dissociation of hydrogen molecule and 2) acting as an atomic hydrogen bridge in BCC/Mg interface and transform hydrogen atoms to Mg particles.

5. The effect of CNTs could be aggregation along the grain boundaries of Mg and facilitate penetration of hydrogen atoms to interior layers of Mg grains. The effects of BCC and CNT could be reverse during hydrogen desorption.

10.5 Mg-Ni as-cast, ball-milled and ball-milled-cast samples

1. It is accepted that cast eutectic Mg- Mg_2Ni can provide required interfaces for hydrogen diffusion into magnesium layers. On the other hand, ball milling a sample of Mg+Mg_2Ni *after* casting may facilitate the placement of the Mg_2Ni in deeper layers of Mg which can help the diffusion of hydrogen atoms into interior layers of Mg. Therefore, firstly, Mg-Ni (6wt%) was fabricated by melt processing and casting. Then a part of the obtained cast alloy was ball-milled by planetary and magneto ball-mill. The results were compared with ball-milled Mg+6wt%Ni powder. Ball milling for all samples were in presence of 5 wt% CNT for activation purpose.

2. The as-cast sample has a eutectic appearance. However, the eutectic structure is completely disturbed, and the particle size and agglomeration of its particles are also lower than in BM-cast and BM-powder samples.

3. Hydrogen absorption at 250 °C and 200 °C make it clear that all ball-milled samples perform faster kinetics and higher capacity in comparison with the as-cast sample. However, ball-milled samples do not show any considerable differences in hydrogen absorption behaviour, with or without prior casting. On the other hand, the desorption rate for all samples are almost the same.

4. The results indicate that doping Mg with a catalyst through ball-milling exhibit remarkable hydrogen sorption properties in comparison with casting as a consequence of introducing defects and active sites during ball milling. However, because the preparation by casting is a cheap method, ball milling of the cast material would be cheaper than ball milling of fine Mg nanopowder

10.6 Future works

Although some scientists believe that MgH_2 is not a good candidate for hydrogen storage because of its sluggish kinetics and high desorption temperature, this material is still one of the promising candidate for this purpose particularly after releasing the new DOE target [20]. To improve its hydrogen properties using new ceramic particles and preparing new combination of MgH_2/complex hydrides can be functional methods. In addition, working on guanidinium borohydride and fabricating a composition of it with MgH_2 can be useful method for further improvement of hydrogen storage properties of magnesium hydride.

References

1. *British Petroleum, Statistical Review of World Energy* 2003, BP: London.

2. World Bank, *World Development Indicators*. 2004.

3. Intergovernmental Panel on Climate Change (IPCC), *Special Report Emissions Scenarios*. 2000: Nairobi.

4. BGR, *Reserves Resources and Availability of Energy Resources*. 2002, Federal Institute for Geosciences and Natural Resources: Berlin, German Federal.

5. T.J. Blasing and S. Jones, *Current Greenhouse Gas Concentration.* Carbon Dioxide Information Analysis Center, available at http://cdiac.esd.ornl.gov, 2003.

6. International Energy Agency (IEA),*Head of Communication and Information Office.* 2009.

7. International Energy Agency (IEA), *World Energy Outlook.* http://www.iea.org//textbase/nppdf/free/2005/weo2005.pdf 2005.

8. *International Organization of Motor Vehicle Manufacturers (OICA), Climate Change and CO2: Automakers publish a comprehensive position paper 2007*

9. Veziroglu T. N. and F. Barbir, *Hydrogen: The Wonder Fuel.* International Journal of Hydrogen Energy, 1992. **17**: p. 391.

10. T.N. Veziroglu and F. Barbir, *Transportation Fuel-Hydrogen.* Energy Technology and the Environment, 1995. **4**(Wiley-Interscience): p. 2712.

11. J.W. Sheffield, *Assessment of Hydrogen Energy for Sustainable Development*. 2006: Springer.

12. Veziroglu T. N., *Hydrogen technology for energy needs of human settlements.* International Journal of Hydrogen Energy, 1987. **12**(2): p. 99.

13. F. Barbir, T.N. Veziroglu, and H.J. Plass, *Environmental Damage Due to Fossil Fuels Use.* International Journal of Hydrogen Energy, 1990. **15**(10): p. 739.

14. R. Narayanan and B. Viswanathan, *chemical and electrochemical energy sysytem*. 1998, Heydarabad: University press (India) limited.

15. N. Richter, *Introduction to Gasification.* www.gasification.org/Docs/02Richter.pdf, 2005.

16. H. Wendt and G. Imarisio, *Nine years of research and development on advanced water electrolysis. A review of the research programme of the Commission of the European Communities.* Journal of Applied Electrochemistry, 1988. **18**: p.1.

17. R.C. Prince and H.S. Kheshgi, *The photobiological production of hydrogen: potential efficiency and effectiveness as a renewable fuel.* Critical Reviews in Microbiology, 2005. **31**: p. 19.

18. P.R. Pathapati, X. Xue, and J. Tang, *A new dynamic model for predicting transient phenomena in a PEM fuel cell system.* Renewable Energy, 2004. **30**: p. 1.

19. EG&G Technical Services, *Fuel cell handbook.* 7th ed. U.S. Departement of Energy: Office of Fossil Energy. http://www.netl.doe.gov/technologies/coalpower/fuelcells/seca/pubs/FCHandbook7.pdf, 2004.

20. U.S. Department of Energy, 2009, *Target for Onboard Hydrogen Storage Systems for Light-Duty Vehicle.* http://www1.eere.energy.gov/hydrogenandfuelcells/storage/pdfs/targets_onboard_hydro_storage.pdf.

21. A. Züttel, *Hydrogen storage materials*, in *H_2-net seminar*. 2004: University of Birmingham, UK.

22. N. Takeichi, H. Senoh, and T. Yokota, *Hybrid hydrogen storage vessel, a novel high pressure hydrogen storage vessel combined with hydrogen storage material.* International Journal of Hydrogen Energy, 2003. **28**: p. 1121.

23. *www1.eere.energy.gov/hydrogenandfuelcells/storage/hydrogen_storage.htm.*

24. A. Züttel, *Materials for hydrogen storage.* Materials Today, 2003. **6**(9): p. 24.

25. S. Satyapal, J. Petrovic, C. Read, G. Thomas, and G. Ordaz, *The U.S. Department of Energy's National Hydrogen Storage Project: Progress towards meeting hydrogen-powered vehicle requirements.* Catalysis Today, 2007. **120**(3-4): p. 246.

26. *www.engineearth.com/news/86.*

27. V.P. Utgikar and T. Thiesen, *Safety of compressed hydrogen fuel tanks: Leakage from stationary vehicles.* Technology in Society, 2005. **27**(3): p. 315.

28. M. S. Dresselhaus and G. Dresselhaus, *Nanotechnology in carbon materials.* Nanostructured Materials, 1997. **9**(1-8): p. 33.

29. Y. Gogotsi, *Nanotubes and Nanofibers*. 2006, Boca Raton, FL: CRC PressTaylor & Francis Group.

30. E. Mélançon and P. Bénard, *Theoretical Study of the Contribution of Physisorption to the Low-Pressure Adsorption of Hydrogen on Carbon Nanotubes.* Langmuir, 2004. **20**(18): p. 7852.

31. A.C. Dillon, K.M. Jones, T.A. Bekkedahl, C.H. Kiang, and et al., *Storage of hydrogen in single-walled carbon nanotubes.* Nature, 1997. **386**(6623): p. 377.

32. Y.Y. Fan, B. Liao, M. Liu, Y.L.Wie, M.Q. Lu, and H.M. Cheng, *Hydrogen uptake in vapor-grown carbon nanofibers.* Carbon, 1999. **37**(10): p. 1649.

33. C. Liu, Y.Y. Fan, M. Liu, H.T. Cong, H.M. Cheng, and M.S. Dresselhaus, *Hydrogen Storage in Single-Walled Carbon Nanotubes at Room Temperature.* Science, 1999. **286**(5442): p. 1127.

34. E. Poirier, R. Chahine, P. Benard, D. Cossement, L. Lafi, E. Melancon, T.K. Bose, and S. Desilets, *Storage of hydrogen on single-walled carbon nanotubes and other carbon structures.* Applied Physics A, 2004. **78**: p. 961.

35. P.-X. Hou, S.-T. Xu, Z. Ying, Q.-H. Yang, C. Liu, and H.-M. Cheng, *Hydrogen adsorption/desorption behavior of multi-walled carbon nanotubes with different diameters.* Carbon, 2003. **41**(13): p. 2471.

36. X. Li, H. Zhu, L. Ci, C. Xu, Z. Mao, B. Wei, J. Liang, and D. Wu, *Hydrogen uptake by graphitized multi-walled carbon nanotubes under moderate pressure and at room temperature.* Carbon, 2001. **39**: p. 2077.

37. Y. Ye, C.C. Ahn, C. Witham, B. Fultz, J. Liu, A.G. Rinzler, D. Colbert, K.A. Smith, and R.E. Smalley, *Hydrogen adsorption and cohesive energy of single-walled carbon nanotubes.* Applied Physics Letters, 1999. **74**(16): p. 2307.

38. M. Becher, M. Haluska, M. Hirscher, A. Quintel, V. Skakalova, U. Dettlaff-Weglikovska, X. Chen, M. Hulman, Y. Choi, S. Roth, V. Meregalli, M. Parrinello, R. Ströbel, L. Jörissen, M.M. Kappes, J. Fink, A. Züttel, I. Stepanek, and P. Bernier, *Hydrogen storage in carbon nanotubes.* Comptes Rendus Physique, 2003. **4**(9): p. 1055.

39. E. Poirier, R. Chahine, P. Benard, L. Lafi, G. Dorval-Douville, and P.A. Chandonia, *Hydrogen Adsorption Measurements and Modeling on Metal-Organic Frameworks and Single-Walled Carbon Nanotubes.* Langmuir, 2006. **22**(21): p. 8784.

40. A. Ansón, M.A. Callejas, A.M. Benito, W.K. Maser, M.T. Izquierdo, B. Rubio, J. Jagiello, M. Thommes, J.B. Parra, and M.T. Martínez, *Hydrogen adsorption studies on single wall carbon nanotubes.* Carbon, 2004. **42**(7): p. 1243.

41. B.P. Tarasov, J.P. Maehlen, M.V. Lototsky, V.E. Muradyan, and V.A. Yartys, *Hydrogen sorption properties of arc generated single-wall carbon nanotubes.* Journal of Alloys and Compounds, 2003. **356-357**: p. 510.

42. N. Nishimiya, K. Ishigaki, H. Takikawa, M. Ikeda, Y. Hibi, T. Sakakibara, A. Matsumoto, and K. Tsutsumi, *Hydrogen sorption by single-walled carbon nanotubes prepared by a torch arc method.* Journal of Alloys and Compounds, 2002. **339**(1-2): p. 275.

43. S. Yamanaka, M. Fujikane, M. Uno, H. Murakami, and O. Miura, *Hydrogen content and desorption of carbon nano-structures.* Journal of Alloys and Compounds, 2004. **366**(1-2): p. 264.

44. H.W. Langmi, A. Walton, M.M. Al-Mamouri, S.R. Johnson, D. Book, J.D. Speight, P.P. Edwards, I. Gameson, P.A. Anderson, and I.R. Harris, *Hydrogen adsorption in zeolites A, X, Y and RHO.* Journal of Alloys and Compounds, 2003. **356-357**: p. 710.

45. J. Weitkamp, M. Fritz, and S. Ernst, *Zeolites as media for hydrogen storage.* International Journal of Hydrogen Energy, 1995. **20**(12): p. 967.

46. D. Fraenkel and J. Shabtai, *Encapsulation of hydrogen in molecular sieve zeolites.* Journal of the American Chemical Society, 1977. **99**(21): p. 7074.

47. W. Henrietta, G. Langmi, and S. McGrady, *Non-hydride systems of the main group elements as hydrogen storage materials.* Coordination Chemistry Reviews, 2007. **251**: p. 925.

48. V.B. Kazansky, F.C. Jentoft, and H.G. Karge, *First observation of vibration–rotation drift spectra of para- and ortho-hydrogen adsorbed at 77 K on LiX, NaX and CsX zeolites.* Jornal of Chemical Society, 1998. **94**: p. 1374.

49. F. Darkrim, A. Asdin, M. Pierre, and L. Dominique, *Hydrogen adsorption in the NaA zeolite: A comparison between numerical simulations and experiments.* The Journal of Chemical Physics, 2000. **112**(13): p. 5991.

50. M.G. Nijkamp, J.E.M.J. Raaymakers, A.J. van Dillen, and de Jong, *Hydrogen storage using physisorption – materials demands.* Applied Physics A, 2001. **72**: p. 619.

51. P.M. Forster, J. Eckert, J.-S. Chang, S.-E. Park, G. Ferey, and A.K. Cheetham, *Hydrogen adsorption in nanoporous nickel(II) phosphates.* Journal of American Chemical Society, 2003. **125**: p. 1309.

52. X.M. Du and Wu E D, *Physisorption of hydrogen in A, X and ZSM-5 types of zeolites at moderately high pressures.* Chinese Journal of Chemical Physics, 2006. **19**: p. 457.

53. B. Xiao and Qingchun Yuan, *Nanoporous metal organic framework materials for hydrogen storage.* Particuology, 2009. **7**: p. 129.

54. N.L. Rosi, J. Eckert, M. Eddaoudi, D.T. Vodak, J. Kim, and M. O'Keeffe, *Hydrogen storage in microporous metal-organic frameworks.* Science, 2003. **300**: p. 1127.

55. J.L.C. Rowsell, A.R. Millward, K.S. Park, and O.M. Yaghi, *Hydrogen sorption in functionalized metal-organic frameworks.* Journal of the American Chemical Society, 2004. **126**: p. 5666.

56. F.A.G. Wong, A.J. Matzger, and O.M. Yaghi, *Exceptional H2 saturation uptake in microporous metal-organic frameworks.* Journal of the American Chemical Society, 2006. **128**: p. 3494.

57. B. Xiao, P.S. Wheatley, X. Zhao, A.J. Fletcher, S. Fox, and A.G. Rossi, *High-capacity hydrogen and nitric oxide adsorption and storage in a metal-organic framework.* Journal of the American Chemical Society, 2007. **129**: p. 1203.

58. B. Panella, M. Hirscher, H. Pütter, and U. Müller, *Hydrogen Adsorption in Metal-Organic Frameworks: Cu-MOFs and Zn-MOFs Compared.* Advaced Functional Materials, 2006. **16**: p. 520.

59. G. Garberoglio, A.I. Skoulidas, and J.K. Johnson, *Adsorption of Gases in Metal Organic Materials: Comparison of Simulations and Experiments.* Journal of Physical Chemistry B, 2005. **109**: p. 13094.

60. A. Chambers, C. Park, R.T.K. Baker, and N.M. Rodriguez, *Hydrogen Storage in Graphite Nanofibers.* The Journal of Physical Chemistry B, 1998. **102**(22): p. 4253.

61. M. Ritschel, M. Uhlemann, O. Gutfleisch, A. Leonhardt, A. Graff, Ch. Täschner, and J. Fink, *Hydrogen storage in different carbon nanostructures.* Applied Physics Letters, 2002. **80**: p. 2985.

62. B.K. Gupta, R.S. Tiwari, and O.N. Srivastava, *Studies on synthesis and hydrogenation behaviour of graphitic nanofibres prepared through palladium catalyst assisted thermal cracking of acetylene.* Journal of Alloys and Compounds, 2004. **381**(1-2): p. 301.

63. B. J. Kim, Y.-S. Lee, and S.-J. Park, *Preparation of platinum-decorated porous graphite nanofibers, and their hydrogen storage behaviors.* Journal of Colloid and Interface Science, 2008. **318**(2): p. 530.

64. S. I. Orimo, Y. Nakamori, J.R. Eliseo, A. Zuttel, and C.M. Jensen, *Complex Hydrides for Hydrogen Storage.* Chemical Reviews, 2007. **107**(10): p. 4111.

65. Y. Nakamori, H.W. Li, K. Kikuchi, M. Aoki, K. Miwa, S. Towata, and S. Orimo, *Thermodynamical stabilities of metal-borohydrides.* Journal of Alloys and Compounds, 2007. **446-447**: p. 296-300.

66. S.K. Ravhi and L.C. Andrew, *Structural transitions in $NaBH_4$ under pressure.* Applied Physics Letters, 2005. **87**(26): p. 261916.

67. B. Bogdanovi and M. Schwickardi, *Ti-doped alkali metal aluminium hydrides as potential novel reversible hydrogen storage materials.* Journal of Alloys and Compounds, 1997. **253-254**: p. 1.

68. B. Bogdanovicacute, M. Felderhoff, S. Kaskel, A. Pommerin, K. Schlichte, and F. Schüth, *Improved Hydrogen Storage Properties of Ti-Doped Sodium Alanate Using Titanium Nanoparticles as Doping Agents.* Advanced Materials, 2003. **15**(12): p. 1012.

69. D.L. Anton, *Hydrogen desorption kinetics in transition metal modified $NaAlH_4$.* Journal of Alloys and Compounds, 2003. **356-357**: p. 400.

70. O. Palumbo, A. Paolone, R. Cantelli, C.M. Jensen, and R. Ayabe, *Monitoring of chemical reactions and point defect dynamics in sodium alanates.* Materials Science and Engineering: A, 2006. **442**(1-2): p. 75.

71. O. Palumbo, A. Paolone, R. Cantelli, C.M. Jensen, and M. Sulic, *Fast H-vacancy Dynamics during Alanate Decomposition by Anelastic Spectroscopy. Proposition of a Model for Ti-enhanced Hydrogen Transport.* The Journal of Physical Chemistry B, 2006. **110**(18): p. 9105.

72. R. Cantelli, O. Palumbo, A. Paolone, C.M. Jensen, M.T. Kuba, and R. Ayabe, *Dynamics of defects in alanates.* Journal of Alloys and Compounds, 2007. **446-447**: p. 260.

73. C.M. Jensen and K.J. Gross, *Development of catalytically enhanced sodium aluminum hydride as a hydrogen-storage material.* Applied Physics A, 2001. **72**: p. 213.

74. J. Block and Gray A. P., *The thermal decomposition o lithium aluminium hydride.* Inorganic Chemistry, 1965. **4**: p. 304.

75. P.B. Viktor, K. W.Dennisa, and V.K. Pecharsky, *Rapid solid-state transformation of tetrahedral $[AlH_4]_2$ into octahedral $[AlH_6]_{32}$ in lithium aluminohydride.* Chemicals Communications, 2000. **17**: p. 1665.

76. J. Chen, N. Kuriyama, Q. Xu, H.T. Takeshita, and T. Sakai, *Reversible Hydrogen Storage via Titanium-Catalyzed $LiAlH_4$ and Li_3AlH_6.* The Journal of Physical Chemistry B, 2001. **105**(45): p. 11214.

77. J. Wang, A.D. Ebner, and J.A. Ritter, *Physiochemical Pathway for Cyclic Dehydrogenation and Rehydrogenation of $LiAlH_4$.* Journal of the American Chemical Society, 2006. **128**(17): p. 5949.

78. A. Fossdal, H.W. Brinks, M. Fichtner, and B.C. Hauback, *Determination of the crystal structure of $Mg(AlH_4)_2$ by combined X-ray and neutron diffraction.* Journal of Alloys and Compounds, 2005. **387**(1-2): p. 47.

79. M. Fichtner, O. Fuhr, and O. Kircher, *Magnesium alanate--a material for reversible hydrogen storage?* Journal of Alloys and Compounds, 2003. **356-357**: p. 418.

80. K. Komiya, N. Morisaku, Y. Shinzato, K. Ikeda, S. Orimo, Y. Ohki, K. Tatsumi, H. Yukawa, and M. Morinaga, *Synthesis and dehydrogenation of $M(AlH_4)_2$ (M = Mg, Ca).* Journal of Alloys and Compounds, 2007. **446-447**: p. 237.

81. M. Mamatha, C. Weidenthaler, A. Pommerin, M. Felderhoff, and F. Schüth, *Comparative studies of the decomposition of alanates followed by in situ XRD and DSC methods.* Journal of Alloys and Compounds, 2006. **416**(1-2): p. 303.

82. M. Schwarz, A. Haiduc, H. Stil, P. Paulus, and H. Geerlings, *The use of complex metal hydrides as hydrogen storage materials: Synthesis and XRD-studies of $Ca(AlH_4)_2$ and $Mg(AlH_4)_2$.* Journal of Alloys and Compounds, 2005. **404-406**: p. 762.

83. U. Bilici, *Sodium borohydride production methods.*, in *Second international boron symposium*. 23-25 September 2004: Eskisxehir, Turkey. p. 119.

84. U.B. Demirci and P. Miele, *Sodium tetrahydroborate as energy/hydrogen carrier, its history.* Comptes Rendus Chimie, 2009. **12**(9): p. 943.

85. S. Suda, N. Morigasaki, Y. Iwase, and Z.P. Li, *Production of sodium borohydride by using dynamic behaviors of protide at the extreme surface of magnesium particles.* Journal of Alloys and Compounds, 2005. **404-406**: p. 643.

86. J.S. Zhang, W.N. Delgass, T.S. Fisher, and J.P. Gore, *Kinetics of Ru-catalyzed sodium borohydride hydrolysis.* Journal of Power Sources, 2007. **164**(2): p. 772.

87. U.B. Demirci, O. Akdim, and P. Miele, *Ten-year efforts and a no-go recommendation for sodium borohydride for on-board automotive hydrogen storage.* International Journal of Hydrogen Energy, 2009. **34**(6): p. 2638.

88. H.I. Schlesinger and H.C. Brown, *Metallo Borohydrides. III. Lithium Borohydride.* Journal of the American Chemical Society, 2002. **62**(12): p. 3429.

89. W.D. Davis, L.S. Mason, and G. Stegeman, *The Heats of Formation of Sodium Borohydride, Lithium Borohydride and Lithium Aluminum Hydride.* Journal of the American Chemical Society, 2002. **71**(8): p. 2775.

90. A. Züttel, S. Rentsch, P. Fischer, P. Wenger, P. Sudan, P. Mauron, and C. Emmenegger, *Hydrogen storage properties of $LiBH_4$.* Journal of Alloys and Compounds, 2003. **356-357**: p. 515.

91. J.J. Vajo, S.L. Skeith, and F. Mertens, *Reversible Storage of Hydrogen in Destabilized $LiBH_4$.* The Journal of Physical Chemistry B, 2005. **109**(9): p. 3719.

92. M. Q. Fan, L.-X. Sun, Y. Zhang, F. Xu, J. Zhang, and H.-l. Chu, *The catalytic effect of additive Nb_2O_5 on the reversible hydrogen storage performances of $LiBH_4$-MgH_2 composite.* International Journal of Hydrogen Energy, 2008. **33**(1): p. 74.

93. J. F. Mao, Z.P. Guo, H.K. Liu, and X.B. Yu, *Reversible hydrogen storage in titanium-catalyzed $LiAlH_4$-$LiBH_4$ system.* Journal of Alloys and Compounds, 2009. **487**(1-2): p. 434.

94. N. Hanada, Krzysztof Chopek, Christoph Frommen, W. Lohstroh, and M. Fichtner, *Thermal decomposition of $Mg(BH_4)_2$ under He flow and H_2 pressure* Journal of Materials Chemistry, 2008. **18**: p. 2611.

95. H.W. Li, K. Kikuchi, Y. Nakamori, N. Ohba, K. Miwa, S. Towata, and S. Orimo, *Dehydriding and rehydriding processes of well-crystallized $Mg(BH_4)_2$ accompanying with formation of intermediate compounds.* Acta Materialia, 2008. **56**(6): p. 1342-1347.

96. H.W. Li, K. Kikuchi, Y. Nakamori, K. Miwa, S. Towata, and S. Orimo, *Effects of ball milling and additives on dehydriding behaviors of well-crystallized $Mg(BH_4)_2$.* Scripta Materialia, 2007. **57**(8): p. 679.

97. S. Satyapal, Krzysztof Chopek, Christoph Frommen, Aline Léon, O. Zabara, and M. Fichtner, *ynthesis and properties of magnesium tetrahydroborate, $Mg(BH_4)_2$* Journal of Material Chemistry, 2007. **17**: p. 3496.

98. M. Fichtner, Z.-K. Zhirong, J. Hu, A. Roth, and PeterWeidler, *The kinetic properties of $Mg(BH_4)_2$ infiltrated in activated carbon.* Nanotechnology, 2009. **20**: p. 204029.

99. X.B. Yu, Y. H. Gu, Z.P. Guo, A. Ranjbar, and H. K. Liua, *A new multicompound hydrogen storage system: $Mg(BH_4)_2$-$LiNH_2$.* The Journal of Physical Chemistry C, 2009. **Under review.**

100. Z. Z. Fang, X.-D. Kang, P. Wang, H.-W. Li, and S.-I. Orimo, *Unexpected dehydrogenation behavior of LiBH4/Mg(BH$_4$)$_2$ mixture associated with the in situ formation of dual-cation borohydride.* Journal of Alloys and Compounds, 2009. **491**(1-2): p. L1.

101. K. Miwa, A. Masakazu, N. Tatsuo, O. Nobuko, N. Yuko, T. Shin-ichi, Z. Andreas, and O. Shin-ichi, *Thermodynamical stability of calcium borohydride Ca(BH$_4$)$_2$.* Physical Review B, 2006. **74**(15): p. 155122.

102. Y. Nakamori, M. Kazutoshi, N. Akihito, L. Haiwen, O. Nobuko, T. Shin-ichi, Z. Andreas, and O. Shin-ichi, *Correlation between thermodynamical stabilities of metal borohydrides and cation electronegativites: First-principles calculations and experiments.* Physical Review B (Condensed Matter and Materials Physics), 2006. **74**(4): p. 045126.

103. Y. Kim, D. Reed, Y.-S. Lee, J.Y. Lee, J.-H. Shim, D. Book, and Y.W. Cho, *Identification of the Dehydrogenated Product of Ca(BH$_4$)$_2$.* The Journal of Physical Chemistry C, 2009. **113**(14): p. 5865.

104. J. H. Kim, S.-A. Jin, J.-H. Shim, and Y.W. Cho, *Thermal decomposition behavior of calcium borohydride Ca(BH$_4$)$_2$.* Journal of Alloys and Compounds, 2008. **461**(1-2): p. L20.

105. M. D. Riktor, M. H. Sørby, K. Chopek, M. Fichtner, F. Buchter, A. Züttel, and B. C. Hauback, *In situ synchrotron diffraction studies of phase transitions and thermal decomposition of Mg(BH$_4$)$_2$ and Ca(BH$_4$)$_2$.* Journal of Material Chemistry, 2007. **17**: p. 4939.

106. E. Ronnebro, MRS Fall Meeting, 2007, Boston.

107. P. Chen, X. Zhitao, L. Jizhong, L. Jianyi, and T. Kuang Lee, *Interaction of hydrogen with metal nitrides and imides.* Nature, 2002. **420**(6913): p. 302.

108. G. Walker, *Solid-state hydrogen storage*. 2008, Cambridge England: Woodan Published Limited.

109. T. Ichikawa, N. Hanada, S. Isobe, H. Leng, and H. Fujii, *Mechanism of Novel Reaction from LiNH$_2$ and LiH to Li$_2$NH and H$_2$ as a Promising Hydrogen Storage System.* The Journal of Physical Chemistry B, 2004. **108**(23): p. 7887.

110. T. Markmaitree, R. Ren, and L.L. Shaw, *Enhancement of Lithium Amide to Lithium Imide Transition via Mechanical Activation.* The Journal of Physical Chemistry B, 2006. **110**(41): p. 20710.

111. S. Isobe, T. Ichikawa, N. Hanada, H.Y. Leng, M. Fichtner, O. Fuhr, and H. Fujii, *Effect of Ti catalyst with different chemical form on Li-N-H hydrogen storage properties.* Journal of Alloys and Compounds, 2005. **404-406**: p. 439.

112. J. P. Bastide, B. Bonnetot, J.-M. Létoffé, and P. Claudy, *Polymorphisme de l'hydrure de magnesium sous haute pression.* Materials Research Bulletin, 1980. **15**(9): p. 1215.

113. C. Lexcellent and G. Gondor, *Analysis of hydride formation for hydrogen storage: Pressure-composition isotherm curves modeling.* Intermetallics, 2007. **15**(7): p. 934.

114. G. Liang, J. Huot, S. Boily, and R. Schulz, *Hydrogen desorption kinetics of a mechanically milled MgH_2+5at.%V nanocomposite.* Journal of Alloys and Compounds, 2000. **305**(1-2): p. 239.

115. M. Martin, C. Gommel, C. Borkhart, and E. Fromm, *Absorption and desorption kinetics of hydrogen storage alloys.* Journal of Alloys and Compounds, 1996. **238**(1-2): p. 193.

116. J. H. SHARP, G. W. BRINDLEY, and B.N.N. ACHAR, *Numerical Data for Some Commonly Used Solid State Reaction Equations.* Journal of the American Ceramic Society. **49**: p. 379.

117. M. H. Mintz and J. Bloch, *Evaluation of the kinetics and mechanisms of hybriding reactions.* Progress in Solid State Chemistry, 1985. **16**(3): p. 163.

118. G. Sandrack, *A panoramic overview of hydrogen storag alloys from gas reaction point of view.* Journal of Alloys and Compounds, 1999. **293-295**: p. 877.

119. S. Corré, M. Bououdina, D. Fruchart, and G.-y. Adachi, *Stabilisation of high dissociation pressure hydrides of formula $La_{1-x}CexNi_5$ (x=0-0.3) with carbon monoxide.* Journal of Alloys and Compounds, 1998. **275-277**: p. 99.

120. D. Lu, W. Li, S. Hu, F. Xiao, and R. Tang, *Uniform nanocrystalline AB_5-type hydrogen storage alloy: Preparation and properties as negative materials of Ni/MH battery.* International Journal of Hydrogen Energy, 2006. **31**(6): p. 678.

121. J. M. Joubert, M. Latroche, R. Cerný, R.C. Bowman, A. Percheron-Guégan, and K. Yvon, *Crystallographic study of $LaNi_{5-x}Snx$ (0.2<=x<=0.5) compounds and their hydrides.* Journal of Alloys and Compounds, 1999. **293-295**: p. 124.

122. R. K. Jain, A. Jain, S. Agarwal, N.P. Lalla, V. Ganesan, D.M. Phase, and I.P. Jain, *Hydrogenation behaviour of Ce-based AB_5 intermetallic compounds.* Journal of Alloys and Compounds, 2007. **440**(1-2): p. 84.

123. J. J. Reilly and R.H. Wiswall, *Formation and properties of iron titanium hydride.* Inorganic Chemistry, 2002. **13**(1): p. 218.

124. M. Bououdina, D. Grant, and G. Walker, *Review on hydrogen absorbing materials--structure, microstructure, and thermodynamic properties.* International Journal of Hydrogen Energy, 2006. **31**(2): p. 177.

125. L. Zaluski, A. Zaluska, and J.O. Strom-Olsen, *Nanocrystakkine metal hydrides.* Journal of Alloys and Compounds, 1997. **253-254**: p. 70-79.

126. S. H. Lim and L. Jai-Young, *The effects of aluminium substitution in TiFe on its hydrogen absorption properties.* Journal of the Less Common Metals, 1984. **97**: p. 65.

127. B. K. Singh, A.K. Singh, and O.N. Srivastava, *On the synthesis, characterization and hydrogenation behaviour of Fe1 - xTi1 + yNi$_x$ (x = 0.2, y = 0.3) hydrogen storage material.* International Journal of Hydrogen Energy, 1997. **22**(8): p. 805.

128. X. B. Yu, Z. Wu, B.J. Xia, and N.X. Xu, *Enhancement of hydrogen storage capacity of Ti-V-Cr-Mn BCC phase alloys.* Journal of Alloys and Compounds, 2004. **372**(1-2): p. 272.

129. T. Huang, Z. Wu, B. Xia, J. Chen, X. Yu, N. Xu, C. Lu, and H. Yu, *TiCr$_{1.2}$(V-Fe)$_{0.6}$--a novel hydrogen storage alloy with high capacity.* Science and Technology of Advanced Materials, 2003. **4**(6): p. 491.

130. J. Mi, X. Guo, X. Liu, L. Jiang, Z. Li, L. Hao, and S. Wang, *Effect of Al on microstructures and hydrogen storage properties of Ti$_{26.5}$Cr$_{20}$(V$_{0.45}$Fe$_{0.085}$)$_{100-x}$Al$_x$Ce$_{0.5}$ alloy.* Journal of Alloys and Compounds, 2009. **485**(1-2): p. 324.

131. A. Zaluska, L. Zaluski, and J.O. Ström-Olsen, *Nanocrystalline magnesium for hydrogen storage.* Journal of Alloys and Compounds, 1999. **288**(1-2): p. 217.

132. P. Jolibois, *Study of pure magnesium and magnesium hydrides*. *Comptes Rendues*. 1912: Academie Science Paris. p. 353.

133. T. Noritake, M. Aoki, S. Towata, Y. Seno, Y. Hirose, E. Nishibori, M. Takata, and M. Sakata, *Chemical bonding of hydrogen in MgH$_2$.* Applied Physics Letters, 2002. **81**(11): p. 2008.

134. N. Eigen, C. Keller, M. Dornheim, T. Klassen, and R. Bormann, *Industrial production of light metal hydrides for hydrogen storage.* Scripta Materialia, 2007. **56**(10): p. 847.

135. P.F. Bernath, J. H. Black, and J.W. Brault, *The Spectrum Of Magnesium Hydride.* The Astrophysical Journal, 1985. **298**: p. 375.

136. V. Fournier, P. Marcus, and I. Olefjord, *Oxidation of magnesium Surface and Interface Analysis.* Surface and Interface Analysis, 2002. **34**(1): p. 494.

137. A. San-Martin and F. D. Manchester, *The H–Mg (hydrogen–magnesium) system.* Bulletin of Alloy Phase Diagrams, 1987. **8**: p. 431.

138. F. H. Ellinger, C. E. Holley, B. B. McInteer, D. Pavone, R.M. Potter, E. Staritzky, and W.H. Zachariasen, *The Preparation and Some Properties of Magnesium Hydride1.* Journal of the American Chemical Society, 2002. **77**(9): p. 2647.

139. J. F. Stampfer, C.E. Holley, and J.F. Suttle, *The Magnesium-Hydrogen System1-3.* Journal of the American Chemical Society, 2002. **82**(14): p. 3504.

140. B. Bogdanovic, K. Bohmhammel, B. Christ, A. Reiser, K. Schlichte, R. Vehlen, and U. Wolf, *Thermodynamic investigation of the magnesium-hydrogen system.* Journal of Alloys and Compounds, 1999. **282**(1-2): p. 84.

141. V. Bérubé, Gregg Radtke, M. Dresselhaus, and G. Chen, *Size effects on the hydrogen storage properties of nanostructured metal hydrides: A review.* International Journal of Energy Research, 2007. **31**(6): p. 637.

142. K. Bohmhammel, B. Christ, and G. Wolf, *Kinetic investigations on the basis of isothermal DSC measurements of hydrogenation and dehydrogenation of magnesium hydride.* Thermochimica Acta, 1998. **310**(1-2): p. 167.

143. C. Suryanarayana, *Mechanical alloying and milling.* Progress in Materials Science, 2001. **46**(1-2): p. 1.

144. C. Chun, *Controlled mechano-chemical synthesis and properties of nanostructured hydrides in the Mg-Al-H and Mg-B-H systems*, in *Mechanical & Mechatronic Engineering*. 2007, University of Waterloo: Waterloo, Ontario, Canada.

145. J. Huot, G. Liang, S. Boily, A. Van Neste, and R. Schulz, *Structural study and hydrogen sorption kinetics of ball-milled magnesium hydride.* Journal of Alloys and Compounds, 1999. **293-295**: p. 495.

146. R.A. Varin, T. Czujko, and Z. Wronski, *Particle size, grain size and γ -MgH_2 effects on the desorption properties of nanocrystalline commercial magnesium hydride processed by controlled mechanical milling.* Nanotechnology 2006. **17** p. 3856.

147. P. Selvam, B. Viswanathan, C.S. Swamy, and V. Srinivasan, *Magnesium and magnesium alloy hydrides.* International Journal of Hydrogen Energy, 1986. **11**(3): p. 169.

148. G. Barkhordarian, T. Klassen, and R. Bormann, *Kinetic investigation of the effect of milling time on the hydrogen sorption reaction of magnesium catalyzed with different Nb_2O_5 contents.* Journal of Alloys and Compounds, 2006. **407**(1-2): p. 249.

149. J. Charbonnier, P. de Rango, D. Fruchart, S. Miraglia, L. Pontonnier, S. Rivoirard, N. Skryabina, and P. Vulliet, *Hydrogenation of transition element additives (Ti, V) during ball milling of magnesium hydride.* Journal of Alloys and Compounds, 2004. **383**(1-2): p. 205.

150. Z. Dehouche, T. Klassen, W. Oelerich, J. Goyette, T.K. Bose, and R. Schulz, *Cycling and thermal stability of nanostructured MgH_2-Cr_2O_3 composite for hydrogen storage.* Journal of Alloys and Compounds, 2002. **347**(1-2): p. 319.

151. G. Liang, J. Huot, S. Boily, A. Van Neste, and R. Schulz, *Hydrogen storage properties of the mechanically milled MgH_2-V nanocomposite.* Journal of Alloys and Compounds, 1999. **291**(1-2): p. 295.

152. G. Liang, J. Huot, S. Boily, A. Van Neste, and R. Schulz, *Catalytic effect of transition metals on hydrogen sorption in nanocrystalline ball milled MgH_2-Tm (Tm=Ti, V, Mn, Fe and Ni) systems.* Journal of Alloys and Compounds, 1999. **292**(1-2): p. 247.

153. N. Hanada, T. Ichikawa, and H. Fujii, *Catalytic Effect of Nanoparticle 3d-Transition Metals on Hydrogen Storage Properties in Magnesium Hydride MgH_2 Prepared by Mechanical Milling.* The Journal of Physical Chemistry B, 2005. **109**(15): p. 7188.

154. R.L. Holtz and M.A. Imam, *Hydrogen storage characteristics of ball-milled magnesium-nickel and magnesium-iron alloys.* Journal of Materials Science 1999. **34**: p. 2655.

155. R.A. Varin, T. Czujko, E.B. Wasmund, and Z.S. Wronski, *Catalytic effects of various forms of nickel on the synthesis rate and hydrogen desorption properties of nanocrystalline magnesium hydride (MgH_2) synthesized by controlled reactive mechanical milling (CRMM).* Journal of Alloys and Compounds, 2007. **432**(1-2): p. 217.

156. J. Huot, J.F. Pelletier, G. Liang, M. Sutton, and R. Schulz, *Structure of nanocomposite metal hydrides.* Journal of Alloys and Compounds, 2002. **330-332**: p. 727.

157. J. Huot, J.F. Pelletier, L.B. Lurio, M. Sutton, and R. Schulz, *Investigation of dehydrogenation mechanism of MgH_2-Nb nanocomposites.* Journal of Alloys and Compounds, 2003. **348**(1-2): p. 319.

158. L. Zaluski, A. Zaluska, P. Tessier, J.O. Ström-Olsen, and R. Schulz, *Catalytic effect of Pd on hydrogen absorption in mechanically alloyed Mg_2Ni, $LaNi_5$ and FeTi.* Journal of Alloys and Compounds, 1995. **217**(2): p. 295.

159. H. B. Lu, C.K. Poh, L.C. Zhang, Z.P. Guo, X.B. Yu, and H.K. Liu, *Dehydrogenation characteristics of Ti- and Ni/Ti-catalyzed Mg hydrides.* Journal of Alloys and Compounds, 2009. **481**(1-2): p. 152.

160. R. Baer, Y. Zeiri, and R. Kosloff, *Hydrogen transport in nickel (111).* Physical Review B (Condensed Matter and Materials Physics), 1997. **55**(16): p. 952.

161. J. Bloch and M.H. Mintz, *Kinetics and mechanisms of metal hydrides formation--a review.* Journal of Alloys and Compounds, 1997. **253-254**: p. 529.

162. T. R. Jensen, A. Andreasen, T. Vegge, J.W. Andreasen, K. Ståhl, A.S. Pedersen, M.M. Nielsen, A.M. Molenbroek, and B. Flemming, *Dehydrogenation kinetics of pure and nickel-doped magnesium hydride investigated by in situ time-resolved powder X-ray diffraction.* International Journal of Hydrogen Energy, 2006. **31**(14): p. 2052.

163. F. V. Zeppelin, H. Reule, and M. Hirscher, *Hydrogen desorption kinetics of nanostructured MgH_2 composite materials.* Journal of Alloys and Compounds, 2002. **330-332**: p. 723.

164. W. Oelerich, T. Klassen, and R. Bormann, *Comparison of the catalytic effects of V, V_2O_5, VN, and VC on the hydrogen sorption of nanocrystalline Mg.* Journal of Alloys and Compounds, 2001. **322**(1-2): p. L5.

165. K. S. Jung, E.Y. Lee, and K.S. Lee, *Catalytic effects of metal oxide on hydrogen absorption of magnesium metal hydride.* Journal of Alloys and Compounds, 2006. **421**(1-2): p. 179.

166. J. L. Bobet, F.J. Castro, and B. Chevalier, *Effects of RMG conditions on the hydrogen sorption properties of Mg + Cr_2O_3 mixtures.* Scripta Materialia, 2005. **52**(1): p. 33.

167. K. F. Aguey-Zinsou, T. Nicolaisen, J.R. Ares Fernandez, T. Klassen, and R. Bormann, *Effect of nanosized oxides on MgH_2 (de)hydriding kinetics.* Journal of Alloys and Compounds, 2007. **434-435**: p. 738.

168. W. Oelerich, T. Klassen, and R. Bormann, *Metal oxides as catalysts for improved hydrogen sorption in nanocrystalline Mg-based materials.* Journal of Alloys and Compounds, 2001. **315**(1-2): p. 237.

169. Z.G. Huang, Z.P. Guo, A. Calka, D. Wexler, C. Lukey, and H.K. Liu, *Effects of iron oxide (Fe_2O_3, Fe_3O_4) on hydrogen storage properties of Mg-based composites.* Journal of Alloys and Compounds, 2006. **422**(1-2): p. 299.

170. G. Barkhordarian, T. Klassen, and R. Bormann, *Fast hydrogen sorption kinetics of nanocrystalline Mg using Nb_2O_5 as catalyst.* Scripta Materialia, 2003. **49**(3): p. 213.

171. O. Friedrichs, J.C. Sanchez-Lopez, C. Lopez-Cartes, T. Klassen, R. Bormann, and A. Fernandez, *Hydrogen sorption improvement of nanocrystalline MgH_2 by Nb_2O_5 nanoparticles.* The Journal of Physical Chemistry B, 2006. **110**(15): p. 7845.

172. R. Gupta, F. Agresti, S.L. Russo, A. Maddalena, P. Palade, and G. Principi, *Structure and hydrogen storage properties of MgH_2 catalysed with La_2O_3.* Journal of Alloys and Compounds, 2008. **450**(1-2): p. 310.

173. K.F. Aguey-Zinsou, J.R. Ares Fernandez, T. Klassen, and R. Bormann, *Effect of Nb_2O_5 on MgH_2 properties during mechanical milling.* International Journal of Hydrogen Energy, 2007. **32**(13): p. 2400.

174. N. Hanada, T. Ichikawa, S. Hino, and H. Fujii, *Remarkable improvement of hydrogen sorption kinetics in magnesium catalyzed with Nb_2O_5.* Journal of Alloys and Compounds, 2006. **420**(1-2): p. 46.

175. Y.Q. Hu, H.F. Zhang, A.M. Wang, B.Z. Ding, and Z.Q. Hu, *Preparation and hydriding/dehydriding properties of mechanically milled Mg-30 wt% $TiMn_{1.5}$ composite.* Journal of Alloys and Compounds, 2003. **354**(1-2): p. 296.

176. Y.Q. Hu, C. Yan, H.F. Zhang, L. Ye, and Z.Q. Hu, *Preparation and hydrogenation characteristics of Mg-30 wt.% $Ti_{37.5}$ V_{25} $Cr_{37.5}$ composite.* Journal of Alloys and Compounds, 2004. **375**(1-2): p. 265.

177. G. Liang, J. Huot, S. Boily, A. Van Neste, and R. Schulz, *Hydrogen storage in mechanically milled Mg-$LaNi_5$ and MgH_2-$LaNi_5$ composites.* Journal of Alloys and Compounds, 2000. **297**(1-2): p. 261.

178. E. Grigorova, M. Khristov, M. Khrussanova, J.L. Bobet, and P. Peshev, *Effect of additives on the hydrogen sorption properties of mechanically alloyed composites based on Mg and Mg_2Ni.* International Journal of Hydrogen Energy, 2005. **30**(10): p. 10995.

179. Z. Li, X. Liu, L. Jiang, and S. Wang, *Characterization of Mg-20 wt% Ni-Y hydrogen storage composite prepared by reactive mechanical alloying.* International Journal of Hydrogen Energy, 2007. **32**(12): p. 1869.

180. R. Vijay, R. Sundaresan, M.P. Maiya, S. Srinivasa Murthy, Y. Fu, H.P. Klein, and M. Groll, *Characterisation of Mg-x wt.% FeTi (x = 5-30) and Mg-40 wt.% FeTiMn hydrogen absorbing materials prepared by mechanical alloying.* Journal of Alloys and Compounds, 2004. **384**(1-2): p. 283.

181. H. Gu, Y. Zhu, and L. Li, *Characterization of hydrogen storage properties of Mg-30 wt.% $Ti_{1.0}V_{1.1}Mn_{0.9}$ composite.* Journal of Alloys and Compounds, 2006. **424**(1-2): p. 382.

182. X.B. Yu, Y.H. Guo, Z.X. Yang, Z.P. Guo, H.K. Liu, and S.X. Dou, *Synthesis of catalyzed magnesium hydride with low absorption/desorption temperature.* Scripta Materialia, 2009. **61**(5): p. 469.

183. H. Imamura, Y. Takesue, T. Akimoto, and S. Tabata, *Hydrogen-absorbing magnesium composites prepared by mechanical grinding with graphite: effects of additives on composite structures and hydriding properties.* Journal of Alloys and Compounds, 1999. **293-295**: p. 564.

184. J. Huot, M.L. Tremblay, and R. Schulz, *Synthesis of nanocrystalline hydrogen storage materials.* Journal of Alloys and Compounds, 2003. **356-357**: p. 603.

185. J.L. Bobet, E. Grigorova, M. Khrussanova, M. Khristov, P. Stefanov, P. Peshev, and D. Radev, *Hydrogen sorption properties of graphite-modified magnesium nanocomposites prepared by ball-milling.* Journal of Alloys and Compounds, 2004. **366**(1-2): p. 298.

186. C.Z. Wu, P. Wang, X. Yao, C. Liu, D.M. Chen, G.Q. Lu, and H.M. Cheng, *Effect of carbon/noncarbon addition on hydrogen storage behaviors of magnesium hydride.* Journal of Alloys and Compounds, 2006. **414**(1-2): p. 259.

187. Z.G. Huang, Z.P. Guo, A. Calka, D. Wexler, and H.K. Liu, *Effects of carbon black, graphite and carbon nanotube additives on hydrogen storage properties of magnesium.* Journal of Alloys and Compounds, 2007. **427**(1-2): p. 94.

188. D. Chen, L. Chen, S. Liu, C.X. Ma, D.M. Chen, and L.B. Wang, *Microstructure and hydrogen storage property of Mg/MWNTs composites.* Journal of Alloys and Compounds, 2004. **372**(1-2): p. 231.

189. C.Z. Wu, P. Wang, X. Yao, C. Liu, D.M. Chen, G.Q. Lu, and H.M. Cheng, *Hydrogen storage properties of MgH2/SWNT composite prepared by ball milling.* Journal of Alloys and Compounds, 2006. **420**(1-2): p. 278.

190. S. Bouaricha, J.P. Dodelet, D. Guay, J. Huot, and R. Schulz, *Activation characteristics of graphite modified hydrogen absorbing materials.* Journal of Alloys and Compounds, 2001. **325**(1-2): p. 245.

191. A. Calka and A.P. Radlinski, *Universal high performance ball-milling device and its application for mechanical alloying.* Materials Science and Engineering: A, 1991. **134**: p. 1350.

192. H. Mio, J. Kano, and F. Saito, *Scale-up method of planetary ball mill.* Chemical Engineering Science, 2004. **59**(24): p. 5909.

193. T.P. Blach and E.M. Gray, *Sieverts apparatus and methodology for accurate determination of hydrogen uptake by light-atom hosts.* Journal of Alloys and Compounds, 2007. **446-447**: p. 692.

194. M. Porcu, A.K. Petford-Long, and J.M. Sykes, *TEM studies of Nb_2O_5 catalyst in ball-milled MgH_2 for hydrogen storage.* Journal of Alloys and Compounds, 2008. 453(1-2): p. 341.

195. P.J. Herley, William Jones, and G.R. Millward, *Electron beam decomposition of copper hydride and the generation of ultra-fine particles of copper* Journal of Materials Science Letters, 1989. 8(9): p. 1013.

196. G. Liang, *Synthesis and hydrogen storage properties of Mg-based alloys.* Journal of Alloys and Compounds, 2004. 370(1-2): p. 123.

197. T.B. Flanagan, C.N. Park, and W.A. Oates, *Hysteresis in solid state reactions.* Progress in Solid State Chemistry, 1995. 23(4): p. 291.

198. R. Gupta, F. Agresti, S.L. Russo, A. Maddalena, P. Palade, and G. Principi, *Structure and hydrogen storage properties of MgH_2 catalysed with La_2O_3.* Journal of Alloys and Compounds, 2008. 450(1-2): p. 310.

199. I. Kanoya, H. M., and S. T., *Development of high-capacity MgMH alloy for hydrogen storage.* Honda R & D Tech Rev, 2002. **14**(2): p. 91.

200. A.L. Yonkeu, I.P. Swainson, J. Dufour, and J. Huot, *Kinetic investigation of the catalytic effect of a body centered cubic-alloy $TiV_{1.1}$ $Mn_{0.9}$ (BCC) on hydriding/dehydriding properties of magnesium.* Journal of Alloys and Compounds, 2008. **460**(1-2): p. 559.

201. X. Liu, Z. Huang, L. Jiang, and S.Wang, *Thermal stabilization and hydrogen storage properties of Mg–40 wt% $Ti_{0.28}Cr_{0.50}V_{0.22}$ composite prepared by mechanical milling.* International Journal of Hydrogen Energy, 2007. **32**: p. 965.

202. J.L. Bobet and B. Darriet, *Relationship between hydrogen sorption properties and crystallography for $TiMn_2$ based alloys.* International Journal of Hydrogen Energy, 2000. **25**(8): p. 767.

203. X.B. Yu, Z.X. Yang, S.L. Feng, Z. Wu, and N.X. Xu, *Influence of Fe addition on hydrogen storage characteristics of Ti-V-based alloy.* International Journal of Hydrogen Energy, 2006. **31**(9): p. 1176.

204. R. Balasubramaniam, *Hysteresis in metal-hydrogen systems.* Journal of Alloys and Compounds, 1997. **253-254**: p. 203.

205. X. Yao, C. Wu, A. Du, G.Q. Lu, H. Cheng, S.C. Smith, J. Zou, and Y. He, *Mg-Based Nanocomposites with High Capacity and Fast Kinetics for Hydrogen Storage.* The Journal of Physical Chemistry B, 2006. **110**(24): p. 11697.

206. R. Schulz, J. Huot, G. Liang, S. Boily, G. Lalande, M.C. Denis, and J.P. Dodelet, *Recent developments in the applications of nanocrystalline materials to hydrogen technologies.* Materials Science and Engineering A, 1999. **267**(2): p. 240.

207. A.J. Du, S.C. Smith, X.D. Yao, and G.Q. Lu, *Catalytic Effects of Subsurface Carbon in the Chemisorption of Hydrogen on a Mg(0001) Surface: an Ab-initio Study.* The Journal of Physical Chemistry B, 2006. **110**(4): p. 1814.

208. X. Yao, C. Wu, A. Du, J. Zou, Z. Zhu, P. Wang, H. Cheng, S. Smith, and G. Lu, *Metallic and Carbon Nanotube-Catalyzed Coupling of Hydrogenation in Magnesium.* Journal of the American Chemical Society, 2007. **129**(50): p. 15650.

209. X.B. Yu, Y.H. Guo, H. Yang, Z. Wu, D.M. Grant, and G.S. Walker, *Improved Hydrogen Storage in Magnesium Hydride Catalyzed by Nanosized $Ti_{0.4}Cr_{0.15}Mn_{0.15}V_{0.3}$ Alloy.* The Journal of Physical Chemistry C, 2009. **113**(13): p. 5324.

210. J.J. Reilly and R.H. Wiswall, *Reaction of hydrogen with alloys of magnesium and nickel and the formation of Mg_2NiH_4.* Inorganic Chemistry, 1968. **7**(11): p. 2254.

211. J. Cermák and L. Král, *Hydrogen diffusion in Mg-H and Mg-Ni-H alloys.* Acta Materialia, 2008. **56**(12): p. 2677.

212. S. Orimo and H. Fujii, *Materials science of Mg-Ni-based new hydrides.* Applied Physics A: Materials Science & Processing, 2001. **72**(2): p. 167.

213. H. Imamura, N. Sakasai, and T. Fujinaga, *Characterization and hydriding properties of Mg-graphite composites prepared by mechanical grinding as new hydrogen storage materials.* Journal of Alloys and Compounds, 1997. **253-254**: p. 34.

214. S. Aminorroaya, et al., *Microstructure and activation characteristics of Mg-Ni alloy modified by Multi-Walled carbon nanotubes.* International Journal of Hydrogen Energy, 2009. **Under review**.

215. N. Bazzanella, R. Checchetto, and A. Miotello, *Catalytic effect on hydrogen desorption in Nb-doped microcrystalline MgH_2.* Applied Physics Letters, 2004. **85**(22): p. 5212-5214.

Acronyms

BCC: body centered cubic

CHN: carbon-hydrogen-nitrogen

CNT: carbon nanotube

CUTE: clean urban transport for Europe

CV: contracting volume

DSC: differential scanning calorimeter

EDS: energy dispersive x-ray spectroscopy (EDS)

EEA: European Environment Agency

GNF: graphite nanofiber

IEA: International Energy Agency

IMC: Intermetallic compounds

IPCC: Intergovernmental Panel on Climate Change

JMA: Johnson-Mehl- Avrami

LH_2: liquid hydrogen

MA: mechanical alloying

MM: mechanical milling

MOF: metal organic framework

MCS: reactive mechano-chemical synthesis

MCAS: mechano-chemical activation synthesis

MWCNT: multi-walled carbon nanotube

OECD: Organisation for Economic Co-operation and Development

PCT: pressure-composition-temperature

PEM: proton electrolyte membrane

RMA: reactive mechanical alloying

RMM: reactive mechanical milling

RT: room temperature

SEM: scanning electron microscope

SWCNT: single-walled carbon nanotube

TEM: transmission electron microscopy

TG: thermogravimetry

TPD: temperature programmed desorption

U.S. DOE: U.S. Department of Energy

XRD: X-ray diffraction

Publications

Journal papers (First Author):

A. Ranjbar, Z.P. Guo, X.B. Yu , D. Wexler, A. Calka, H.K. Liu, *Hydrogen Storage properties of MgH_2-SiC nanocomposites.* Materials Chemistry and Physics, 2009, **114**: p. 168.

A. Ranjbar, Z.P. Guo, X.B. Yu , A. Calka, H.K. Liu, *Effect of SiC with and without Ni on Hydrogen Storage Properties of MgH_2,* International Journal of Hydrogen Energy, 2009, **34**: p. 7263

A. Ranjbar, Z. P. Guo, X. B. Yu, A. Calka, H. K. Liu, *Hydrogen storage properties of Mg-BCC nanocomposite*, International Journal of Green Energy, 2009, **6**: p. 607.

A. Ranjbar, M. Ismail, Z.P. Guo, X. B. Yu, H. K. Liu, *Effect of CNTs on the hydrogen storage properties of MgH_2 and MgH_2-BCC composite.* International Journal of Hydrogen Energy, 2010, **35**: p. 7821.

A. Ranjbar, S. Aminorroaya, Z.P. Guo, Y. H Cho, Hua Liu, Arne Dahle, *A multi-scale production approach for Mg hydrogen storage alloys.* Journal of Alloys and Compounds. 2010: **Under Review**.

Journal papers (Co-Author):

X. B. Yu, Y. H. Guo, Z. P. Guo, **A. Ranjbar**, H. K. Liu, *A new multicompound hydrogen storage system: $Mg(BH_4)_2$-$LiNH_2$,* The Journal of Physical Chemistry C, 2010, **114**: p. 4733.

J. F. Mao, Z. P. Guo, C. K. Poha, **A. Ranjbara**, X. B. Yu, H. K. Liua, *Study on the dehydrogenation kinetics and thermodynamics of $Ca(BH_4)_2$,* Journal of Alloys and Compounds, 2010, **500**: p. 200.

S. Aminorroaya, **A. Ranjbar**, Y. Cho, H. K. Liu and A. K. Dahle, *Hydrogen storage properties of Mg-10 wt% Ni alloy co-catalysed with Niobium and multi-walled carbon nanotubes*, International Journal of Hydrogen Energy 2010: Manuscript approved**, In Press**.

M. Ismail, **A. Ranjbar** , Y. Zhao, X.B. Yu, S. X. Dou, *Improved hydrogen storage property of Lithium Alanate by milling with carbon based additives*, Carbon 2010: **Under Review**.

Conference papers:

S. Aminorroaya, **A. Ranjbar**, H. K. Liu, Y. Ch, A. K. Dahle, *Structural study and hydrogen sorption kinetics of ball-milled samples of cast Mg-10%Ni catalysed by Nb.* Proceeding of Materials Challenges in Alternative and Renewable Energy, 21-24 Feb. 2010, Cocoa beach, Florida, USA.

A. Ranjbar, Z. P. Guo, X. B. Yu, A. Calka, H. K. Liu, *Characterization of hydrogen storage properties of Mg-BCC with different ball to sample weight ratio* . Hydrogen and Fuel Cell Conference, Vancouver, Canada 2009.

A. Ranjbar, Z. P. Guo, X.B. Yu, A. Calka, H.K. Liu, *Effect of different amount of SiC on Hydrogen Storage properties of* MgH_2, 17th World Hydrogen Energy Conference, Brisbane, Australia 2008.

H. Salamati, F. Nekui, **A.Ranjbar**, *A Comparative Study of Experimental Techniques for Critical Current Densities and Microstructure of Ag-doped YBCO Superconductors*, ICMF, Hungary 1998.